METHOD OF THIN FLEXIBLE MICROELECTRODE INSERTION IN DEEP BRAIN REGION FOR CHRONIC NEURAL RECORDING

by

Muhammad Abdullah Arafat

A Dissertation

Submitted to the Faculty of Purdue University

In Partial Fulfillment of the Requirements for the degree of

Doctor of Philosophy

School of Electrical and Computer Engineering

West Lafayette, Indiana

December 2019

THE PURDUE UNIVERSITY GRADUATE SCHOOL
STATEMENT OF COMMITTEE APPROVAL

Dr. Pedro P. Irazoqui, Chair
Department of Electrical and Computer Engineering
Department of Biomedical Engineering
Dr. Muhammad Ashraful Alam
Department of Electrical and Computer Engineering
Dr. John G. R. Jefferys
Department of Biomedical Engineering
Department of Pharmacology, University of Oxford, Oxford, UK
Dr. Zhongming Liu
Department of Electrical and Computer Engineering
Department of Biomedical Engineering
Dr. Robert Worth
Department of Mathematical Sciences, IUPUI
Neurosurgeon, Indianapolis

Approved by:
Dr. Dimitri Peroulis
Head of the Graduate Program

Dedicated to my parents

ACKNOWLEDGMENTS

I would like to acknowledge the many people who have assisted me during my time here at Purdue University.

- My supervisor Dr. Pedro Irazoqui for his constant support and guidance.
- My committee members, Dr. Pedro Irazoqui, Dr. Muhammad Ashraful Alam, Dr. John G. R. Jefferys, Dr. Zhongming Liu and Dr. Robert Worth.
- My ECE graduate school advisor, Matt Golden.
- Dr. Quan Yuan and Dr. Matthew Ward of the Weldon School of Biomedical Engineering
- Bill Schoenlein, Susan Hardy and Asem Aboelzahab of the Martin Jischke Hall of Biomedical Engineering
- Dr. Thelma Lovick of Bristol University, Bristol, UK
- My lab-mates: Dan Pederson, Jack Williams, Chris Quinkert, Jesse Somann, Ryan Budde, Ethan Biggs, Rachael Swenson, Steven Lee, Kurt Quing, Zhi Wang, Henry Zhang, Gabriel Albors, Hans Ajieren, Jay Shah, Curtis Slaubaugh, Jui-Wei Tsai, Logan Rubin, Kelsey Bayer, Kelsey Wasilczuk, Kaitlyn Neihouser, Vivek Ganesh, Gang Seo, Shelby Olson, Mark Bevilacqua, Adam Scott, Trevor Meyer, Ahoura Mortazavi, Georgia Lawlor, Brett Collar, Drew Fox, Michael Thomas Williams, Sydney Sofronici, Yvonne Chen and Isaac Meng.
- My wife Nahrin Nowrose for her physical, emotional, and spiritual support during my time here at Purdue.
- My parents Dr. Md. Mohar Ali and Mrs. Afroza Begum, my elder sisters Dr. Mahbuba Begum and Dr. Meher Nigar Neema, my elder brother Dr. Muhammad Abdullah Adnan for their overwhelming support of my academic aspirations throughout various stages of my life.

TABLE OF CONTENTS

LIST OF TABLES

LIST OF FIGURES

LIST OF ACRONYMS

ABS……	Acrylonitrile Butadiene Styrene
ADC……	Analog to Digital Converter
ASIC……....	Application Specific Integrated Circuit
BMI……	Brain Machine Interface
BotC……	Botzinger Complex
BP……	Blood Pressure
CBF……..	Critical Buckling Force
CE……	Counter Electrode
CID……...	Center for Implantable Devices
CMOS……..	Complementary Metal Oxide Semiconductor
CMRR……..	Common Mode Rejection Ratio
CSF……...	Cerebrospinal Fluid
CT……	Computer Tomography
DAQ……	Data Acquisition
dB……	Decibel
DC……	Direct Current
ECoG……	Electrocorticogram
EEG……..	Electroencephalogram
EIS……	Electrochemical Impedance Spectroscopy
HR……	Heart Rate
IACUC……	Institutional Animal Care and Use Committee
IC……..	Integrated Circuit
IP……..	Intraperitoneal
KA……	Kainic Acid
LCD……..	Liquid Crystal Display
LFP……...	Local Field Potential
MIM……	Metal Insulated Metal
MOSFET……..	Metal Oxide Semiconductor Field Effect Transistor
MUX……	Multiplexer
OPAMP……	Operational Amplifier
PACUC……	Purdue Animal Care and Use Committee
PBS……..	Phosphate Buffered Saline
PCB……..	Printed Circuit Board
PEG……..	Polyethylene Glycol
PETH……	Peri Event Time Histogram
POT……..	Potentiometer
PR……	Photoresist
PSRR……	Power Supply Rejection Ratio
Pt……..	Platinum
RE……	Reference Electrode
RF……	Radio Frequency
RIE……...	Reaction Ion Etching

RPS……..	Revolution Per Second
SNR……..	Single to Noise Ratio
SPDT……	Single Pole Double Through
SpO_2…….	Peripheral Capillary Oxygen Saturation
SPST…….	Single Pole Single Through
SUDEP…….	Sudden Unexpected Death in Epilepsy
TeNT……	Tetanus Neurotoxin
UV……	Ultra Violet
WE……...	Working Electrode
WPT…….	Wireless Power Transfer

PREFACE

Portions of this paper have been previously published and reproduced with permission from IEEE Transactions on Neural Systems and Rehabilitation Engineering and Epilepsia journals.

M. A. Arafat, L. N. Rubin, J. G. R. Jefferys, and P. P. Irazoqui, "A Method of Flexible Micro-Wire Electrode Insertion in Rodent for Chronic Neural Recording and a Device for Electrode Insertion," *IEEE Trans Neural Syst Rehabil Eng,* vol. 27, no. 9, pp. 1724-1731, Sep 2019, doi: 10.1109/TNSRE.2019.2932032.

J. G. R. Jefferys, M. A. Arafat, P. P. Irazoqui, and T. A. Lovick, "Brainstem activity, apnea, and death during seizures induced by intrahippocampal kainic acid in anaesthetized rats," *Epilepsia,* Nov 2019, doi: 10.1111/epi.16374.

ABSTRACT

Reliable chronic neural recording from focal deep brain structures is impeded by insertion injury and foreign body response, the magnitude of which is correlated with the mechanical mismatch between the electrode and tissue. Thin and flexible neural electrodes cause less glial scarring and record longer than stiff electrodes. However, the insertion of flexible microelectrodes in the brain has been a challenge. A novel insertion method is proposed, and demonstrated, for precise targeting deep brain structures using flexible micro-wire electrodes. A novel electrode guiding system is designed based on the principles governing the buckling strength of electrodes. The proposed guide significantly increases the critical buckling force of the microelectrode. The electrode insertion mechanism involves spinning of the electrode during insertion. The spinning electrode is slowly inserted in the brain through the electrode guide. The electrode guide does not penetrate into cortex. The electrode is inserted in the brain without stiffening it by coating with foreign material or by attaching a rigid support and hence the method is less invasive. Based on two new mechanisms, namely spinning and guided insertion, it is possible to insert ultra-thin micro-wire flexible electrodes in rodent brains without buckling. I have demonstrated successful insertion of 25 μm platinum micro-wire electrodes about 10 mm deep in rat brain. A novel micro-motion compensated ultra-thin flexible platinum microelectrode has been presented for chronic single unit recording. Since manual insertion of the proposed microelectrode is not possible, I have developed a microelectrode insertion device based on the proposed method. A low power low noise 16 channel programmable neural amplifier ASIC has been designed and used to record the neural spikes. The ability to record neural activity during insertion is a unique feature of the developed inserter. In vivo implantation process of the microelectrode has been demonstrated. Microelectrodes were inserted in the Botzinger complex of rat and long term respiratory related neural activity was recorded from live rats. The developed microelectrode has also been used to study brain activity during seizures. In-vivo experimental results show that the proposed method and the prototype insertion system can be used to implant flexible microelectrode in deep brain structures of rodent for brain studies.

1. INTRODUCTION

1.1 Neural Recording

The most complex organ in our body is our brain. It contains numerous neurons and glial cells which convey information using electrical signals in the form of action potentials and chemical signals in the form of neurotransmitter. As neuroscience research evolves and more questions about the functions of the brain arise, the need for more advanced experimental tools also arises. One such tool is a brain–machine interface (BMI) wherein the brain and machine communicate via electrical activity using electrodes. Electrode as the BMI is the most important part in recording neural activities [1-5]. There are various types of electrodes for recording various neural activities in the brain. Some are noninvasive and some are invasive. Noninvasive electrodes are used to capture signal such as electroencephalogram (EEG) from outside the skull. Invasive electrodes are used to capture electrocorticogram (ECoG), local field potential (LFP) or spike activity. Metal exposed tip or surface are used to record these neural signals. Single unit spike recording requires high spatial resolution which can be obtained by using a microelectrode with small exposed surface or with a sharp tip. Action potentials from specific neurons are recorded to study neuronal behavior [6, 7]. Analyzing neural signals is important for discovering specific mechanisms of brain functions and for investigating brain diseases such as Parkinson's disease, epilepsy and chronic pain [8-11].

1.2 Penetrating Single Unit Recording Electrode

Implantable electrodes are referred to as the electrodes that are surgically implanted on the surface of the brain (non-penetrating) or penetrated into the brain (penetrating) to record neural activities from neurons. Single unit recording electrodes are the ones which can detect neural spikes from individual neurons. Single-unit recording provides a method of measuring the electro-physiological responses of single neurons using a microelectrode system. When a neuron generates an action potential, the signal propagates down the neuron as a current which flows in and out of the cell through excitable membrane regions in the soma and axon. If a microelectrode is inserted into the brain, it can record the rate of change in voltage with respect to time. When the exposed sharp metal tip comes closer to a neuron, it detects the potential change of the

neuron. Glass micropipette is the first penetrating cortical electrode. It was made of an electrolyte-filled glass pipette with a tip diameter of 1 micrometer [12]. These glass micropipettes are mainly used to record intracellular activities but also can record extracellular activities. However, the glass micropipettes cannot be used in chronic studies due to electrolyte leakage, fragility and brain damage. In 1950, Woldring and Dirken report the ability to obtain spike activity from the surface of the cerebral cortex with platinum wires [13]. In 1953, Dowben and Rose developed the iridium micro-wire for recording [14]. In 1958, the stainless steel microelectrode was developed [15]. In 1959, Hubel and Wiesel used single neuron recordings to map the visual cortex in unanesthetized, unrestrained cats using tungsten electrodes [16]. In 1960, glass-insulated platinum microelectrodes were developed for recording [17].

Metal electrodes are made of various types of metals such as platinum, tungsten, platinum-10% iridium, gold, alloy, stainless steel, silver. They have high low-frequency impedance and low high-frequency impedance. They are suitable for measurement of extracellular action potentials. They have high signal-to-noise ratio (SNR) due to lower impedance for the frequency range of spike signals. They also have better mechanical stiffness for puncturing through brain tissue. They are easily fabricated into different tip shapes and sizes at large quantities. However, metal electrode should consider chronic reaction for long-term neural recording. It the material is not chosen properly, the electrode tip can dissolve in the tissue fluids and the whole electrode can cause inflammatory reaction [18]. Therefore, researchers have evaluated the immune response of the brain tissue for various metal micro-wires implanted into brain. According to their studies, platinum and gold are considered as the most “non-toxic” metals for implantable electrodes [19]. Over the past few years these implanted microelectrodes have led to breakthrough discoveries and technological innovations such as restoration of the cortical control of the upper limbs [22], control of robotic end effectors [20, 21], discovery of fundamental mechanisms underlying cognitive processes [23, 24] and discovery of neural activity during epileptic seizures [25, 26].

1.3 Inflammatory Reaction of Rigid Neural Probe

A fundamental problem with the rigid electrodes is the contradiction between the materials properties needed for implantation and the properties required to minimizing long-term neural trauma. Neural probes made of rigid wire or silicon substrate suffer from the mechanical

mismatch between stiff electrode and soft brain tissue [27]. Due to this mechanical mismatch and insertion damage, the immune response creates an inhospitable environment that isolates the probe from the neural tissue of interest over time [28], [29]. An insulating sheath of astrocytes is created between electrodes and neurons which isolates the neurons from the electrode surface and moves the neurons away from the recording site over time [30], [31]. Therefore, although stiff probes are easy to insert into soft brain tissue, they create foreign body response that increases with time. Moreover, the relative micro-motion between the brain and the electrode creates more glial scar encapsulating the probe and results in neuronal death [32]. Due to persistent and progressive scarring caused by the foreign body response to electrodes, the number of neurons near the electrode decreases with time [33]. Therefore, neural spikes of interest are no longer visible and long-term chronic neural signal recording is not possible with rigid electrodes.

1.4 Thin and Flexible Neural Electrode

Researchers have demonstrated that the scar formation minimizes for thinner and flexible electrodes [34-36]. Because of much smaller cross-sectional area, thin wire electrodes displace smaller volume of tissue and cause much less compression on the surrounding tissue compared to thicker electrode. Also, when the electrode gets thinner, it becomes flexible which reduces relative micro-motion between brain and electrode. The major drawback of the thin and flexible electrodes in the surgical implantation: when the unsupported length of the electrodes is longer than a certain length (1-2 mm), they buckle rather than enter the brain tissue [37]. Therefore, insertion methods and devices are necessary to implant these electrodes.

1.5 Existing Insertion Methods and a Need for a Novel Insertion Method

Engineers have developed few insertion methods in the past years to solve the challenge. In 2001, Rousche et al., fabricated polyimide-based intracortical electrode arrays which were inserted after making sharp incision in the brain using a blade [38]. Since invasive incision is required, unwanted brain damage can be associated in the implantation process. Moreover, the implanted electrodes were only 1.5 mm in length. Insertion of electrodes in deep brain region is not possible using this method.

In 2004, Shoji et al. invented parylene based 3D flexible electrode and coated the electrode by bio dissolvable polyethylene glycol, PEG to have necessary stiffness for insertion [39]. After the insertion, PEG was dissolved in the neural tissue and the probe became flexible. The demerit of this method is that it injects foreign particles inside brain which may cause brain damage or other side effects. Also, the electrodes implanted in the experiment were only 1 mm in length. For deep brain electrode, this method is not feasible. Other than PEG, sucrose gel, hydro gel sheath was also used to increase stiffness of the electrode in some studies [40-43]. However, substantial amount of coating material would be required for deep brain electrodes. Some researchers used various rigid structures which were attached to the flexible electrodes while insertion and then removed after insertion leaving the flexible probe behind [44-49]. The increased rigidity and footprint of the stiffener-electrode assembly can aggravate the acute and chronic injury, damaging or destroying nearby neurons and breaching the blood brain barrier [48, 50]. Also, a substantial amount of brain cells is displaced and withdrawn with the rigid structure.

A magnetic tension-based insertion mechanism was proposed in [51]. Probes were constructed from a sharp magnetic tip attached to a flexible tether. A pulsed magnetic field was generated in a coil surrounding the electrode. The applied magnetic field pulls the electrode tip forward, accelerating the probe into the neural tissue. The limitation of this method is that the probe has to be made out of magnetic materials. Therefore, widely used materials such as platinum and gold cannot be used as the electrode material. Another drawback of this method is that the penetration depth of electrode is not well controlled because of the inhomogeneous density and variable structure of the brain. Therefore, targeting a particular type of neuron is not possible using this method. Also, adjustment of the electrode depth is not possible after shooting the electrode.

In recent years, a method based on a viscous drag force on the microelectrode applied by flowing liquid in a micro-fluidic channel has been proposed [52]. A micro-fluidic actuation device has been fabricated and used for this purpose. Carbon nanotube fiber microelectrode has been inserted 4 mm deep in rat brain using fluidic micro-drives, though nothing is stated about the condition of dura. Micro-positioning the electrode with this method is difficult. Also, the electrode can only go inside the brain. Backward motion is not possible with the device. The

feasibility of implanting longer electrode is unknown. Moreover, making contacts with the microelectrodes after implantation is very difficult and most often the neural signal is lost while making this connection due to micro motion.

A new technology to insert and precisely position flexible ultrathin electrodes without temporary stiffening would significantly improve the robustness and utility of flexible electrodes while minimizing excess damage to the brain from stiffeners. Due to the unavailability of such insertion method, a novel insertion method is necessary for chronic neural recording from deep brain structures.

1.6 Novel Insertion Method

In this dissertation, a method of inserting flexible micro-wire electrode in deep brain without removing dura is proposed. The method is derived from the principles governing the buckling strength of electrodes. Two new concepts are introduced to increase critical buckling force (defined in Section 2.2) of the electrode and reduce brain penetration force. A novel micro-wire single shank electrode design is provided. An electrode insertion device based on the proposed mechanism is also presented. In-vivo experiments demonstrate the effectiveness of the proposed insertion mechanism. The ultimate goal of this study is to develop and validate a technology platform that is capable of implanting flexible micro-wire electrode into deep brain structures for chronic brain signal studies.

Chapter 2 describes the novel microelectrode insertion method. Chapter 3 contains the design of a novel ultra thin micro-motion compensated micro-wire electrode. The design of the flexible micro-wire electrode inserter is given in Chapter 4. A low power low noise neural amplifier integrated circuit (IC) design for recording spikes is shown in Chapter 5. Chapter 6 provides the in vivo electrode implantation method and shows chronically recorded neural activity in rat. Finally, Chapter 7 provides the conclusion of the study.

2. FLEXIBLE MICROELECTRODE INSERTION METHOD

2.1 Buckling of Micro-wire Electrode

When a micro-wire cannot penetrate a medium, one of the three phenomena can occur. They are: bending, buckling and rupture [53]. In case of micro-wire penetrating a medium, rupture does not occur because of the properties of metal. In case of flexible micro-wire penetrating a brain, bending normally does not occur because buckling occurs before bending takes place. Therefore, I will focus on buckling of micro-wires for brain penetration. Figure 2.1(a) shows the buckling of a platinum (Pt) micro-wire electrode while penetrating 0.6% agar gel [54]. The wire buckles because it cannot provide the required penetration force on the agar gel. There are six modes of buckling depending on the end supports as shown in Figure 2.1(b). For the system of Figure 2.1(a), the mode of buckling is "one-pinned end and one-fixed end".

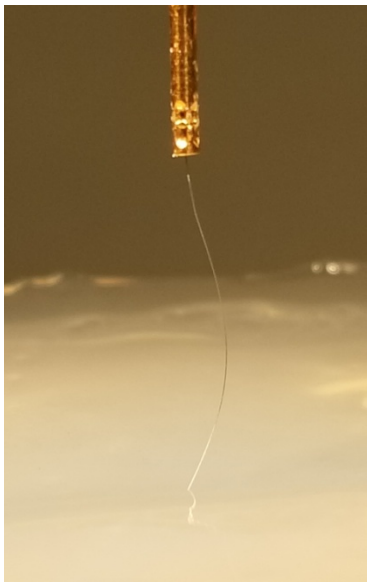

(a)

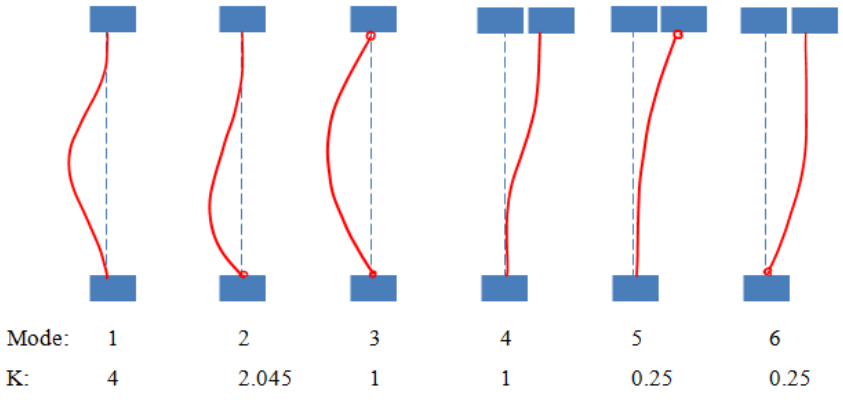

(b)

Figure 2.1 (a) Buckling of Pt microelectrode during insertion in 0.6% agar gel, (b) Six different modes of buckling. Buckled shape of electrode is shown by red line. Mode 1 is called "both-fixed end" and mode 2 is called "one-pinned end and one-fixed end" because of the end supports.

2.2 Critical Buckling Force (CBF)

To develop an insertion method, we first need to know how much force a micro-wire can exert before buckling. Critical Buckling Force (CBF) is a measure of the stiffness of a wire. CBF is defined as the maximum force a wire can bear while staying straight. It depends on the geometry of the wire and the elastic modulus of the wire material [55]. For a cylindrical wire, CBF is theoretically calculated from the following formula [53, 56]:

$$P_{cr} = \frac{K\pi^3 E r^4}{4L^2} \tag{2.1}$$

where, P_{cr} is the CBF of the wire in Newtons, K is the effective length factor (dimensionless) which depends on the end supports of the wire, E is the elastic modulus of the material in Pascals, L is the effective length in meters and r is the radius of wire in meters. This formula was derived in 1757, by the Swiss mathematician Leonhard Euler and it is known as Euler's column formula because of its broad use in designing columns of buildings.

Table 2.1. Elastic modulus of commonly used electrode materials

Material	Elastic Modulus (GPa)
Platinum	168
Iridium	528
Platinum-10% Iridium	204
Gold	79
Stainless Steel	200
Silicon	130-185
Tungsten	400

Some commonly used electrode materials are platinum, iridium, platinum-iridium, tungsten, gold, carbon fiber, stainless steel and silicon. The elastic modulus of some materials is listed in Table 2.1. And in the "one-pinned end and one-fixed end" mode of buckling, the value of K is 2.045. Now Figure 2.2 shows how CBF varies with the length of wire for three different diameters

(25µm, 50µm and 75µm) of platinum- 10% iridium (Pt10%Ir) wires. I also have measured the CBF using a micro-force sensor, S256 (10 gm) from Strain Measurement Devices, Wallingford, CT 06492, USA, and the data are shown in Figure 2.2. The experimentally measured CBF values match with the theoretical values. Figure 2.2 shows that a 10 mm length 25 um diameter Pt10%Ir wire can only apply 0.8 mN force on the brain surface before buckling.

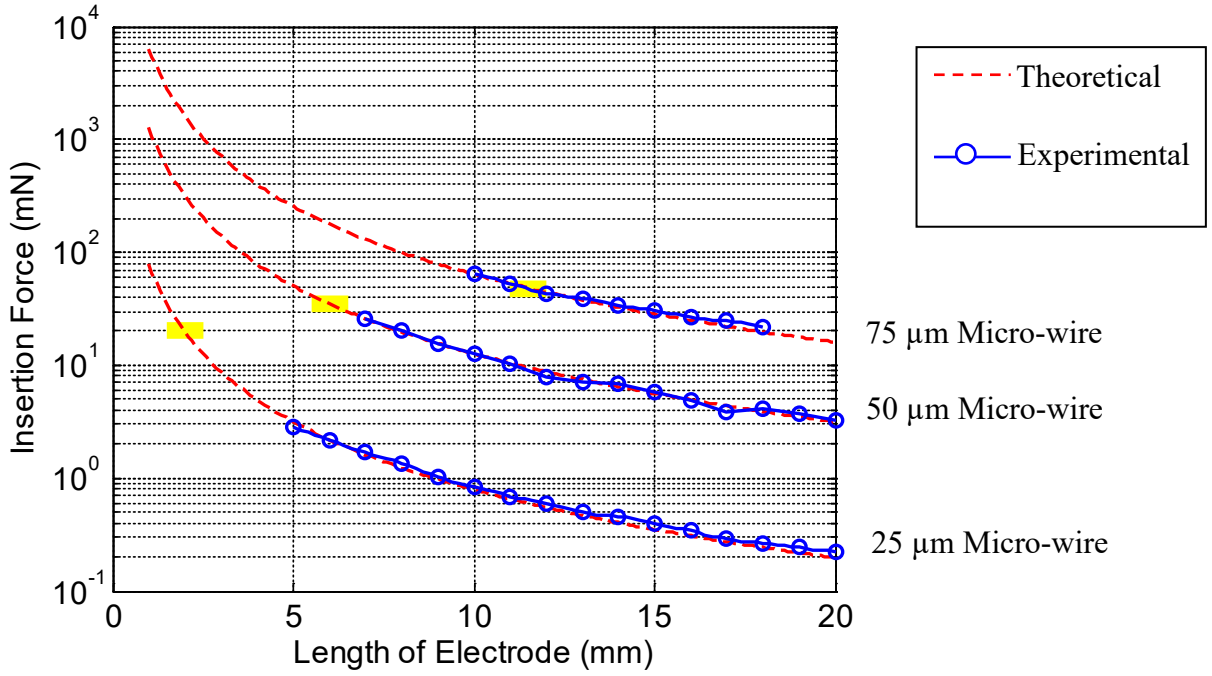

Figure 2.2 Critical buckling force of Pt10%Ir micro-wire. The yellow marks show the length of the corresponding electrodes at which penetration failure starts to occur.

2.3 Self Penetration Length

Various lengths of Pt- 10%Ir micro-wires with different diameters and tip geometries have been inserted in rat brains. Each wire having specific length, diameter and tip geometry has been inserted 3 times at 3 different locations in the hippocampus of rat brain, and the numbers of penetrations without buckling and the numbers of buckling occurrences have been counted which are given in Table 2.2-2.4. The probability of successful penetration for a specific wire is graphically shown in Figure 2.3. Figure 2.3 shows that for a successful penetration of 25um Pt-10%Ir wire with a scissor cut tip, its length has to be less than 1 mm. Now relating Figure 2.2 to

Figure 2.3, it is found that it takes more than 10 mN (80 mN) force for a sharp (scissor cut) 25um electrode to penetrate the dura.

Table 2.2 Number of penetrations and number of buckling occurrences of 25 μm micro-wire for various lengths and tip geometries

Wire Length (mm)	Scissor Cut Tip			Round Tip			Sharp Tip		
	No. of Penetra-tion	No. of Buckling	Total No. of Trial	No. of Penetra-tion	No. of Buckling	Total No. of Trial	No. of Penetra-tion	No. of Buckling	Total No. of Trial
1	3	0	3	3	0	3	3	0	3
2	2	1	3	3	0	3	3	0	3
2.5				1	2	3			
3	0	3	3	0	3	3	1	2	3
4	0	3		0	3	3	0	3	3
5							0	3	3

Table 2.3 Number of penetrations and number of buckling occurrences of 50 μm micro-wire for various lengths and tip geometries

Wire Length (mm)	Scissor Cut Tip			Round Tip			Sharp Tip		
	No. of Penetra-tion	No. of Buckling	Total No. of Trial	No. of Penetra-tion	No. of Buckling	Total No. of Trial	No. of Penetra-tion	No. of Buckling	Total No. of Trial
4	3	0	3						
5	3	0	3						
6	2	1	3						
7	0	3	3	3	0	3			
8	0	3	3	3	0	3			
9				1	2	3			
10				0	3				
11				0	3				
12							3	0	3
13							3	0	3
14							2	1	3
15							0	3	3
16							0	3	3

Table 2.4 Number of penetrations and number of buckling occurrences of 75 µm micro-wire for various lengths and tip geometries

Wire Length (mm)	Scissor Cut Tip			Round Tip			Sharp Tip		
	No. of Penetra-tion	No. of Buckling	Total No. of Trial	No. of Penetra-tion	No. of Buckling	Total No. of Trial	No. of Penetra-tion	No. of Buckling	Total No. of Trial
10	3	0	3						
11	3	0	3						
11.5	2	1	3						
12	0	3	3	3	0	3			
13	0	3	3	3	0	3			
14				2	1	3			
15				1	2	3			
16				0	3	3			
17				0	3	3			
18							3	0	3
19							3	0	3
20							3	0	3

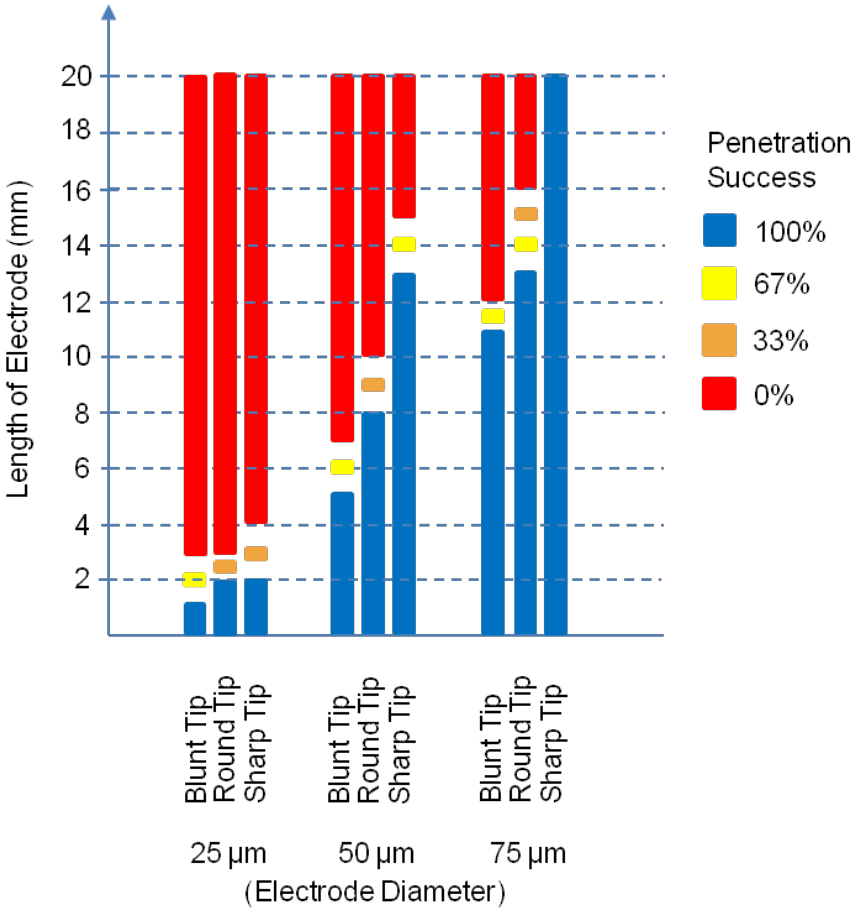

Figure 2.3 Probability of successful penetration of Pt-10%Ir wire in rat brain for various lengths, diameters and tip geometry.

2.4 Use of Electrode Guide to Increase CBF

It is clear from Section 2.4 that the CBF of the micro-wire needs to be increased to penetrate the brain. One way to increase CBF is to increase *r* (Equation 1). Doubling *r* gives 16 times increase in CBF. To have 10 mN CBF required to penetrate into cerebral cortex by a sharp Pt electrode, the diameter of the electrode has to be 62.6 um. However, increasing *r* makes the electrode stiffer, which is not desirable. Therefore, I chose the alternate solution which is using a guide to restrict buckling.

One candidate for a guide could be a cylindrical tube as shown in Figure 2.4(a), but it is problematic because the electrode gets stuck inside the tube when adhesive blood and cerebrospinal fluid (CSF) quickly fill the narrow tube by capillary action during in-vivo experiments. Moreover, retracting the tube after insertion is a problem because the electrode socket cannot pass through the tube. Even if the electrode is detached from the socket before retracting the tube, the tube displaces the electrode while retracting because of the growing friction developed by blood and CSF with time. In addition, attaching the socket to the electrode after insertion is very difficult. To overcome all these problems, I have proposed a new electrode guide which is shown in Figure 2.4(b) [57].

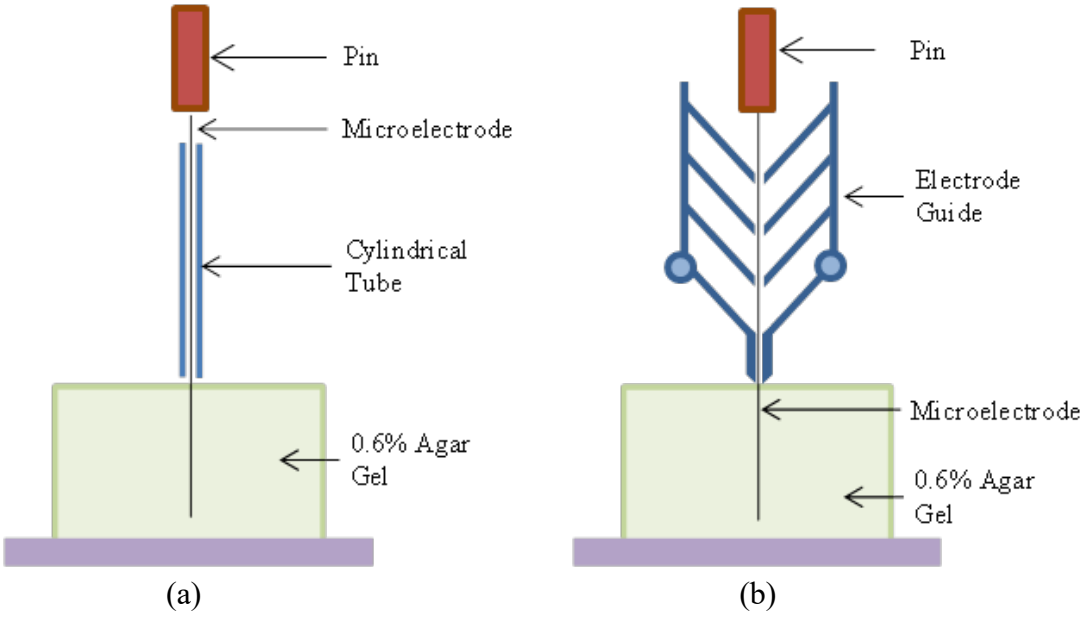

Figure 2.4 (a) A cylindrical tube restricts the electrode from buckling, (b) Proposed electrode guide. © [2019] IEEE Reprinted with permission from [57]

The electrode guide is designed to reduce contact area between the electrode and the guide in order to reduce friction due to blood and CSF. The guide consists of 4 pairs of separated arms and each pair forms a micro-hole through which the electrode passes. The guide restricts the electrode from buckling at points where the micro-holes are located. Since the electrode can only buckle between two micro-holes, the effective length of buckling depends on the separation of arms. The guided insertion creates a twofold increase in CBF. First, the guide reduces the effective length of electrode allowed for buckling. Since CBF is proportional to $1/L^2$, the guide significantly increases CBF. Second, by using a guide, buckling follows "both ends fixed" mode rather than "one-pinned end and one-fixed end" mode when the electrode penetrates cortex [53]. When the electrode is inside brain, the mode of buckling for the portion of electrode above the brain is still "both ends fixed" mode. In this mode, $K = 4$ which further doubles the CBF. According to Equation (1), a guide having 5 mm separation between arms can increase the CBF of Pt microelectrode to 5 mN, which is large enough to penetrate rat brain if the dura is removed in advance. Therefore, I designed the guide with 5 mm separation between arms. The electrode guide is described in Section 4.3 in detail.

2.5 Spinning During Insertion to Penetrate Dura

The proposed guide alone cannot make successful penetration of 10 mm long electrode when dura is present. In this case, the electrode is spun slowly to pierce the dura. The spinning electrode bores a micro-hole in the dura and penetrates through it. Although a higher insertion force is required to penetrate dura [58, 59], the electrode pierces dura by its spinning motion. The driving force for the electrode is the pressure applied to it. When the electrode touches brain surface, it initially creates a small dimple, unlike with impact insertion [60, 61]. The electrode then gradually slides inside the brain. Even after penetration, the dura sticks to the side of the electrode and clutches it. Therefore, the electrode is kept spinning until it nears the target. When the electrode reaches close to the target, I stop spinning. I then advance the electrode in micro-steps into the brain until I find desired neuron.

3. FABRICATION OF FLEXIBLE ULTRA-THIN MICRO-WIRE ELECTRODE FOR SINGLE UNIT RECORDING

3.1 Electrode Fabrication

The flexible microelectrode is fabricated from 25µm platinum (Pt) single core wire. The micro-wire is obtained from AM Systems, WA, USA (catalog number - 764500). In this study, I have used the electrodes to record from the brainstem region of rat brain. The target is about 10 mm deep in the brain from the skull surface. I cut 17 mm long pieces of wire from the spool using a micro-scissor (Fine Science Tools, Foster City, CA, USA, PN: 15000-11). Each 17 mm long piece of wire is used to make one electrode. Among the additional 7 mm length of wire, 6 mm is required by the design of the electrode inserter and 1 mm is used to attach a metallic socket to the electrode to hold it during insertion. The micro-wire is attached to a thicker wire such as 0.3 mm tinned coated copper wire by spot welding as shown in Figure 3.1. The tinned copper wire is then trimmed down to 1 mm. A gold-plated female socket, obtained from Plastics1, VA, USA (catalog number E363/0), is attached to the micro-wire. The 1 mm tinned copper wire along with the micro-wire is put into the socket and the socket is attached by crimping. The length of the wire becomes 16 mm. The reason behind using a thicker wire instead of directly crimping the socket to the micro-wire is to make a reliable and strong mechanical connection. Instead of spot welding to a thicker wire and then crimping the socket, the micro-wire could also be attached to the socket directly by soldering. However, soldering the micro-wire could burn and damage the electrode. The curved micro-wire is then made straight by holding the socket in one hand and pulling the micro-wire very gently along the length with the other hand. Figure 3.2 shows a 16 mm long electrode after straightening.

3.2 Micro-wire Tip Etching

The bare end is electrochemically etched to make a sharp tip for single unit recording. The platinum wire is etched in 1.5 M $CaCl_2$ solution by dip etching. A thick spiral Pt wire is used as a counter electrode. A $6V_{pp}$ 60Hz sinusoidal voltage is applied between the micro-wire electrode and the counter electrode. The micro-wire is dipped 20 times in the $CaCl_2$ solution. For a fixed amplitude of voltage, the sharpness of the tip increases with the number of dips. The rate of

dipping is 30 dips/min. After etching, the electrode is rinsed with deionized water. Figure 3.3 shows the electrode tip before and after electrochemical etching.

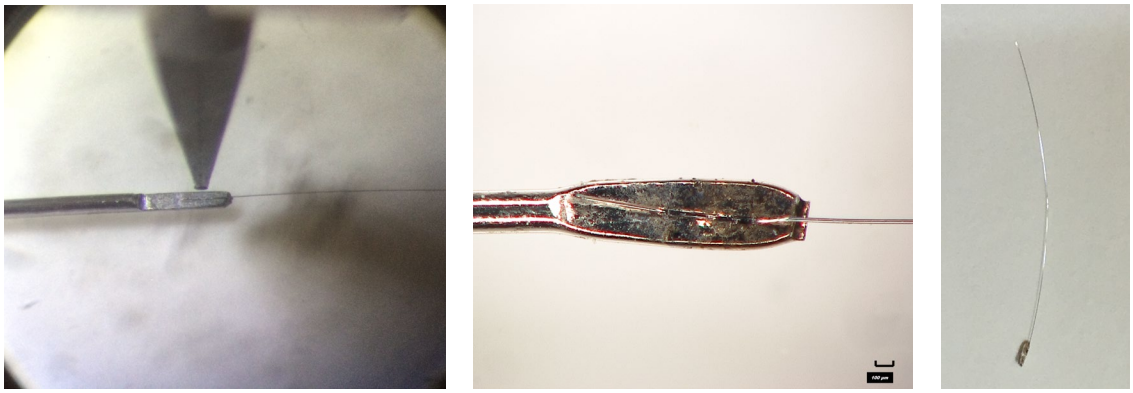

(a) (b) (c)

Figure 3.1 Fabrication steps of neural electrode using ultra-thin flexible Pt micro-wire. (a) Spot welding of micro-wire to a thicker wire for stability. (b) Spot welded micro-wire. (c) Trimmed wire assembly ready to be crimped in female socket pin.

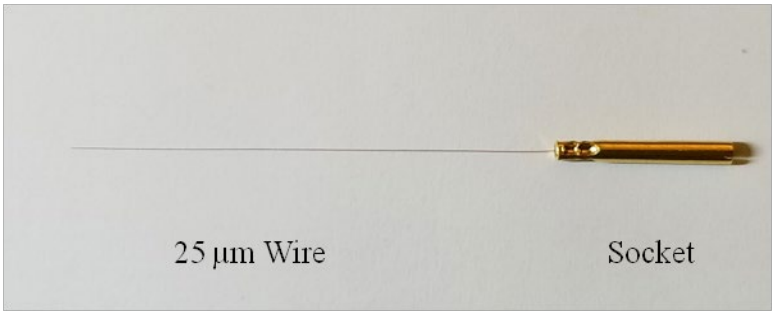

Figure 3.2 Straightened 25 µm diameter Pt electrode after crimping socket. © [2019] IEEE Reprinted with permission from [57]

3.3 Micro-wire Coating using Biocompatible Polymer

The sharp micro-wire is then insulated by coating with parylene C. Parylene C is a biocompatible polymer [62]. The Specialty Coating Systems, PDS 2010 parylene deposition system is used to coat the micro-wires. Parylene C is deposited by a chemical vapor deposition method. The process temperature and pressure parameters used in this system are given in Table 3.1. The average thickness of the coating is 2 µm. Before coating the micro-wire with parylene C, the socket is covered with a silicone tube. The silicone tube is removed after parylene C deposition.

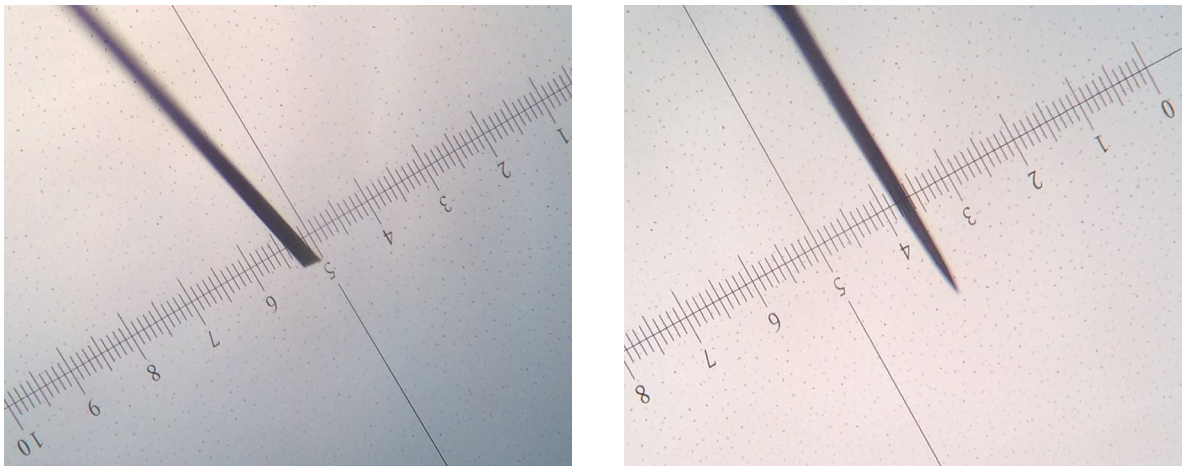

(a) (b)

Figure 3.3 (a) Microelectrode tip before etching. (b) Microelectrode tip after electrochemical etching in $CaCl_2$ solution.

Table 3.1 Process parameters for parylene C coating and etching

Parylene C Coating		Parylene C Etching	
Furnace	690˚C	RF Power	50 W
Chamber Gauge	135˚C	Pressure	50 mTorr
Vaporizer	175˚C	Gas Flow	50 sccm
Vacuum	15 mTorr	Etching Time	30 min

3.4 Tip Deinsulation

After coating, the sharp tip of the micro-wire is exposed to provide electrical connection to the neural tissue and lower impedance and electrical noise. This is done by etching parylene from the tip using reactive-ion etching (RIE) technology. Conventional technique for deinsulating stiff electrode by poking the electrodes through aluminum foil followed by an oxygen plasma etch does not work for ultra-thin long flexible wire [62]. I have developed a new technique to deinsulate the tip of ultra-thin long flexible wire. Figure 3.4 shows the schematics of step-by-step process of tip deinsulation. First, the micro-wire is inserted into a 1.1 mm inner diameter glass pipette having a tip of 100 µm in diameter. Using a micromanipulator, the micro-wire is positioned in the pipette such that the sharp tip pokes out about 100 µm from the pipette tip. The

pipette tip is then closed with a drop of photoresist (PR) AZ9260. The micro-wire tip pokes out about 25-35 µm from PR. This is the length of exposed metal tip after parylene etching. Variable exposed metal tip length is obtained by controlling the length of the micro-wire poking out of PR using a micromanipulator. A stiff rod holds the micro-wire socket inside the pipette and after positioning the micro-wire, super glue is used to hold the rod in place inside the glass pipette (Figure 3.5(a)). The PR is then baked at 90˚C for 10 minutes in oven.

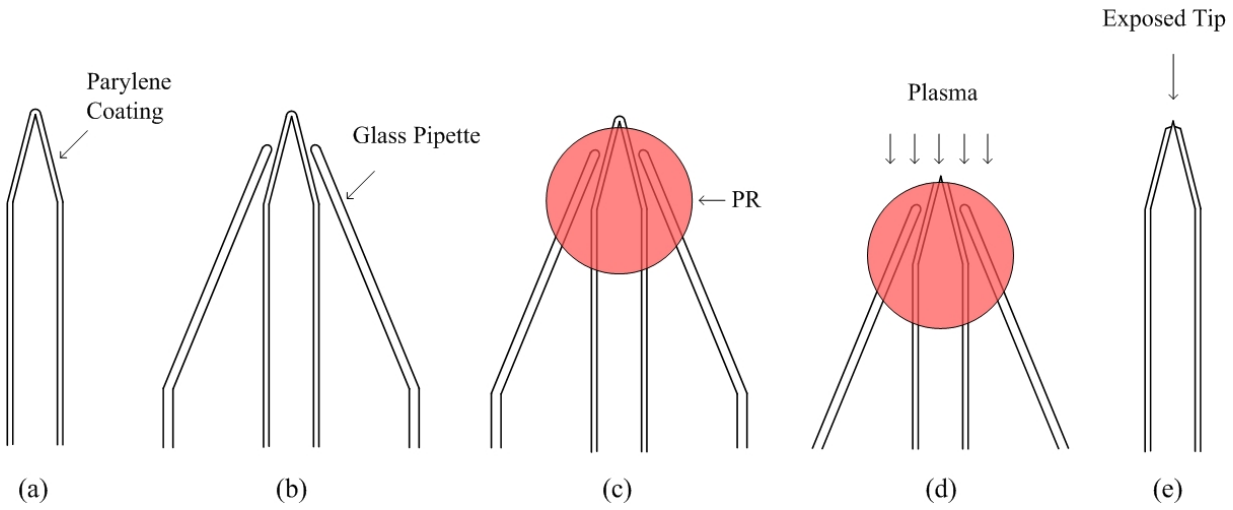

Figure 3.4 Schematics of micro-wire tip deinsulation process. (a) Electrochemically etched micro-wire. (b) Micro-wire inserted inside a glass pipette in preparation for parylene etching. (c) Pipette tip covered with PR AZ9260. Micro-wire tip pokes out of the PR. (d) Plasma etching to remove parylene from the micro-wire tip. (e) Electrode after parylene etching and PR removal.

After baking, the PR becomes hard. The pipette tip is shown in Figure 3.6(a) after baking. The PR is added to cover the pipette tip so that plasma cannot enter inside the pipette. Also, it holds the micro-wire which eliminates vibration while etching. The pipette is placed vertically with the tip facing up in the plasma RIE chamber. A custom-made glass frame (shown in Figure 3.5(b)) is used to hold the pipettes in the plasma chamber. Oxygen gas is used in the parylene etching process [63]. The parylene etching process parameters are given in Table 3.1. The etching is done in the Scifres Nanofabrication Laboratory cleanroom located at Birck Nanotechnology Center, Purdue University. The Plasma Tech RIE system has been used. Figure 3.6(b) shows the pipette tip after parylene etching. The tip of the micro-wire becomes shiny after parylene etching. The pipette is then submerged in acetone to dissolve the PR and super glue. After 30 minutes, the

socket along with the electrode is carefully taken out of the glass pipette. It is then rinsed with isopropyl alcohol and DI water, respectively. Figure 3.6(c) shows the exposed Pt sharp tip.

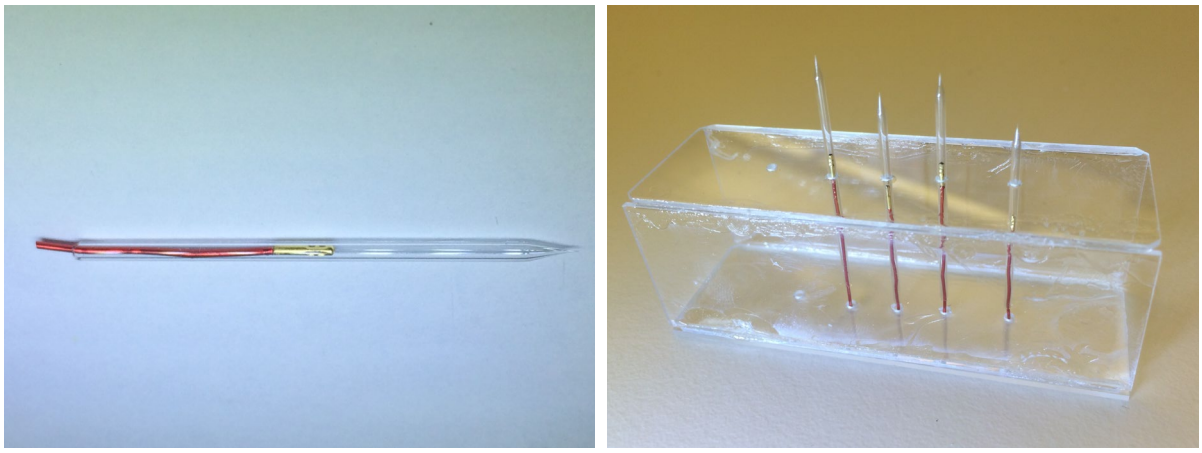

(a) (b)

Figure 3.5 (a) Micro-wire electrode inside of glass pipette. (b) A custom-made glass box holding four glass pipettes vertically ready to be put in plasma chamber.

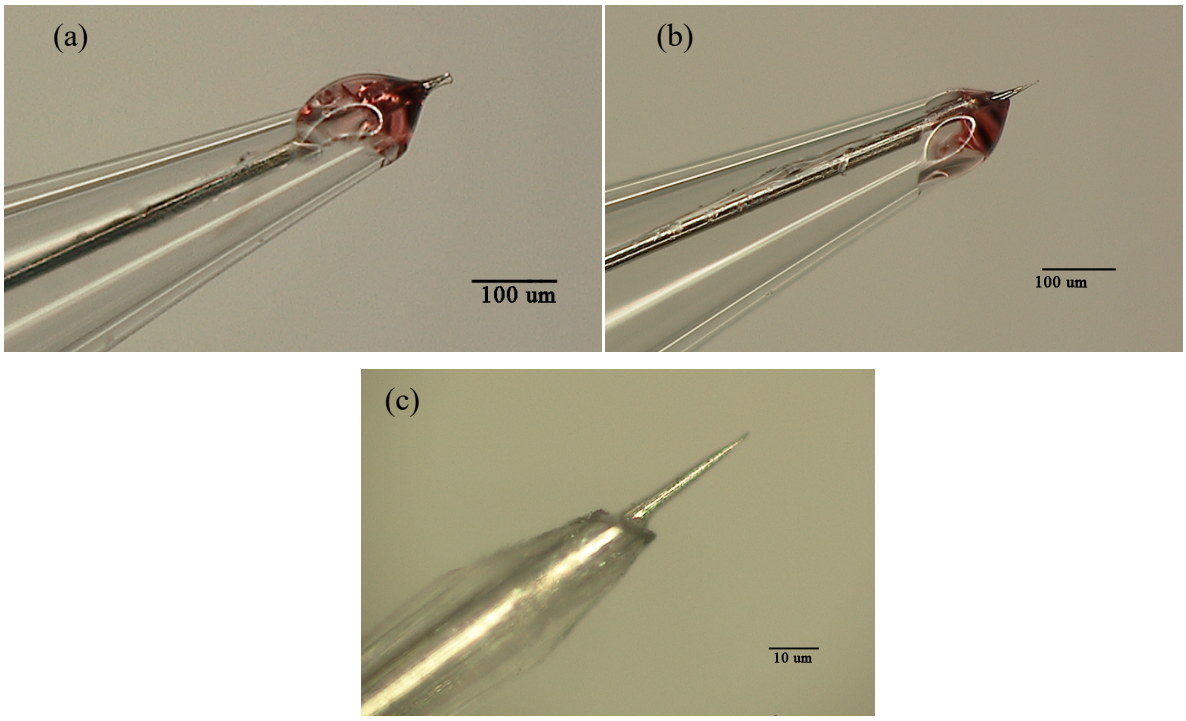

Figure 3.6 (a) Photoresist covered glass pipette tip after PR baking. Parylene coated electrode tip pokes out of PR. (b) Photoresist covered pipette tip after RIE etching. Electrode tip becomes shiny after parylene etching. (c) Sharp Pt electrode tip removed from pipette.

3.5 Helix Formation for Micro-motion Compensation

The electrode presented so far is good enough for all acute experiments and most of the chronic implantations where sufficient cement can be applied to anchor the electrode. However, in some applications, due to extensive manipulation of the connecting leads during implantation or due to dramatic movements of the rats after implantation, it is possible to displace the electrode from the neuron by few microns which are sufficient for losing the neural signal. Therefore, I have introduced a helical spring at the top of the electrode to compensate micro-motion of the anchoring base. Figure 3.7 shows the micro-motion compensated electrode. Instead of the bigger female socket (E363/0), a smaller socket is attached to the micro-wire which complies to the connecting lead of the wireless telemetry device called Bionode. The fabrication process of this electrode includes some additional steps. Before attaching the micro-wire to the socket, it is straightened and wrapped around a thicker wire to form the helical spring. Then it is attached to the socket by soldering at low temperature (550˚F). The micro-wire is trimmed to 10 mm after the spring. Figure 3.7(a) shows the electrode after this step. It contains four turns in the spring.

The micro-wire tip is then etched in $CaCl_2$ solution. After sharpening the tip, the helical spring is also etched in $CaCl_2$ solution to make it more pliable. After making it four times more pliable than an electrode having similar length and no spring, the electrode is coated with parylene C. Then I put PR in the spring and bake it at 90˚C for 20 min in oven. After baking, the electrode tip is exposed according to the procedure described in Section 3.3. The purpose of using PR in the spring is to make the spring stiff so that the electrode can be loaded in the glass pipette tube without damaging the spring. After tip deinsulation, the PR is removed using acetone. Then the spring is covered by a silicone tube to protect it during implantation. The silicone tube is attached to the socket. To increase the stiffness of the electrode for inserting in the brain, the silicone tube is filled with sucrose. After insertion and before affixing the electrode, the sucrose is dissolved by pouring few drops of sterile saline over the silicone tube. It takes couple of minutes to dissolve the sucrose. Figure 3.7(b) shows the sucrose filled micro-motion compensated single unit recording neural electrode. A comparison of the compression forces of electrodes with and without helical spring is given in Figure 3.8. It is seen from Figure 3.8 that the addition of helical spring in the electrode reduces the force by four times as stated before.

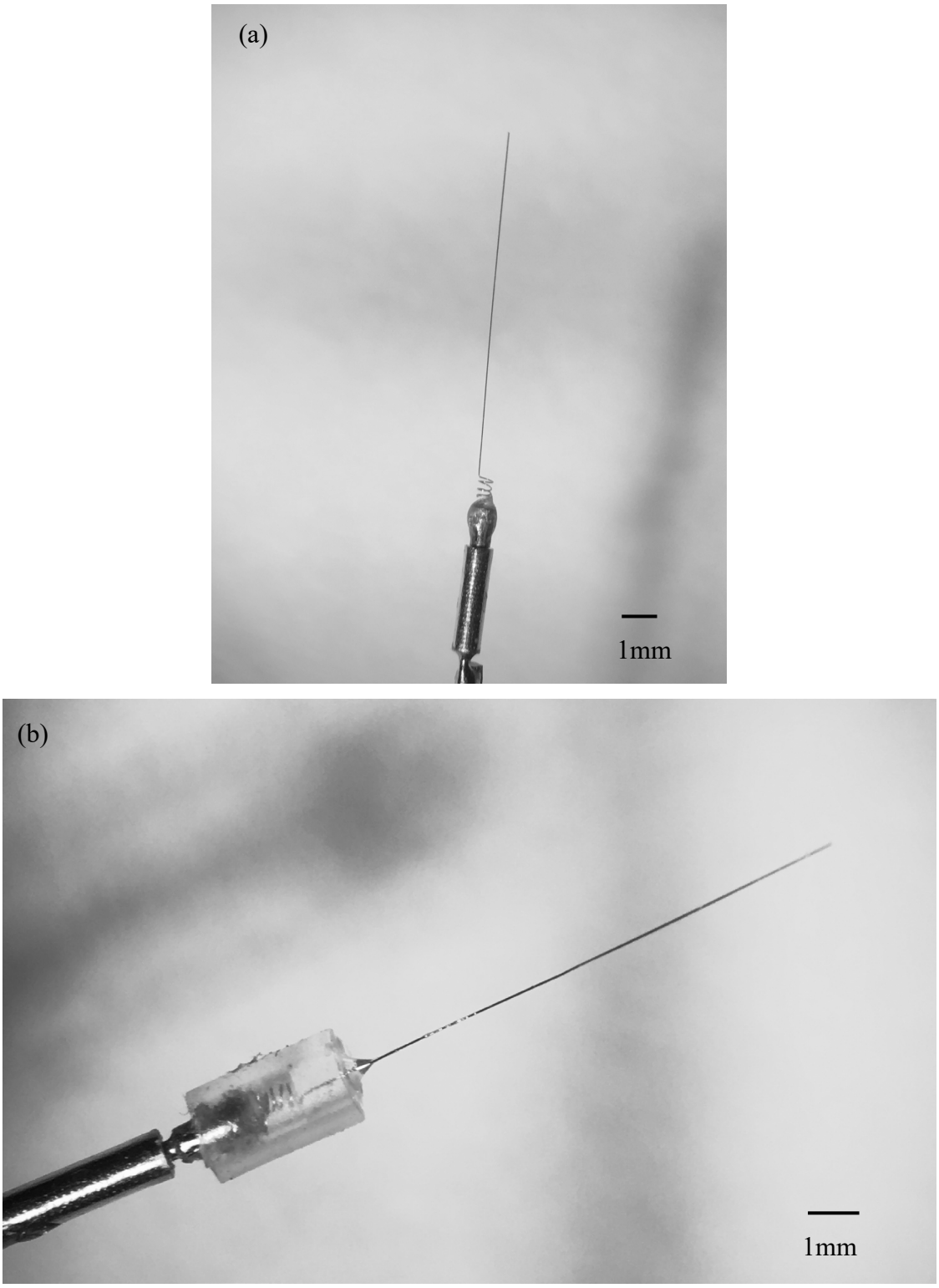

Figure 3.7 (a) Helical spring for micro-motion compensation. (b) Silicone covered and sucrose filled helical spring electrode.

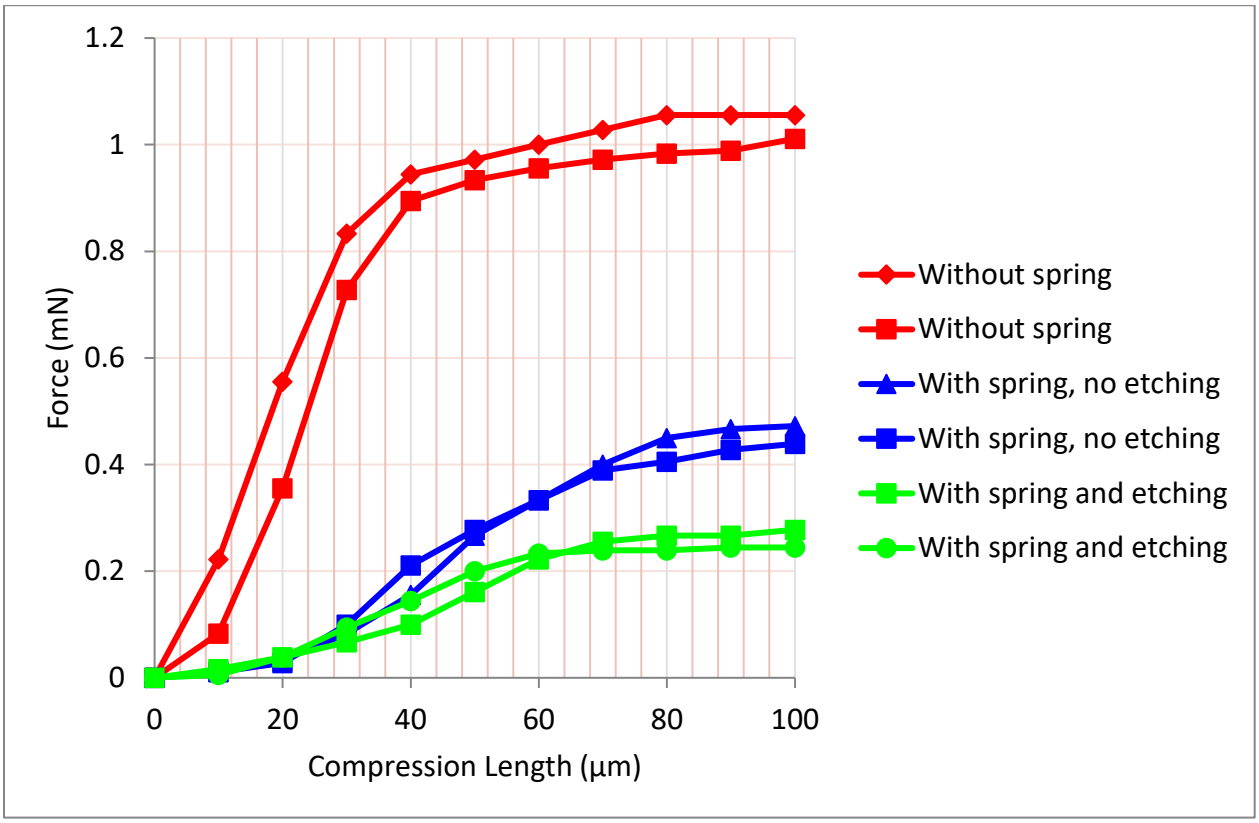

Figure 3.8 Compression forces of electrodes with and without helical spring.

3.6 Electrochemical Characterization of Electrodes

The electrochemical impedance of the electrode is measured using Gamry Instruments Potentiostat (Reference 600). Three-electrode cell configuration was used where the micro-wire Pt electrode was connected as the working electrode (WE), a larger Pt spiral wire as the counter electrode (CE) and an Ag/AgCl electrode as the reference electrode (RE) (see Figure A.1 in Appendix). Every microelectrode was characterized in a phosphate buffered saline solution (PBS 1x) by electrochemical impedance spectroscopy (EIS) (100 KHz to 10 Hz). Figure 3.9 shows the electrochemical impedance of a typical microelectrode.

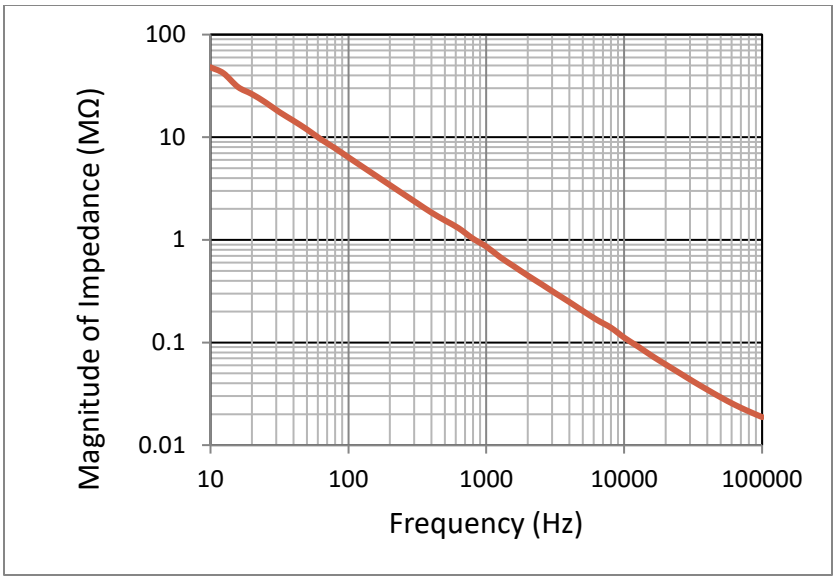

(a)

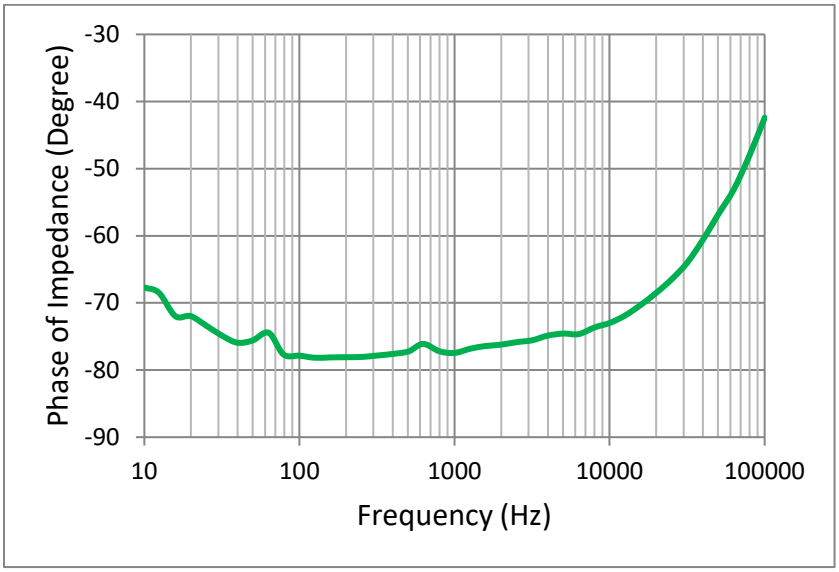

(b)

Figure 3.9 Electrochemical impedance of the fabricated Pt microelectrode. (a) Magnitude of impedance. (b) Phase of impedance.

4. DESIGN AND PROTOTYPE DEVELOPMENT OF THE MICROELECTRODE INSERTER

4.1 Overview

Manual insertion (i.e. insertion by hand) of the micro-wire electrode is not possible because of its flexibility and the precise positioning required in finding and holding a desired neuron. Therefore, an insertion device is necessary to implant this electrode. Since such a device does not exist, I have proposed the design of the microelectrode inserter and developed a prototype of the proposed inserter. This section presents my design of the motorized electrode inserter and describes its working principal.

4.2 Design of the Microelectrode Inserter

The proposed inserter consists of 4 major parts: digital Vernier caliper, insertion motor, spinner motor and the electrode guide. The last 3 parts are mounted on a digital Vernier caliper obtained from AccuRemote, San Clemente, CA, USA (PN: 35-812). Figure 4.1 shows a 3D model of the proposed microelectrode inserter. The model is designed in Fusion 360 and the mounting parts are fabricated in FDM 3D printer using ABS material. The insertion motor is a variable speed DC gear motor (obtained from Uxcell, Kwai Fong, Hong Kong, PN: a14052900ux0148) that drives the electrode up and down. Linear motion is obtained by using a 100 mm long and 6 mm diameter lead screw with 1 mm pitch. The spinner motor is a variable speed DC servo motor (obtained from FEETECH RC Model Co., Ltd., PN: FS90R) that spins the electrode during insertion. The electrode is attached to the spinner motor shaft using a holder shown in Figure 4.2. The electrode holder is made of a 0.5 mm diameter stainless steel conductor with a non-conductive motor shaft coupler. The other end of the holder plugs into the electrode socket (E363/0). A custom-made socket, as shown in Figure 4.2, is used as a slip ring. The insertion motor is attached to the caliper and the spinner motor is attached to the movable Vernier scale. The Vernier caliper has a digital LCD display which shows the position of the Vernier scale. When the insertion motor is on, it slides the Vernier scale over the fixed frame and the LCD display shows the new position of the Vernier scale. Since the electrode is attached to the spinner motor and the spinner motor is situated on the Vernier scale, the position of the Vernier scale can

be treated as the position of the microelectrode. The resolution of the digital LCD display for position measurement is 10µm. Therefore, the smallest measurable motion of the microelectrode is 10µm. However, by regulating the supply voltage to the insertion motor, insertion step size as small as 4 µm is achievable.

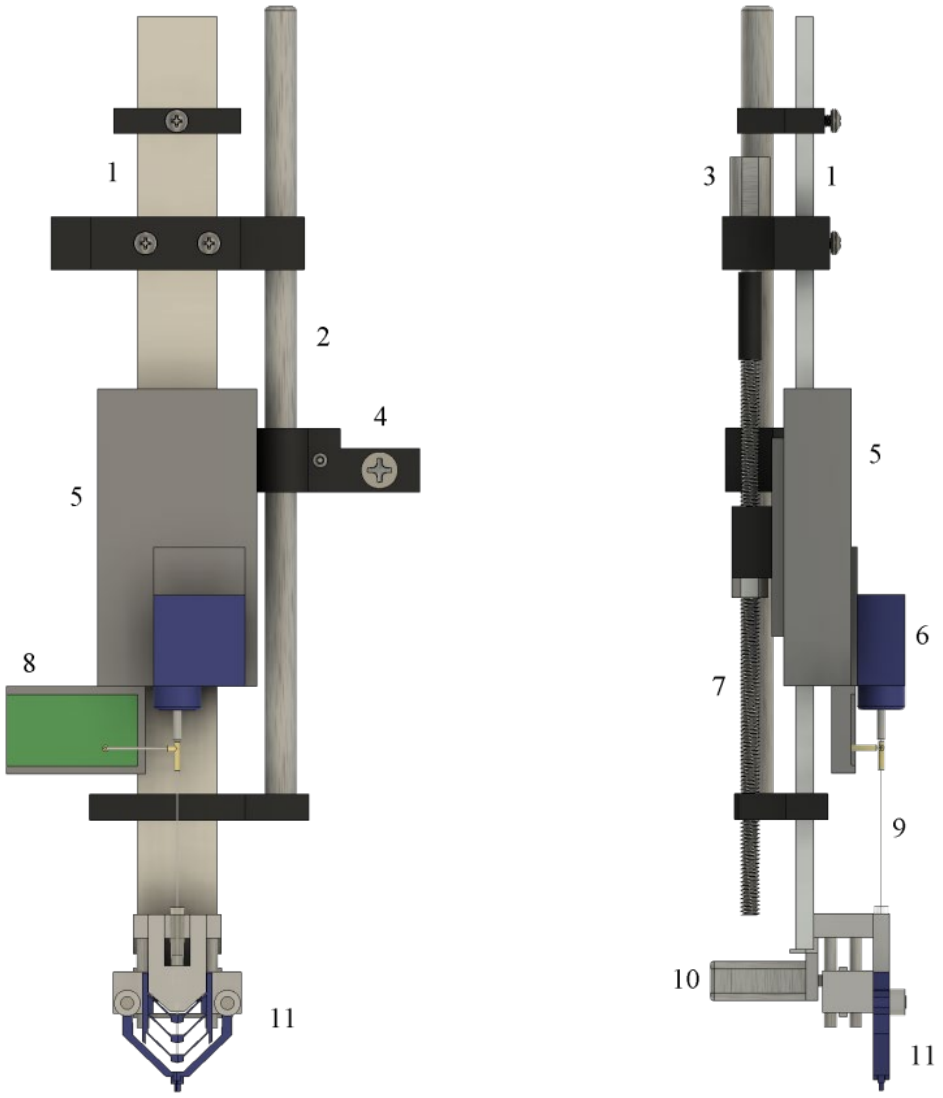

(a) (b)

Figure 4.1 3D model of the microelectrode inserter designed in Fusion 360. (a) Front view of the inserter. (b) Side view of the inserter. [1- Caliper Frame, 2- Support Rod, 3- Insertion Motor, 4- Stereotaxic Arm Clamp, 5-Movable Vernier Scale, 6- Spinner Motor, 7- Lead Screw, 8- Neural Amplifier Board, 9- Electrode Holder, 10- Guide Lifting Motor, 11- Electrode Guide] © [2019] IEEE Reprinted with permission from [57].

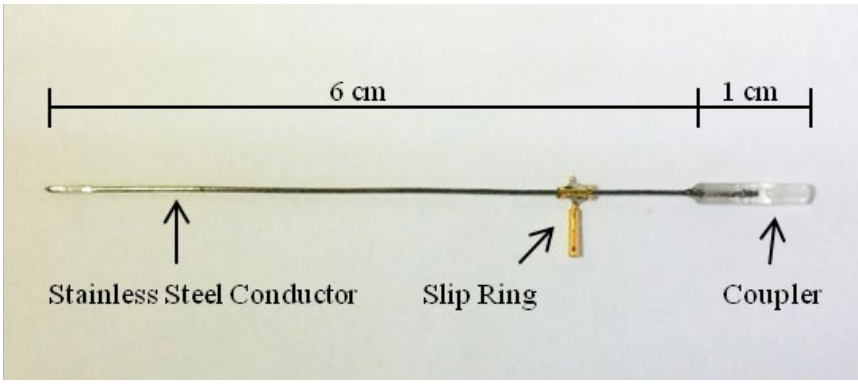

Figure 4.2 Fabricated electrode holder. © [2019] IEEE Reprinted with permission from [57]

4.3 Design of the Electrode Guide

One of the basic components of the proposed electrode insertion method is the electrode guide which is located at the bottom of the caliper (Figure 4.1). The guide is demonstrated in Figure 4.3 by inserting an electrode into agar gel. The top 3 pairs of arms are semi-flexible and the bottom arms are rigid. Figure 4.3(a) shows the state of the guide and the position of the electrode before insertion. The rigid arms and the lower two pairs of the semi-flexible arms are closed and surround the electrode wire. The top semi-flexible arms are open because of the electrode socket. The electrode is spun and slowly inserted in the agar gel through the guide. While inserting the electrode, the semi-flexible arms open up one by one as the electrode socket pushes them downward. Figure 4.3(b) shows the position of the electrode in the guide after insertion. The electrode is in the agar gel and the electrode socket is above the rigid arms. The rigid arms are then retracted, as shown in Figure 4.3(c), to release the electrode. Figure 4.3(d) shows a computerized tomography (CT) image of the microelectrode inserted 10 mm in agar gel. The semi-flexible arms are attached to the frame but the rigid arms are mounted on a support which can slide up and down. The up-down movement of the rigid arms is controlled by a motorized cam-wheel system shown in Figure 4.3(e) and 4.3(f). The cam-wheel is designed to provide 4 mm vertical displacement with 180˚ rotation. While retracting the rigid arms, the extruded rigid frame (Figure 4.3(f)) restricts the motion of the rigid arms and forces them to rotate. In this way, the rigid arms open up to make space for fastening the electrode in in-vivo experiments without dislodging the electrode.

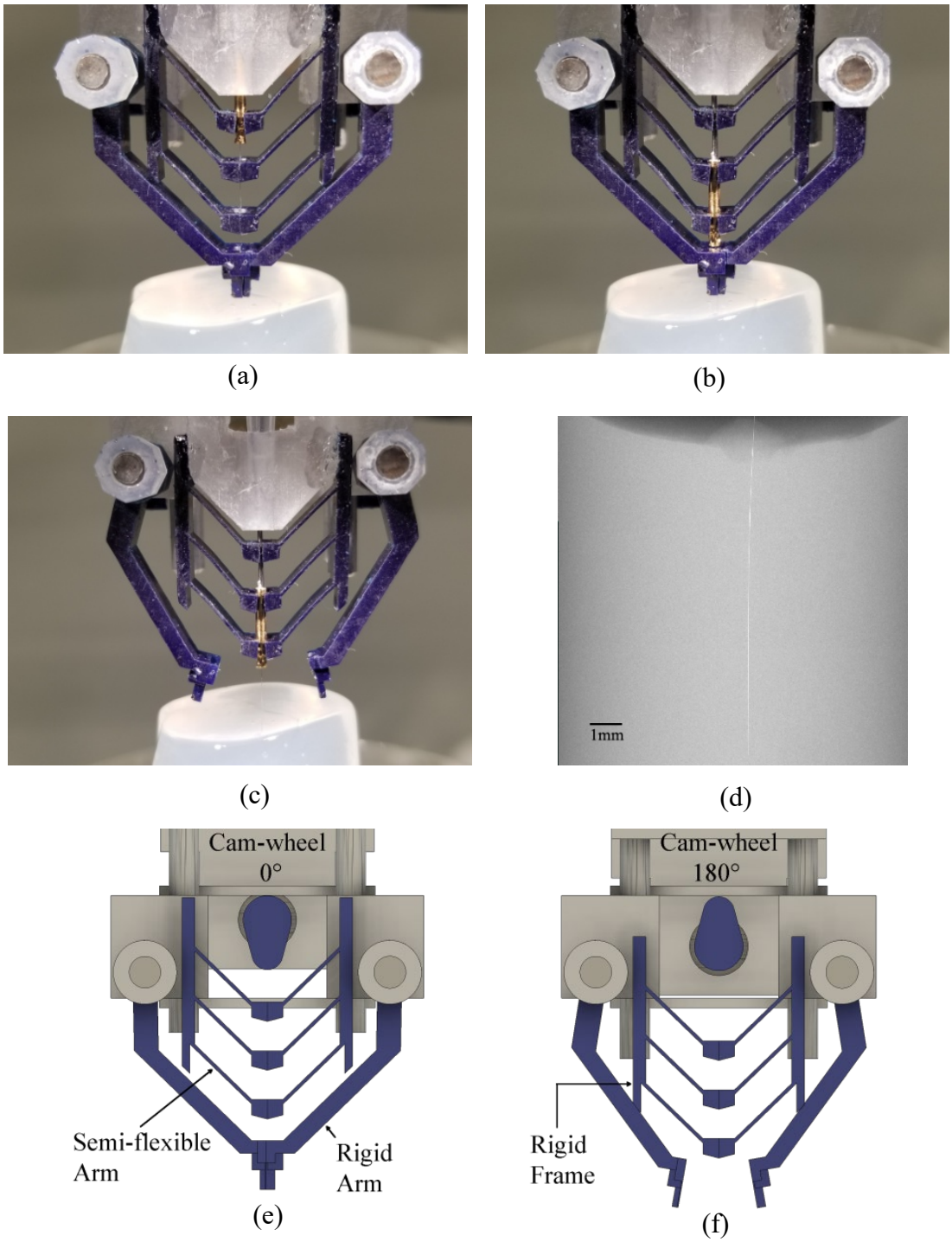

Figure 4.3 Demonstration of the electrode guide. The state of the guide and the position of the electrode - (a) before and (b) after insertion. The semi-flexible arms open up one by one as the electrode socket pushes them downward. (c) Opening of the rigid arms after insertion. (d) CT image of the inserted electrode in agar gel. The electrode appears as a thin white line in the image. (e) 0˚ position of the cam-wheel when rigid arms are closed. (f) 180˚ position of cam-wheel to retract and open the rigid arms. © [2019] IEEE Reprinted with permission from [57]

At the ends of the arms, there are micro-holes each with the shape of a half cone, so that when two arms touch end to end, they make a complete conical micro-hole as shown in Figure 4.4. In addition to the conical micro-hole, the rigid arms, when closed together, create a 3 mm long micro-ferrule below the conical hole. This particular guide design ensures perpendicular penetration in the brain, restricts the electrode from buckling during insertion, and minimizes friction between the electrode and the guide, thus providing better insertion force. The height of the micro-ferrule including the conical hole is 4 mm and the rigid arms retract by 2 mm before opening. Therefore, the electrode has to be 6 mm longer than the depth of insertion. The electrode guide is fabricated in a 10 µm resolution Autodesk Ember SLA 3D printer.

The fabricated prototype electrode insertion device is shown in Figure 4.6. The device is fabricated in the Center for Implantable Devices (CID) at Purdue University, West Lafayette, IN.

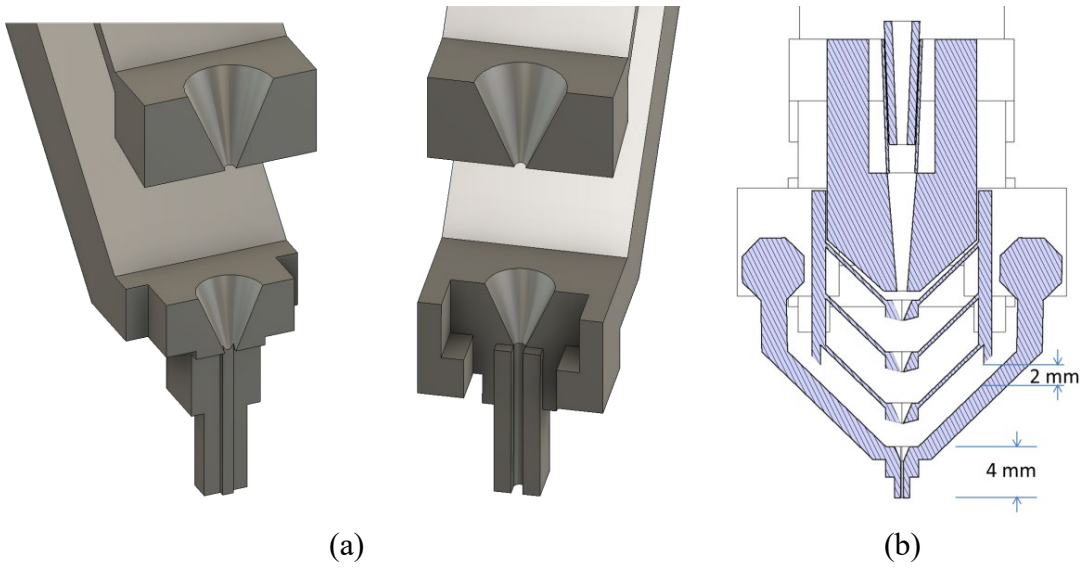

Figure 4.4 (a) Conical holes at the ends of the guide arms. (b) Cross sectional view of the electrode guide at mid-plane. © [2019] IEEE Reprinted with permission from [57]

4.4 Control Panel

The electrode inserter has a control panel to operate it during electrode insertion. The device is battery operated. A simplified block diagram of the control system is shown in Figure 4.5. It has two rotary knobs, one single pole double throw (SPDT) switch, one single pole single throw (SPST) switch, and two liquid crystal display (LCD) displays on the panel. The insertion motor speed is controlled by one rotary knob and the spinner motor speed is controlled by the other rotary knob. When the knobs are turned to zero, the corresponding motions stop. The rigid arms of the electrode guide are lifted up and down by the SPDT switch. The device is turned on and off using the SPST switch. The rotational speed of the electrode during insertion is displayed on one LCD screen and the insertion depth is displayed on the other LCD screen. The position of the electrode is read out from the Vernier scale and displayed on the screen. An infrared sensor is used to measure the rotational speed of the electrode. The rotational speed is calculated from the number of square pulses obtained per second from the IR sensor. An Arduino Uno micro-controller board is used for doing the calculations and running the LCD screens. The entire system is powered from two 9 V batteries (±9 V) placed inside the controller. The control panel is shown in Figure 4.6.

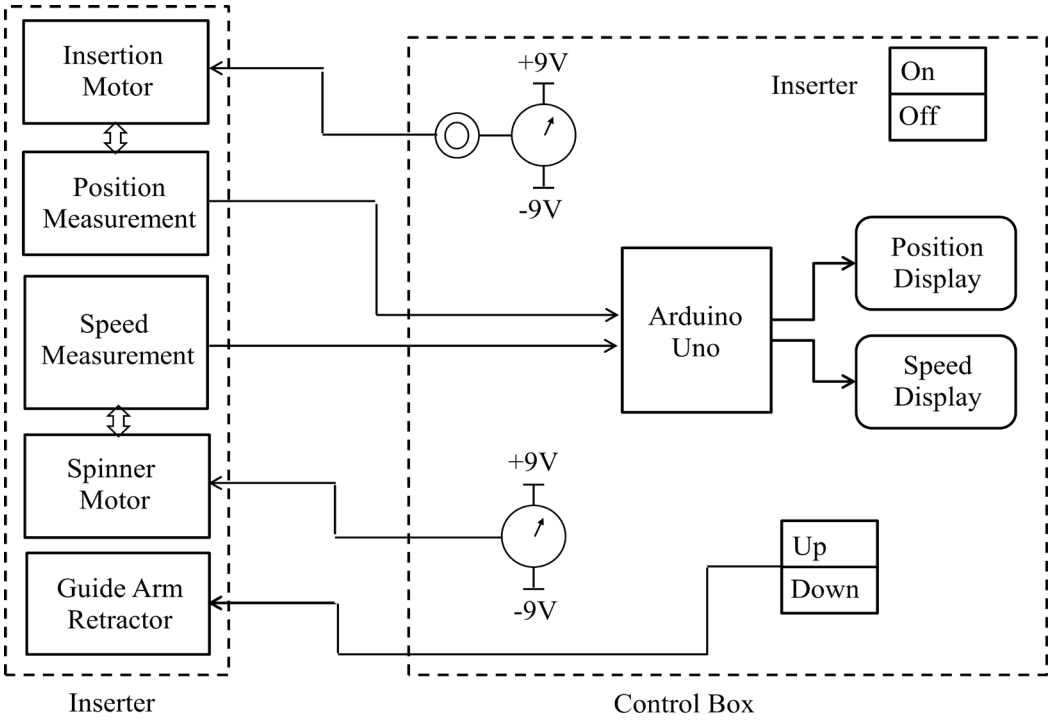

Figure 4.5 Block diagram of the inserter control system

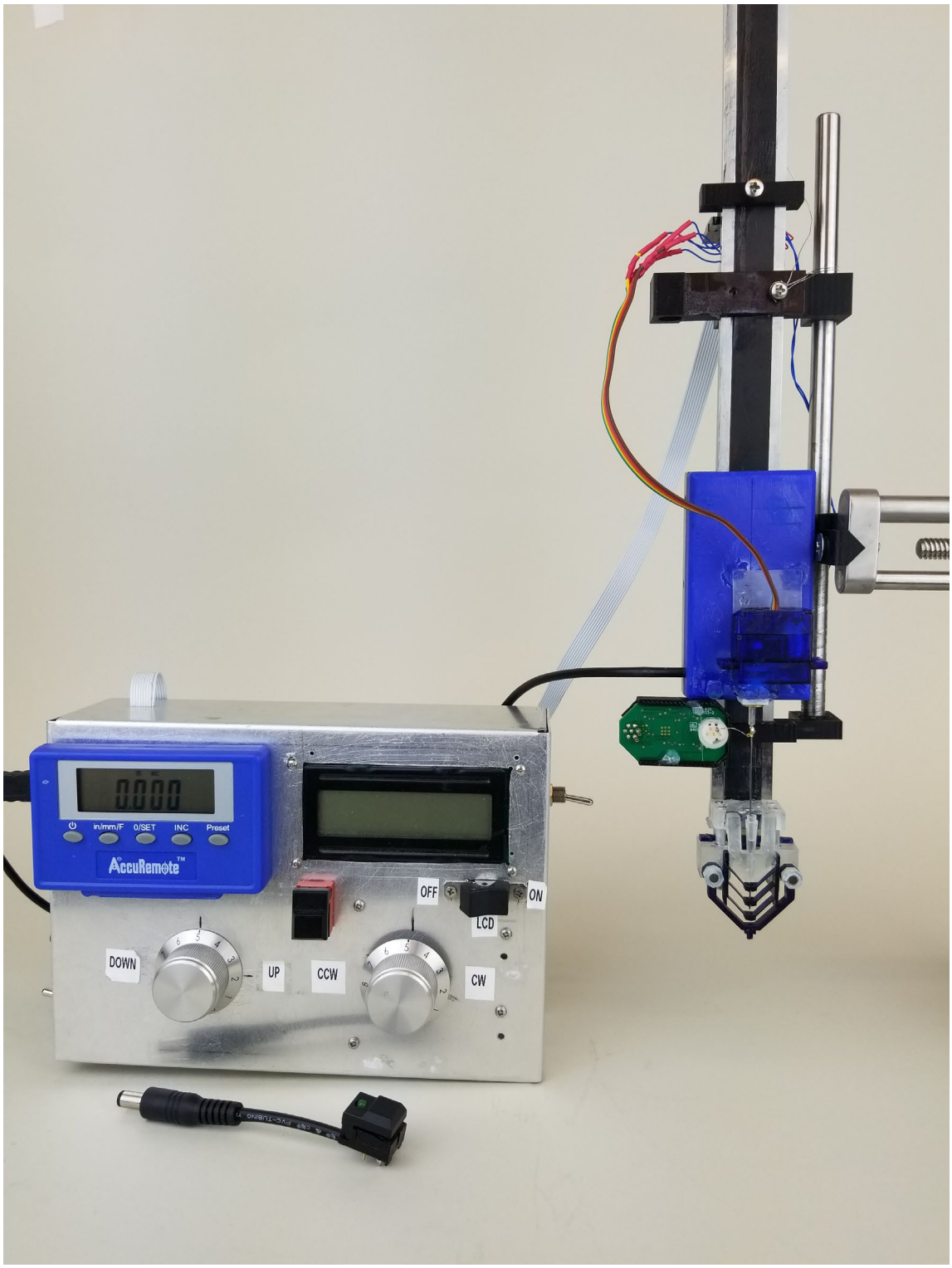

Figure 4.6 Prototype of the developed ultra-thin flexible microelectrode inserter. © [2019] IEEE
Reprinted with permission from [57]

5. NEURAL SIGNAL RECORDING CIRCUIT: 16 CHANNEL PROGRAMMABLE NEURAL AMPLIFIER IC DESIGN

5.1 Neural Amplifier IC Design

In order to record microvolt neural spikes with high signal-to-noise ratio (SNR) and amplify them with appropriate bandwidth, a low noise neural amplifier is required. Neural amplifier made from off the shelf components has poor common mode rejection ratio (CMRR) and noise performance. Therefore, a low noise neural amplifier integrated circuit (IC) has been designed and fabricated. Figure 5.1 shows the schematics of the design of neural amplifier. The amplifier has 16 input channels. All the channels are differential. The outputs of the channels are multiplexed and a single output is provided. Four digital control pins (M0-M3) are used to select the channels. The 16 inputs are divided into two groups. These two groups are independently programmable to tune for different gain and bandwidth setting. Eight input pins are used to program each group of channels. Among them, S1-S2 are used for gain setting, S3-S6 for low pass cut off setting and V1-V2 for high pass cut off and roll off settings. The control parameter settings are provided in Table A.1 in Appendix.

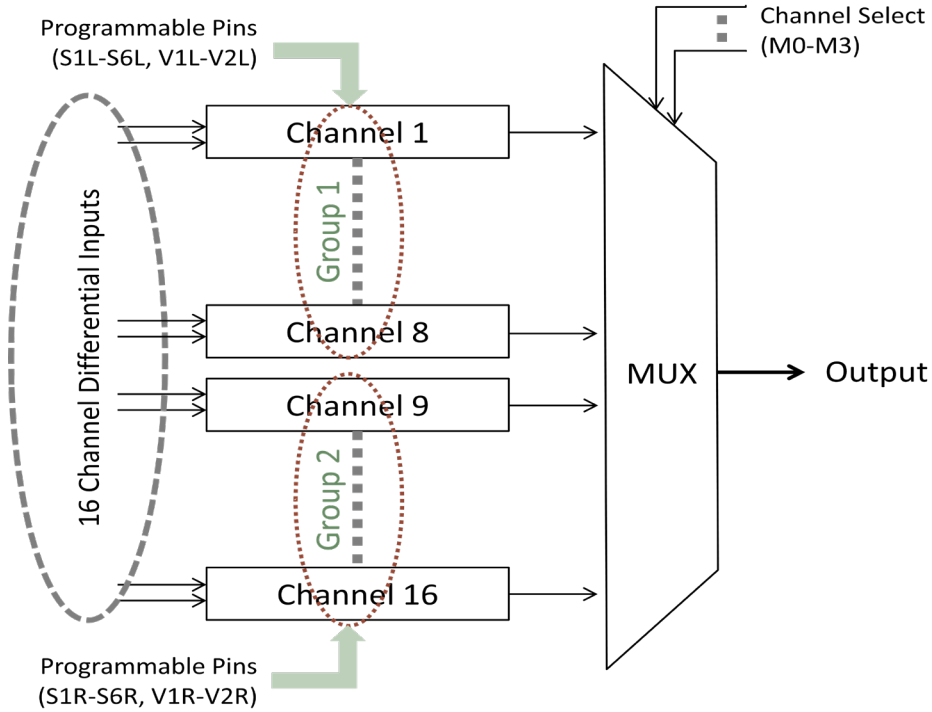

Figure 5.1 Schematics of the 16-channel programmable neural amplifier.

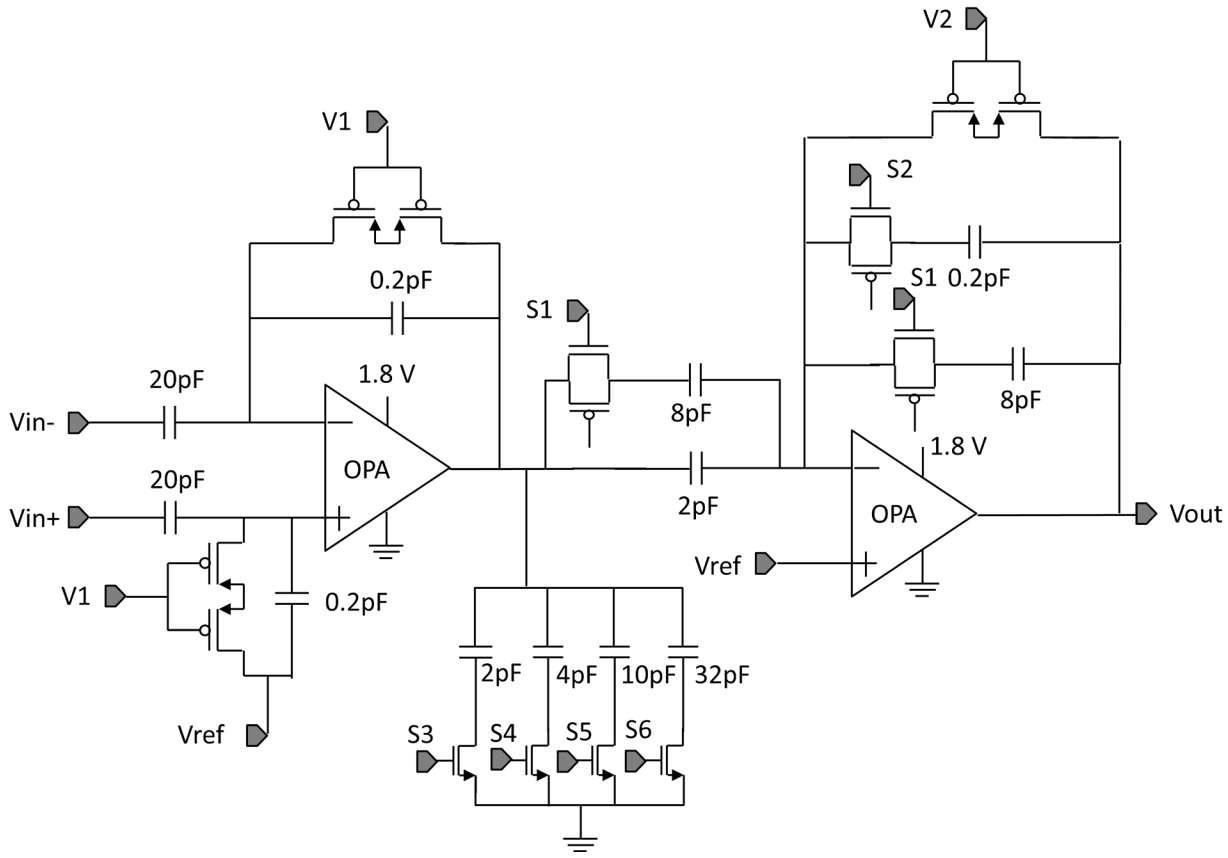

Figure 5.2 Schematics of a single channel programmable neural amplifier.

The schematic of the circuit diagram of the individual single channel amplifier is shown in Figure 5.2. The amplifier consists of two stages. The first stage provides a voltage gain of 100 (40 dB). The second stage provides an additional voltage gain of either 1.25 or 10 depending on the control settings (see Table A.1 in appendix) and a tunable high pass filter cut off frequency. Therefore, the overall voltage gain of the amplifier is 125 (42 dB) or 1000 (60 dB). The voltage gain, A of each stage is given by the following equation:

$$A = \frac{Vo}{Vi} = \frac{C_s}{C_p} \tag{5.1}$$

where, V_o is the output voltage, V_i is the differential input voltage, C_s is the input capacitor and C_p is the feedback capacitor. The transfer characteristic of the amplifier is shown in Figure 5.3.

The amplifier is capacitively coupled to the electrodes to eliminate DC input voltage and any unwanted low frequency baseline fluctuations.

Measurement Conditions

Gain 42dB	
S1	1
S2	0
S3	1
S4	0
S5	0
S6	0
V1	1.5V
V2	1.5V

Gain 60dB	
S1	0
S2	1
S3	1
S4	0
S5	0
S6	0
V1	1.5V
V2	1.5V

0 = Low 1 = High

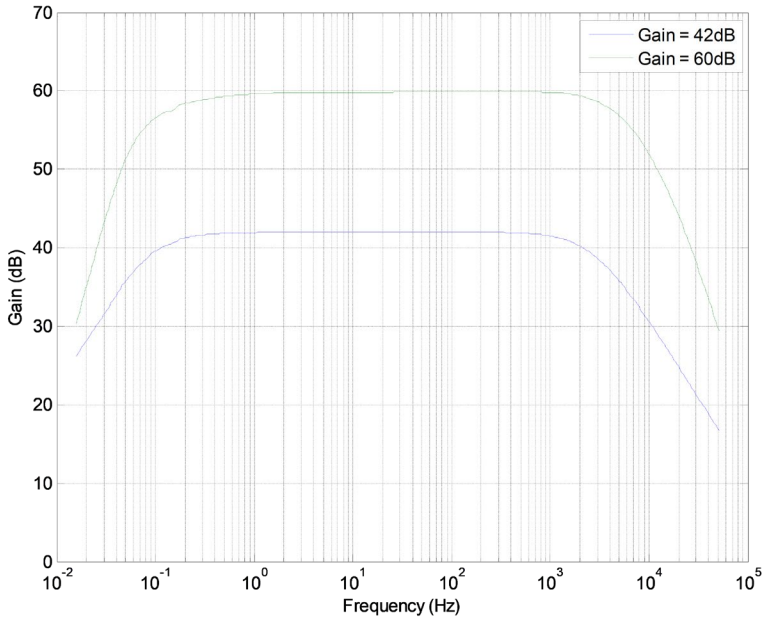

Figure 5.3 Transfer characteristics of the neural amplifier. The amplifier can be programmed to provide either 42 dB or 60 dB gain. The measurements are taken using Agilent 35670A dynamic signal analyzer.

The high pass filter cut off frequency, f_L is given by the following equation:

$$f_L = \frac{1}{2\pi R C_S} \tag{5.2}$$

where, R is the pseudo resistance. The tunable cut off frequency is obtained by varying the pseudo resistance. The pseudo resistance is realized by two p-type MOSFETs connected as depicted in Figure 5.2 and is known as pseudo-resistance [64-66]. Variable resistance is obtained by tuning the gate voltage V_2. Increase in the gate voltage of the pMOS increases the channel resistance and, therefore, decreases the cut off frequency. Figure 5.4 shows the variation of the high pass filter cut off frequency with the second stage gate voltage V_2. The first stage also provides a tunable high pass filter cut off frequency. By tuning both stages, both 20 db/decade and 40 db/decade roll offs can be achievable as shown in Figure 5.5. Variation in the low pass

filter cut off frequency is obtained by connecting various capacitances at the output of the first stage. Figure 5.4 shows the variation of the low pass filter cut off frequency by changing capacitances. Increase in capacitance decreases the cut off frequency.

The values of the cut off frequencies for various control parameter settings are provided in Appendix. While continuous variation is possible for high pass filter cut off frequency, the low pass filter cut off frequency can have 16 discrete values.

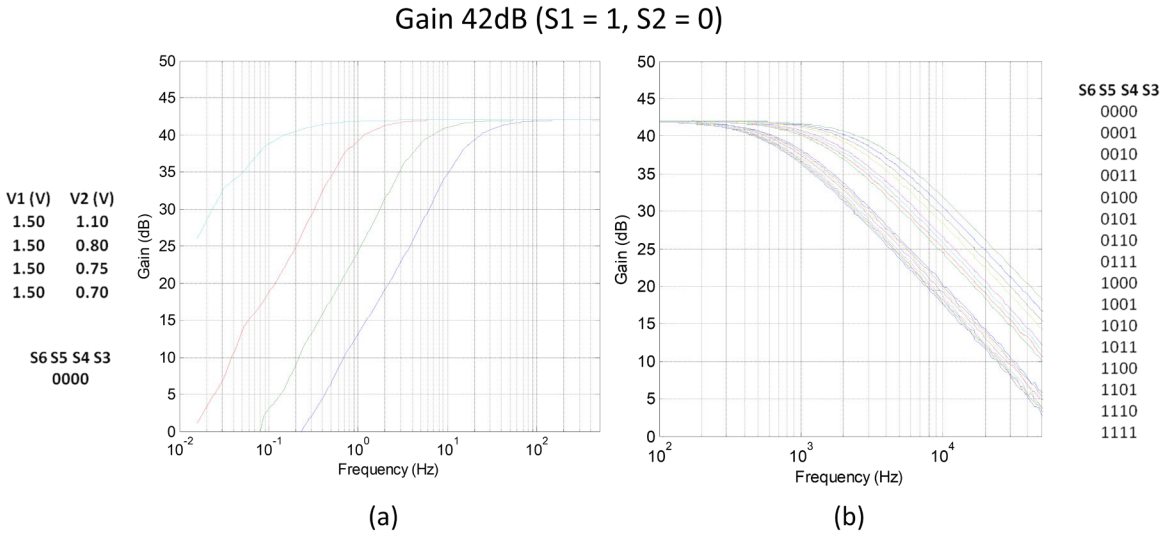

Figure 5.4 (a) Variation of high pass filter cut off frequency. (b) Variation of low pass filter cut off frequency. The measurements are taken using Agilent 35670A dynamic signal analyzer.

Gain (dB)	Roll off (db/decade)	V1 (V)	V2 (V)
42	20	1.50	0.70
	40	0.80	0.70
60	20	1.5	0.78
	40	0.78	0.78

S6 S5 S4 S3 S2 S1
0 0 0 0 0 1

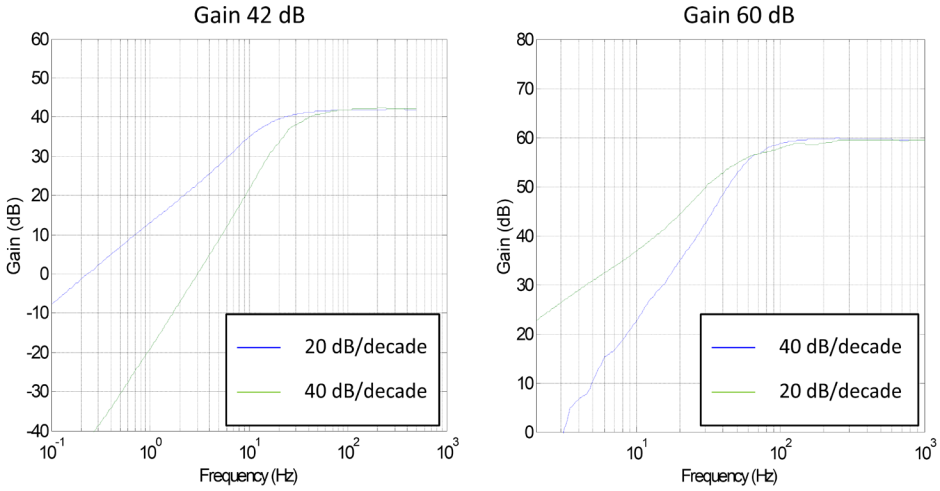

Figure 5.5 Two different high pass roll off of the neural amplifier. The measurements are taken using Agilent 35670A dynamic signal analyzer.

The basic building block of the neural amplifier is the operational amplifier (OPAMP). OPAMPs are made of metal oxide semiconductor field effect transistors MOSFETs (M). Different architectures are used to design an OPAMP. Two-stage Cascode architecture is widely used in circuit design at places where high gain and high output impedance are required. Folded Cascode architecture provides better performance than the Cascode OPAMP circuit [67]. Therefore, I have used the Folded Cascode architecture to design my OPAMP. The schematic of the OPAMP circuit is given in Figure 5.6. An ideal OPAMP has infinite open loop gain and, therefore, the gain of the designed OPAMP should be as large as possible. The open loop voltage gain, A_v of the OPAMP can be derived as

$$A_v = \frac{v_{out}}{v_{in+} - v_{in-}} = -\frac{v_{out}}{2v_{in-}} = \frac{1}{2} g_{m4}[(g_{m12} r_{o12}(r_{o4}||r_{o14})\}||(g_{m10} r_{o10} r_{o8})] \quad 5.3$$

From the equation, we see that the voltage gain, A_v depends on the transconductance, g_{m4} and on the products $g_{m12}r_{o12}$ and $g_{m10}r_{o10}$. To increase the gain, we can increase these three terms.

Since, $g_m = \sqrt{2\mu_n C_{ox} \frac{W}{L} I_D}$ and $r_o = \frac{1}{\lambda I_D} \propto \frac{L}{I_D}$,

$$g_m r_o = \sqrt{2\mu_n C_{ox} \frac{W}{L} I_D} * \frac{1}{\lambda I_D} \propto \sqrt{2\mu_n C_{ox} \frac{WL}{I_D}} \quad 5.4$$

Power consumption is an important design criterion of the neural amplifier. In future, this neural amplifier will be used in implantable devices where available energy is very limited. Therefore, the amplifier is designed to consume power as less as possible. Thus, the drain current, I_D cannot be increased. For a fixed drain current, we can increase both width (*W)* and length (*L)* of transistors M_9-M_{12} keeping the *W/L* ratio fixed so that the overdrive voltages remain the same. At the same time, we can increase g_{m4} by increasing its width. In this way, I have increased the gain.

Low noise is another important criterion for recording neural spikes. Spike amplitude can be as low as 10 μV. Therefore, the noise level at the amplifier output should be low enough to detect the spike from the baseline noise. The output noise is inversely proportional to size of the input

MOSFET. Therefore, I have increased the size of M_3 and M_4 as much as possible. The sizes of all the MOSFETs in the OPAMP are shown in Table 5.1.

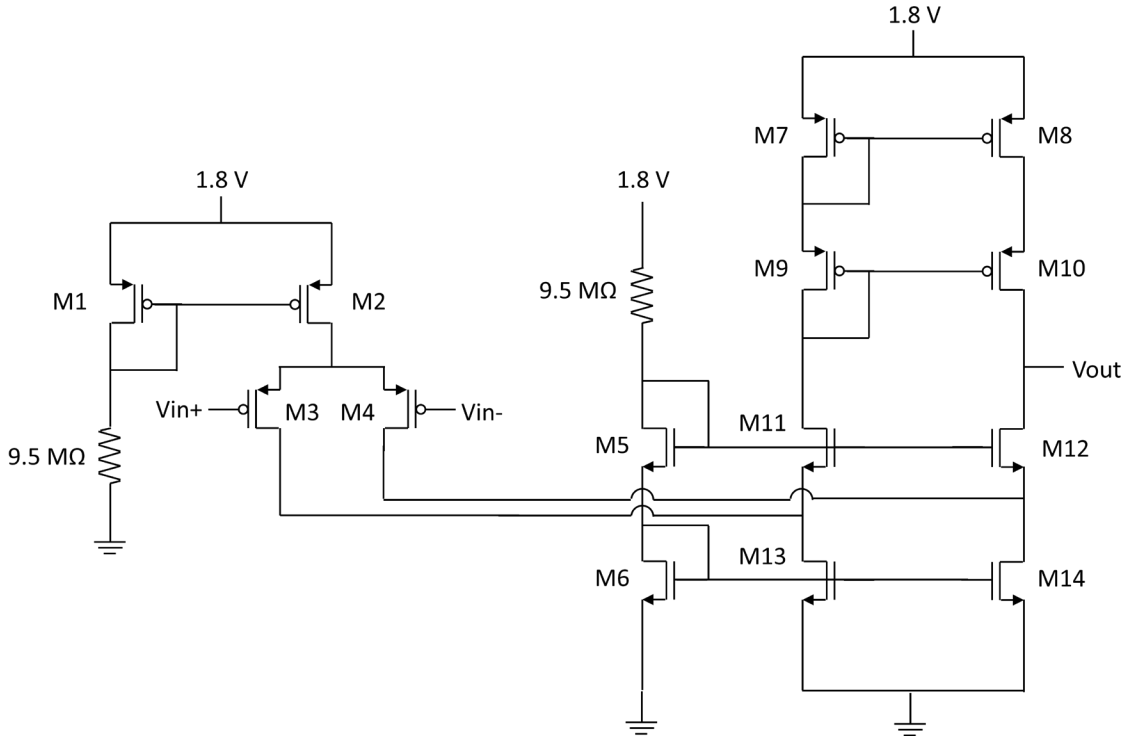

Figure 5.6 Schematics of a folded Cascode differential input single ended output OPAMP.

Table 5.1 Size of the MOS transistors in the OPAMP

Transistor Name	Gate Length, L_g	Gate Width, W_g	No. of Gates	No. of Multiplier
M1	10	1	1	1
M2	10	1	10	2
M3, M4	4	40	10	1
M5	10	2	1	1
M6	20	1	1	1
M7 - M10	10	5	4	1
M11, M12	10	2	5	2
M13, M14	20	1	2	10

5.2 ASIC Design and Fabrication

The 16-channel neural amplifier integrated circuit (IC) has been designed and simulated in Cadence Virtuoso using 180nm CMOS process from ON Semiconductor. It has been sent to ON Semiconductor for fabrication and the fabricated application specific integrated circuit (ASIC) is shown in Figure 5.7.

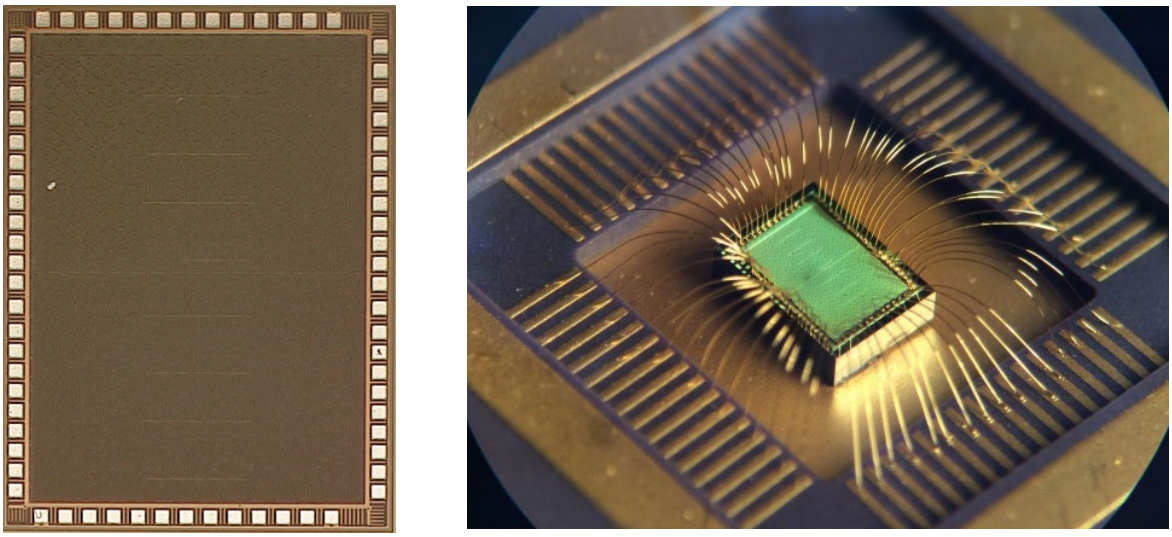

(a) (b)

Figure 5.7 (a) Fabricated 16 channel neural amplifier ASIC. (b) ASIC is wire bonded to a 64-pin socket for characterization.

The layout of the amplifier IC is shown in Figure 5.8. The size of the chip is 2.8mm x 2mm. For the resistor, rppolyhr was used and the metal-insulated-metal (MIM) capacitor was used for the capacitor.

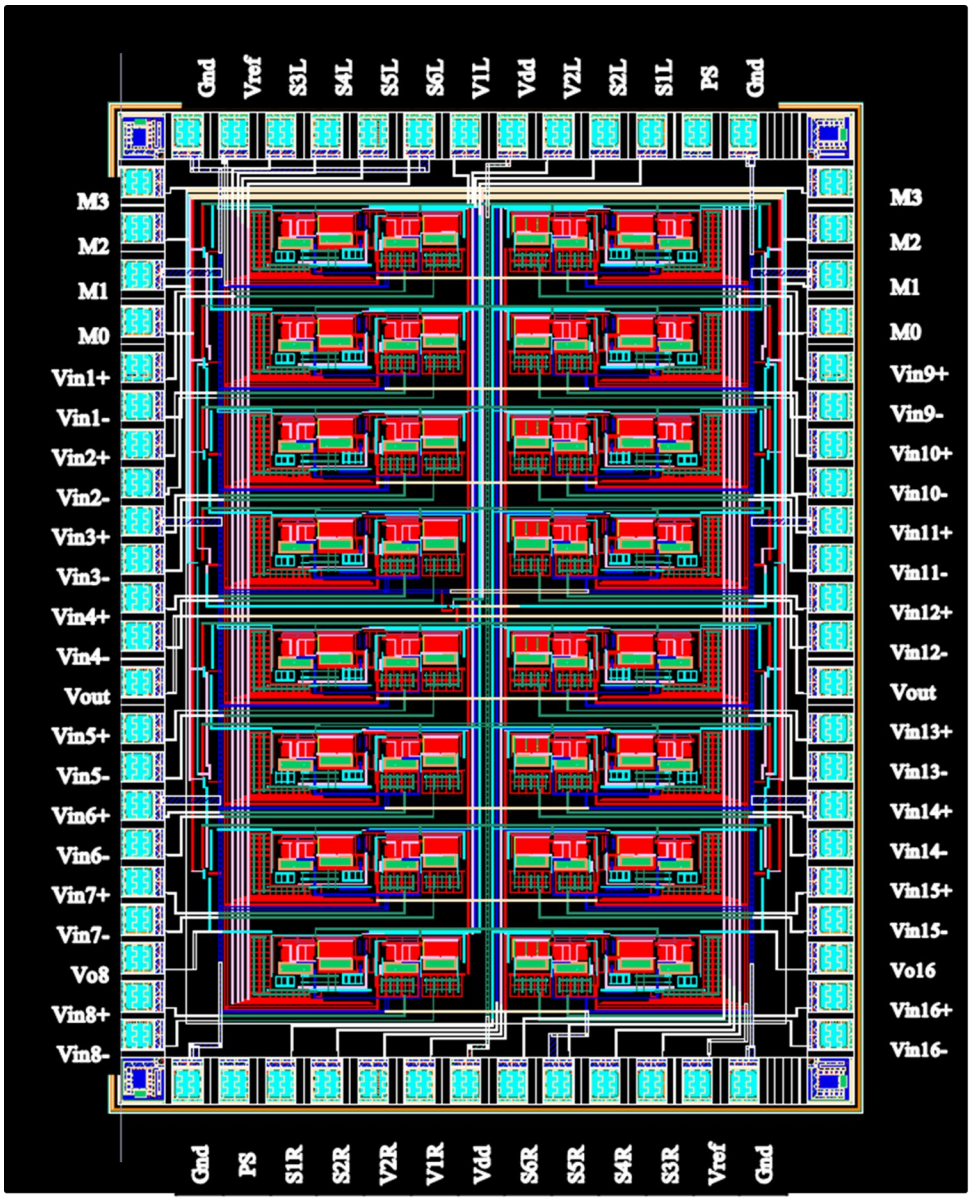

Figure 5.8 Layout of the 16 channel programmable neural amplifier designed in Cadence Virtuoso using 180 nm CMOS technology from ON Semiconductor.

5.3 Performance Characterization

The fabricated IC has been characterized using Agilent 35670A dynamic signal analyzer and Agilent E4980AL LCR Meter and the results are given in Table 5.2 along with the performance of the state-of-the-art neural amplifiers. The input referred output noise and the total harmonic distortion are shown in Figure 5.9 and 5.10 respectively. Time domain output waveforms are shown in Figure A.2 in Appendix.

Table 5.2 Performance characteristics of the neural amplifier

Parameter	This Work	[68] TBCS 2011	[69] TBCS 2013	[70] TCS 2013	[71] JSSC 2014
Gain	42, 60 dB	49-66 dB	400, 600	60.9 dB	30-4000
Bandwidth	Tunable	Fixed	Tunable	Fixed	Tunable
CMRR	82 dB	62 dB	73 dB	60 dB	60
Input Referred Output Noise	3.45 µVrms	5.4 µVrms	3.2 µVrms	4 µVrms	3.2 µVrms
PSRR	74 db	72 dB	80 dB	70 dB	76 dB
Supply Voltage	1.8 V	1.8 V	1.8 V	1.8 V	1.8 V
Input Impedance	>100 MΩ	-	-	-	-
Power Consumption	13.43 µW/ch	10.1 µW/ch	9.4 µW/ch	11.6 µW/ch	27.8 µW/ch
Total Harmonic Distortion	0.076% @42dB; 0.186% @60dB	-	0.53%	1%	1 %
Output Range	1 V	-	-	-	-
No. of Channels	16	32	100	100	52
Area Per channel	0.35 mm^2	0.31 mm^2	0.25 mm^2	0.28 mm^2	0.18 mm^2
Process Technology	180 nm CMOS	180 nm CMOS	180 nm CMOS	180 nm CMOS	180 nm CMOS

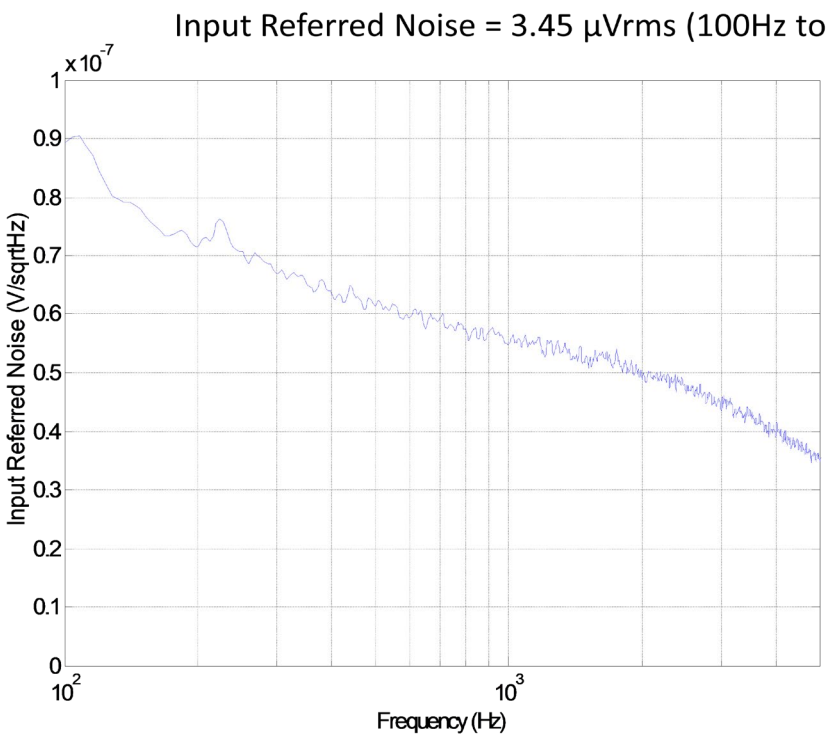

@Gain 60dB	
S1	0
S2	1
S3	1
S4	0
S5	0
S6	0
V1	1.5V
V2	1.5V

Figure 5.9 Input referred output noise of the neural amplifier.

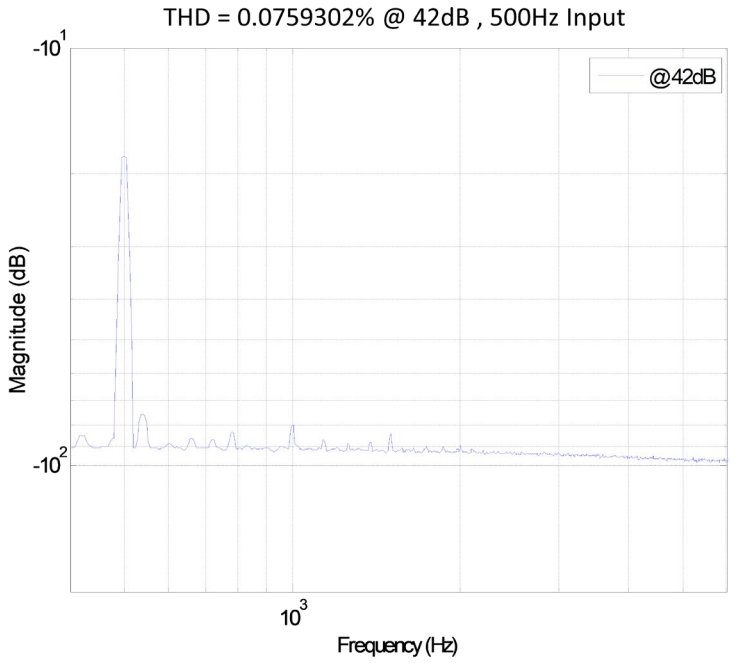

Gain 42dB	
S1	1
S2	0
S3	1
S4	0
S5	0
S6	0
V1	1.5V
V2	1.5V

Gain 60dB	
S1	0
S2	1
S3	1
S4	0
S5	0
S6	0
V1	1.5V
V2	1.5V

Figure 5.10 Total harmonic distortions at the output of the neural amplifier

The outputs of the 16 channels can be multiplexed using the built-in multiplexer (MUX). The four channel-select pins take digital inputs and connect the MUX output to the channels according to the digital signal. Figure 5.11 demonstrates four channel multiplexing. Four input signals having different frequencies are fed into four channels and the output signal is a time division multiplexed signal. The time required for the output to be stabilized from one channel to another channel is 3.5 µs. For an analog to digital converter (ADC) requiring 1.5 µs 'sample and hold' acquisition time, the sampling frequency would be 200 kHz or 12.5 kHz/channel.

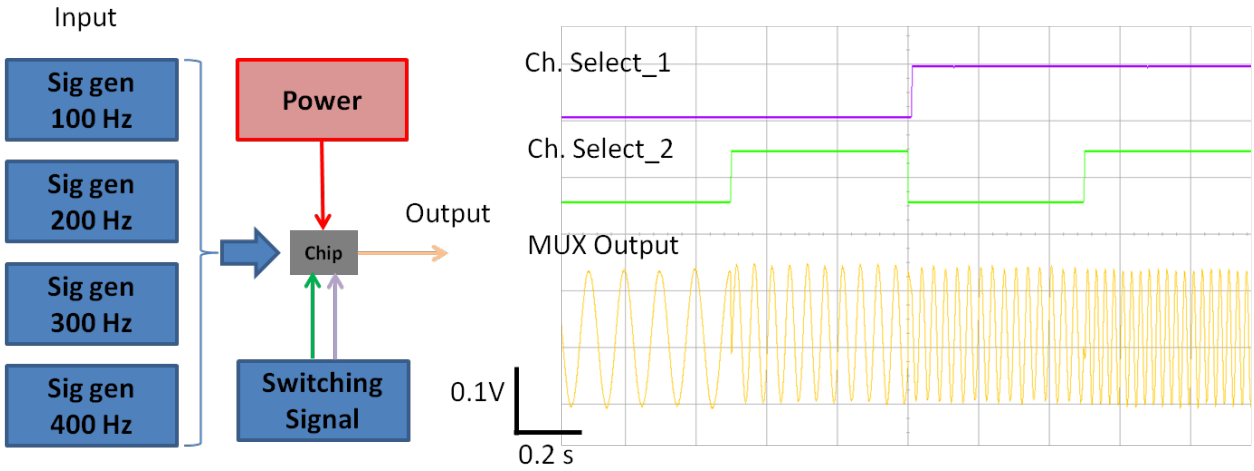

Figure 5.11 Four channels multiplexing.

5.4 Amplifier Board Design

After characterizing the neural amplifier IC, I have made a printed circuit board (PCB), as shown in Figure 5.12, to program the chip and use the chip to collect neural signal. A microcontroller (NRF52832) is used to program the IC. The board contains all other necessary active and passive electronic components for operation. The schematic of the circuit diagram and the layout of the PCB are given in Figure A.3 and A.4 in Appendix. The amplifier board has been used to record most of the neural data in my PhD study. This board is attached to the movable Vernier scale of the inserter. To protect the wire bonding, epoxy has been used to make globe top encapsulation of the chip (see Figure A.5 in Appendix). Neural signal from the electrode reaches the amplifier through the electrode holder and slip-ring. The ability to record neural activity during insertion is a useful feature of the developed inserter.

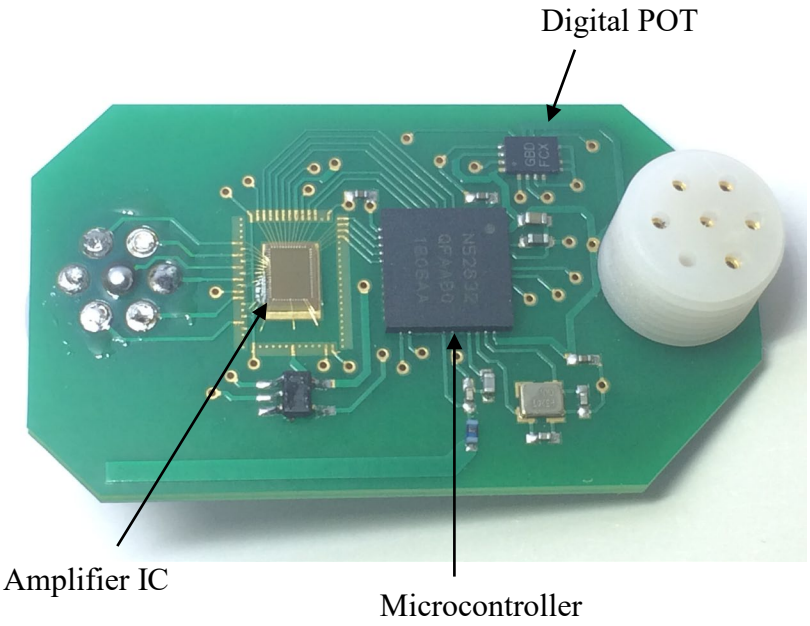

Figure 5.12 Neural amplifier PCB for recording neural spikes.

6. IN VIVO IMPLANTAION AND CHRONIC SINGLE UNIT RECORDING FROM RESPIRATORY NEURONS OF RAT

6.1 Evaluation of Rotational Speed of Electrode on Insertion

To evaluate different rotational and insertion speeds, electrodes were inserted at 1, 2 and 3 revolution per second (RPS) rotational speeds and at 100, 200 and 400µm/s insertion speeds in two rat brains. Each combination of rotational and insertion speeds was evaluated by 6 trials and the number of failures is given in Table 6.1. The 1 RPS rotational speed has 1, 2 and 5 failures and the 2 RPS rotational speed has 0, 0 and 2 failures when inserted at 100, 200 and 400µm/s, respectively. The 3 RPS rotational speed has 0 failure at all three insertion speeds. These results show that higher rotational speed allows faster insertion without failure. However, slow insertion allows blood vessels and brain tissue to accommodate the electrode [72] and, therefore, it is preferable. Thus, electrodes were inserted at 200µm/s in all the experiments. Since 2 RPS rotational speed showed 0 failure at 200 um/s, electrodes were inserted at 2 RPS. Slower rotational speed might result in insertion failure. Faster rotation likely would also allow insertion, but given I had found a successful combination of speeds of rotation and advance; I did not explore a wider range of values.

Table 6.1 Number of insertion failure for various rotational speed and insertion speed of microelectrode

Insertion Speed (µm/s)	Rotational Speed (RPS)		
	1	2	3
100	1	0	0
200	2	0	0
400	5	2	0

6.2 Microelectrode Implantation: In vivo Experiments

Microelectrodes were inserted in a number of non-survival and survival experiments under anesthesia. All surgical and animal handling procedures were performed in accordance with the regulations of the Institutional Animal Care and Use Committee (IACUC) and approved by the Purdue University Animal Care and Use Committee (PACUC). Female Long Evans rats (250-274 gm) were anesthetized with Isoflurane (5% for induction and 0.5 - 3% for maintenance, both in 2 L/min O_2). The rat was mounted on a stereotaxic frame using ear bars and a nose cone. Butorphanol (0.5-2 mg/kg, subcutaneous (SC)) analgesic was injected. The surgical site was shaved and cleaned with 10% betadine and alcohol swabs. A mid-line incision was made on the skull. An ALM retractor was used to hold skin during surgery. The `Botzinger complex (BotC)' of the brainstem was selected as the target of insertion. The `BotC' is a group of neurons located in the rostral ventrolateral medulla and ventral respiratory column [73]. In rat, the `BotC' is situated at ~12.4 mm posterior to bregma, ~2.2 mm lateral to mid-line and about 10 mm deep in the brain with reference to bregma as shown in Figure 6.1 [74]. The complex spans only about 0.5 mm in the coronal plane. To avoid penetrating the sigmoid sinuses (large blood vessels), the electrode was inserted at an angle of 10˚ to mid-line. Therefore, a 2 mm craniotomy hole was made in the skull at 0.5 mm lateral to mid-line instead of 2.2 mm. The dura was left intact. The `BotC' consists of respiratory neurons which generate inspiratory and expiratory activities [75-77]. The relationship between the neural activity recorded from electrode during insertion and the breathing of the rat provides a physiological marker for the target structure.

Now the inserter was attached to the stereotaxic frame for electrode insertion. An electrode was attached to the holder and loaded in the inserter. The electrode was positioned at the end of the micro-ferrule. The ferrule end was positioned on the craniotomy. In preparation for insertion, the spinner motor was accelerated to a speed of 2 RPS. The spinning electrode was then advanced into the brain at a speed of 200 um/s. Both motions were turned off when the electrode went about 8 mm inside the brain. The electrode was then advanced in micro-steps without spinning until a suitable neuron was found. A 3-electrode recording system was used. The scalp retractor was used as the reference and an injection needle under the skin on the back was used as amplifier ground. Some photos of the electrode insertion experiment are shown in Figure 6.2.

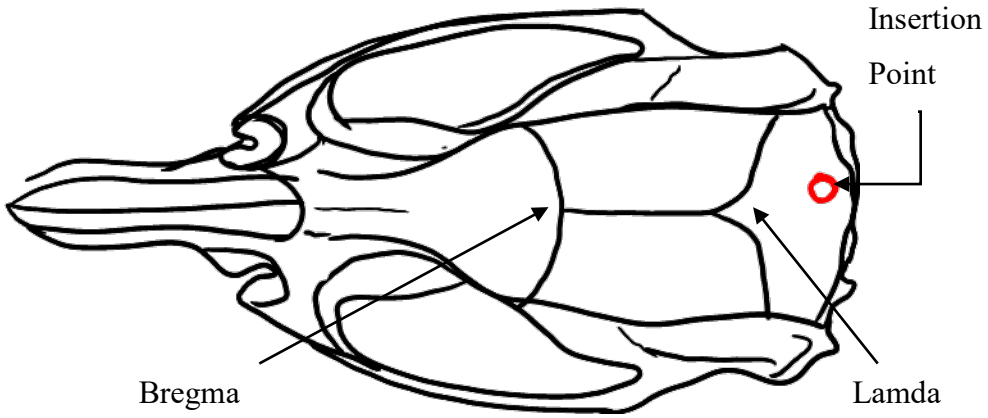

(a)

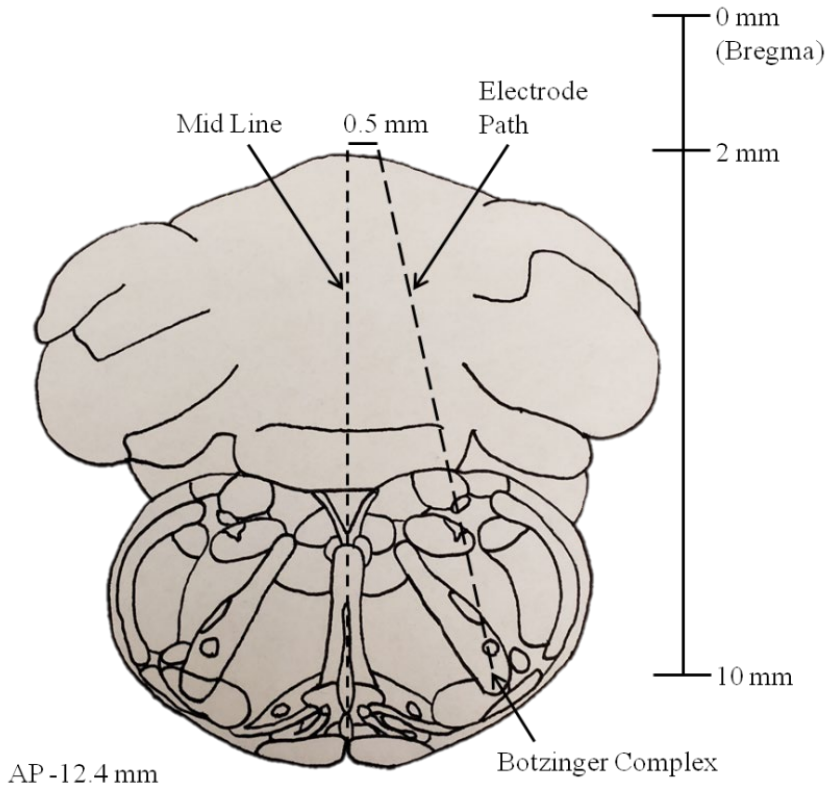

(b)

Figure 6.1 Location of the 'Botzinger' complex in rat brain. (a) A rat brain skull. The red dot on the skull posterior to lambda shows the insertion site. (b) A rat brain section at 12.4 mm behind bregma showing the location of the `BotC' and the electrode insertion path. The electrode is inserted at 10 degrees to avoid penetrating blood vessels. © [2019] IEEE Reprinted with permission from [57]

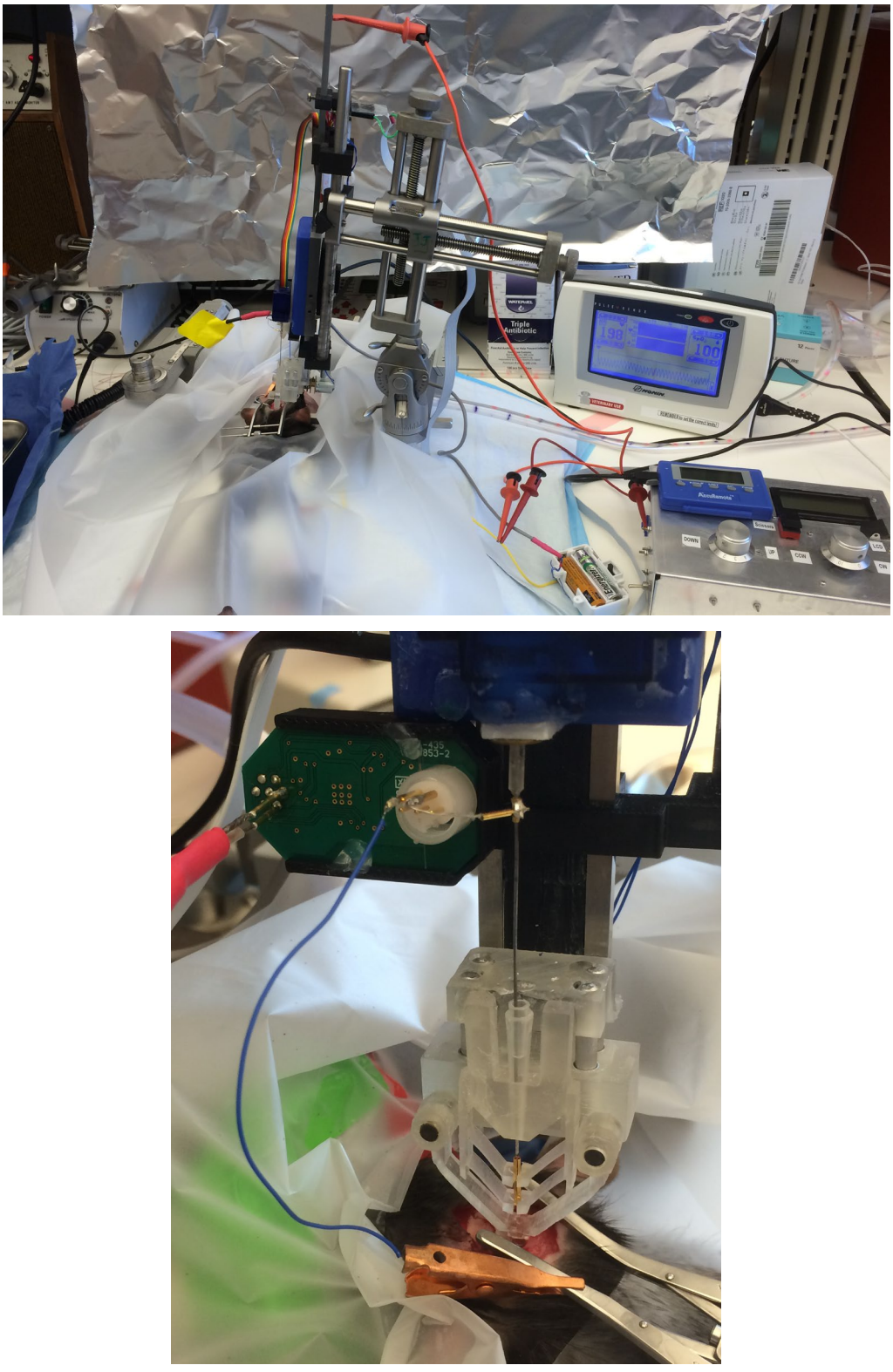

Figure 6.2 Two photos of the in vivo electrode insertion experiment.

In survival experiments, after reaching the target, the electrode was fixed on the skull as shown in Figure 6.3. First, the rigid arms of the guide were retracted and they opened up without dislocating the electrode. Silicone sealant and ultraviolet (UV) light cured dental cement were applied to fix the electrode to the skull. Then the electrode holder was retracted and detached from the electrode socket and the inserter was removed.

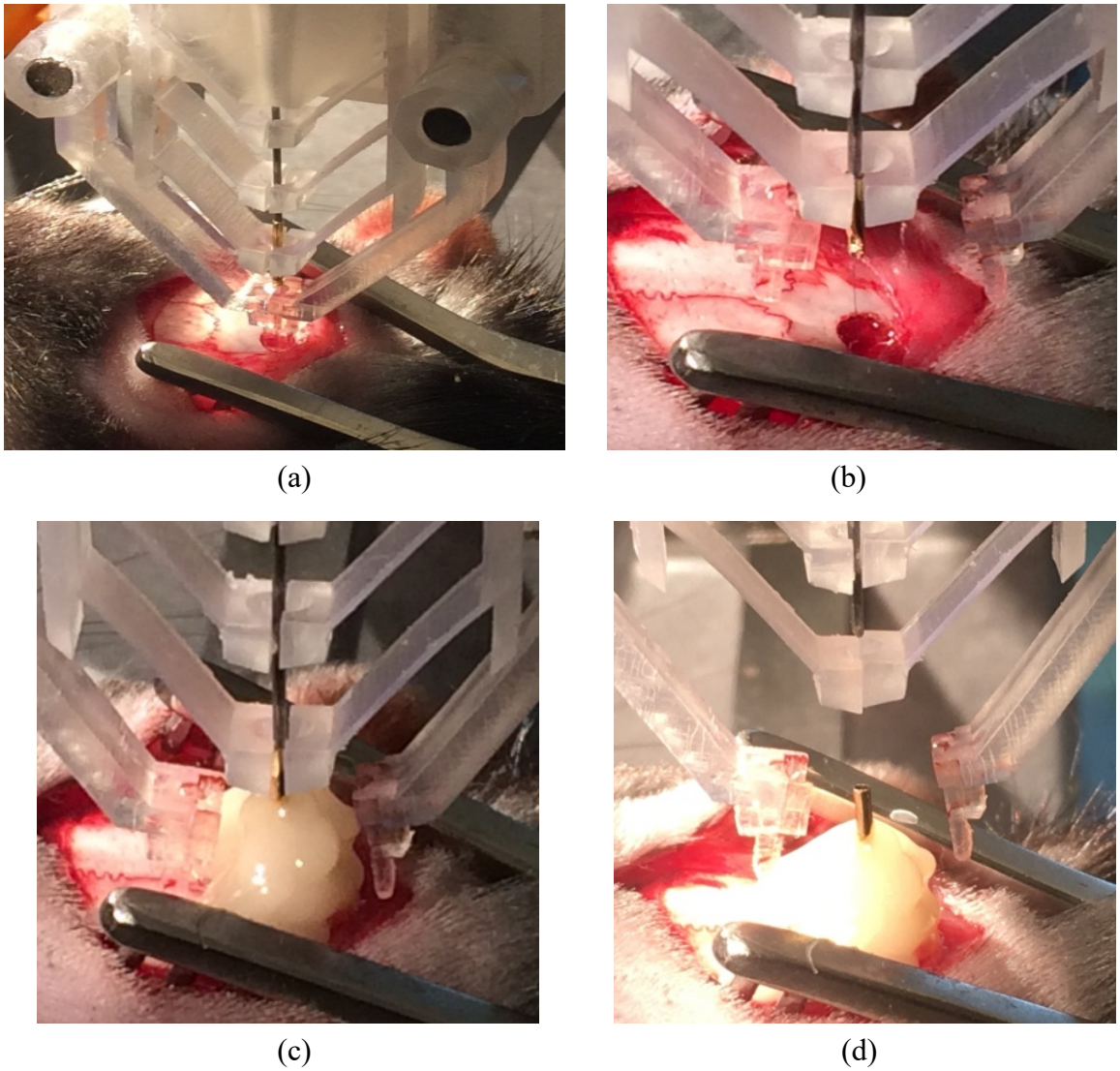

(a) (b)

(c) (d)

Figure 6.3 In-vivo demonstration of the electrode fixing process in a survival experiment. (a) Microelectrode inserted in the brainstem of a rat. (b) Opening of rigid arms after insertion. The part of electrode above the brain is visible. (c) Application of dental cement. (d) Holder detached from electrode socket. (e) Recording cable plugged into socket to verify neural activity. (f) Plastic pedestal mounted on skull to secure electrode.

Figure 6.3 (continued)

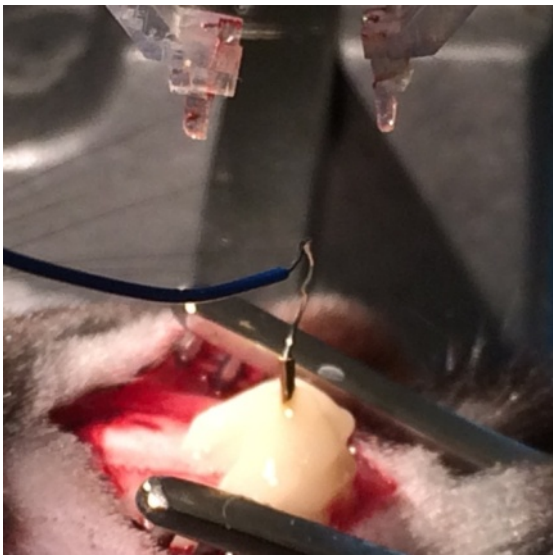

(e)

(f)

Two stainless steel screws were implanted and connected to a socket with a wire to make the reference electrode. Finally, a plastic pedestal with holes was mounted on the skull to secure the electrodes and the rat was recovered from anesthesia.

Recordings were made under light anesthesia various times after recovery from implantation surgery. Neural signal was obtained by connecting the amplifier to the electrodes with a cable. An injection needle under the skin on the back was used as amplifier ground. After recording, the needle was removed and the rat was recovered from anesthesia.

6.3 Acute and Chronic Neural Recordings

Figure 6.4 shows the neural activity recorded at progressive depths of insertion in a survival experiment (Rat1). Various neural activities were observed at different positions in the brain. A thermocouple was placed in front of the nose to sense respiration. For each breathing period, the thermocouple generated a voltage oscillation due to the temperature variations in the inhaled and exhaled air. This respiratory signal is also shown in Figure 6.4. The neural signal was played on a speaker and the rat's chest movements were observed. At 9.68 mm depth, neural firing was

found to be correlated with respiration. The microelectrode was stepped further into the brain and a stronger respiratory neural activity was observed at 9.83 mm. These observations demonstrated that the electrode reached the target region. Figure 6.4 shows the neural signal recorded at each phase of the electrode fixing process. The peri-event time histogram (PETH) of the detected spikes also shows the synchronization of the neural firing with respiration. Each PETH was obtained by averaging the spike rates from 20 respiratory cycles. The negative peak of each respiratory cycle was used to synchronize the spikes. Average cycle duration was used for segmenting the signal around the negative peaks.

Four survival experiments (Rat1-Rat4) were performed. Neural activity was recorded and observed up to 76 days in Rat2. In Rat1 and Rat4, neural activities were observed up to 54 and 63 days, respectively. The head cap of Rat3 fell off 5 days after implantation surgery and therefore the rat was euthanized. Figure 6.5 shows the neural signal recorded from Rat1 on day 1, 8, 21, 34 and 50. The spikes were sorted and the first 3 dominant units are shown along with their PETHs. The first dominant unit is synchronized with respiration but the second and third units are not correlated with respiration. The neural signals recorded from Rat2 and Rat4 are given in Figure 6.6 and Figure A.6 (in Appendix), respectively. The rats were euthanized by injecting 0.9ml euthanasia into the peritoneum (intraperitoneal (IP) injection) after 90 days of post implantation.

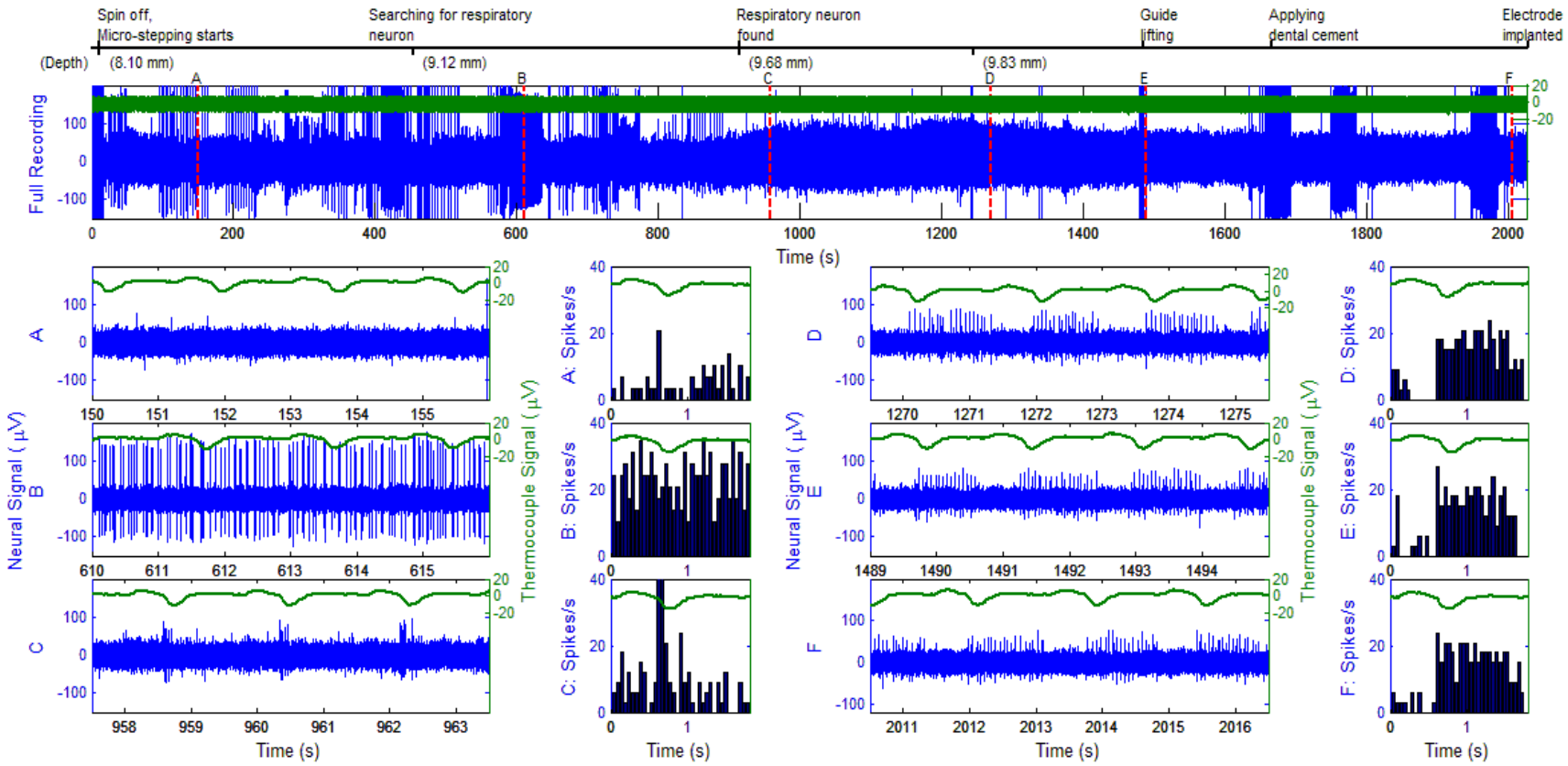

Figure 6.4 Neural recordings at various steps of electrode insertion. Blue trace is neural signal and green trace is respiration signal. Each negative peak in the respiration signal represents an exhalation. Top plot: Full recording from micro-stepping to electrode implantation. The line at top shows time stamps and associated electrode depth at various events during insertion process. Plot A-F in the first and third columns show segments of the full recording at instances marked with red dash line on the full recording and the corresponding PETHs of neural firing in a breathing cycle are shown in the second and fourth columns. Plot A: Recording at 8.40 mm depth during micro-stepping. Few small spikes are observed. Plot B: Recording at 9.32 mm depth. Many large spikes, although not related to respiration, are observed. Plot C: Appearance of respiratory neural activity. Neural firing synchronized with respiration is observed at 9.68 mm depth. Plot D: Stronger respiratory neural activity observed at 9.83 mm depth. Plot E: Neural signal after opening the rigid arms. Plot F: Neural signal after applying dental cement. © [2019] IEEE Reprinted with permission from [57]

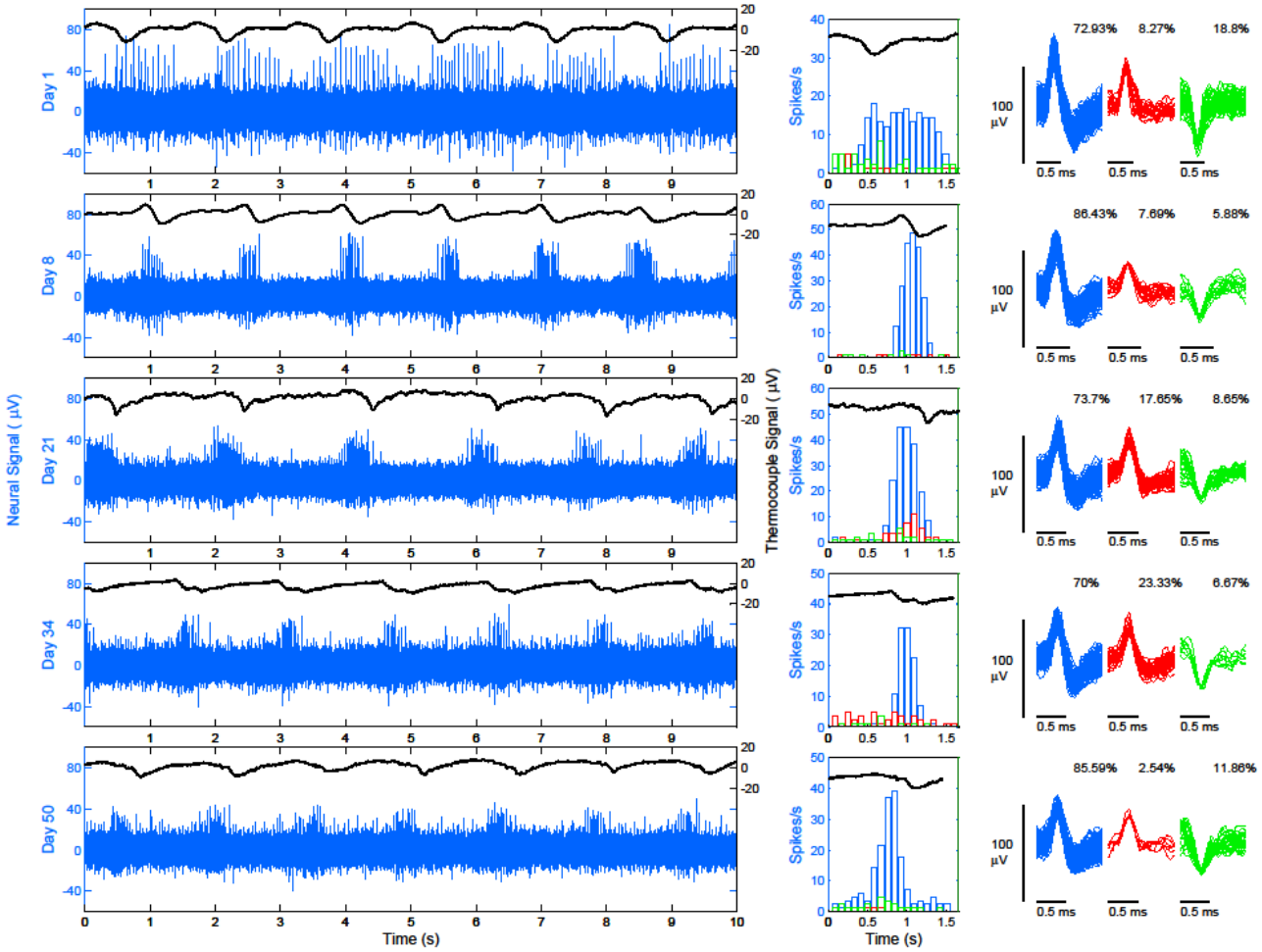

Figure 6.5 Long-term neural recording from the Botzinger Complex of Rat1. (Left) Segments of respiratory neural signal recorded on day 1, 8, 21, 34 and 50. Blue trace is the neural signal and black trace is the respiration signal. (Right) The 3 largest populated spike groups after spike sorting. The percentage number of spikes in each group are given. (Middle) The PETH of the three dominant spikes in a breathing cycle. © [2019] IEEE Reprinted with permission from [57]

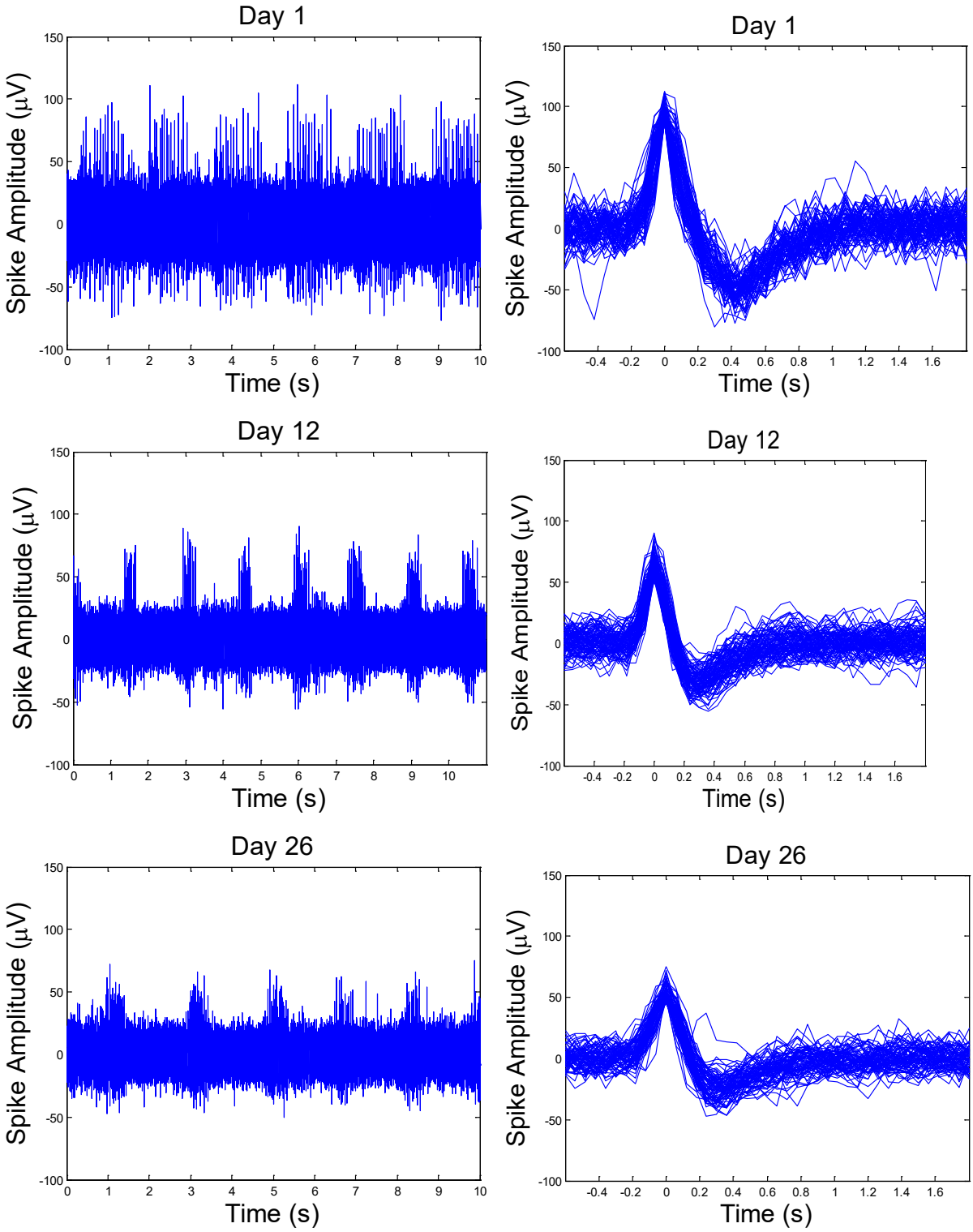

Figure 6.6 Long-term respiratory neural recording from Rat2. Left plots show segments of recording on Day 1, 12, 26, 35, 48, 61, 76. Right plots show the spikes after spike sorting.

Figure 6.6 (continued)

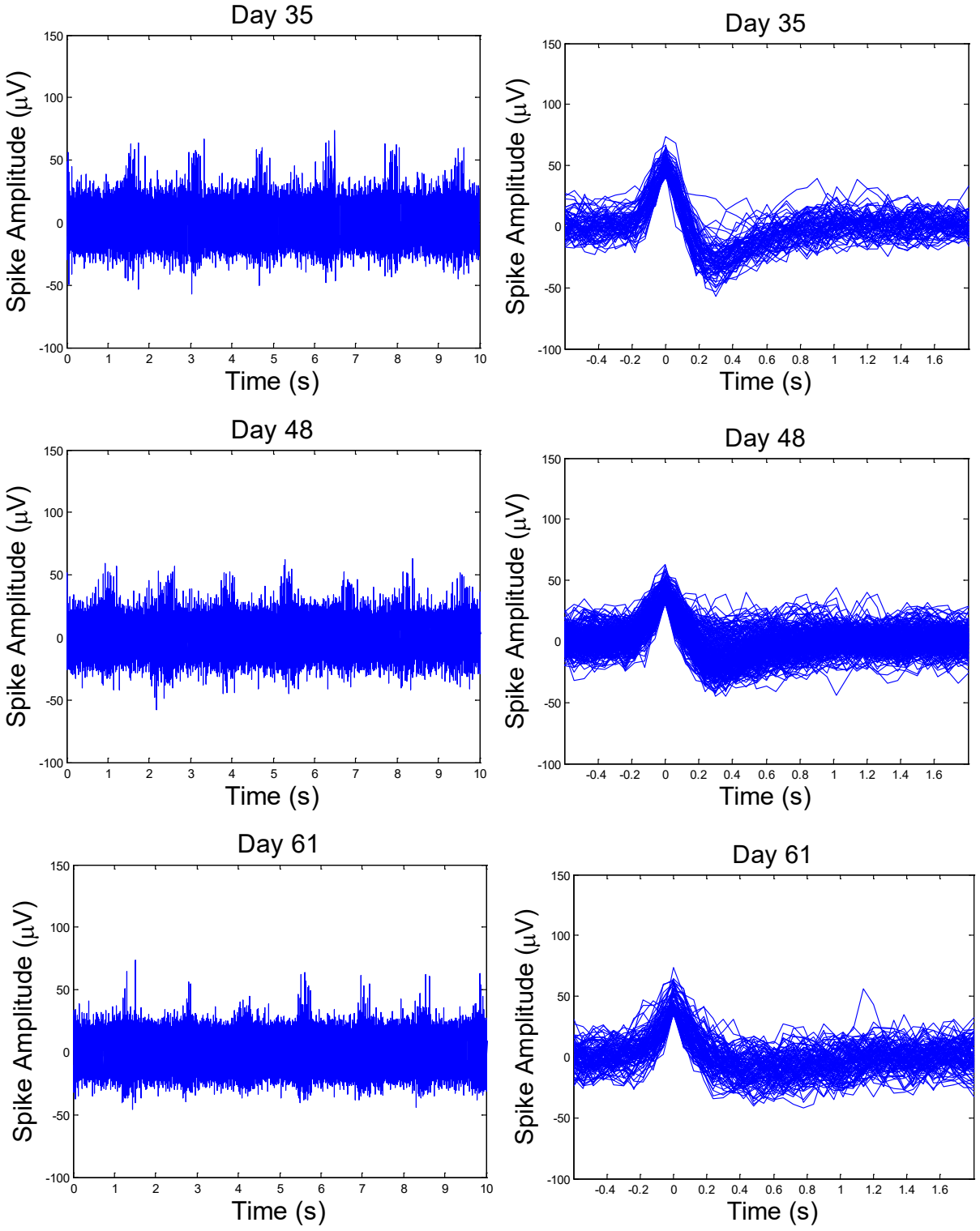

Figure 6.6 (continued)

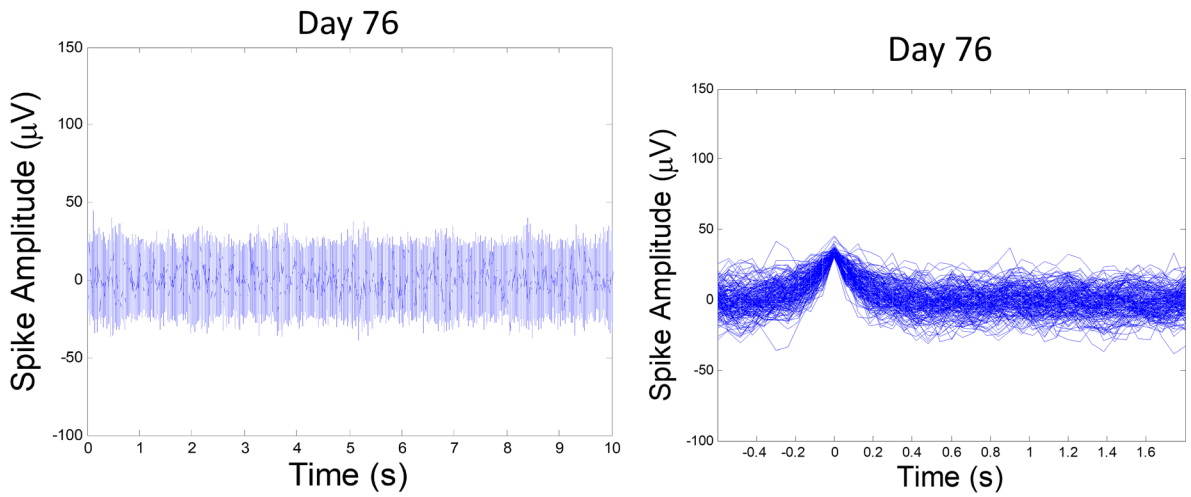

The decay of the neural signal amplitude with time has been observed. The noise amplitude remained almost the same. The SNR of the recorded signals in different days are shown in Table 6.2. The SNR is calculated using the following formula:

$$SNR = 20log\frac{s}{n} \tag{6.1}$$

where, *s* is the average spike amplitude and *n* is the average noise amplitude.

Table 6.2 Signal-to-noise ratio of the recorded neural spikes

Day	**SNR**
1	7.36
12	8.30
26	6.02
35	6.03
48	5.58
61	5.11
76	2.92

The respiratory neural spikes were observed in more than 30 acute experiments. In couple acute experiments, I did not observe spikes synchronized with respiration. I believe that I missed the small target structure due to the variability of brain structure between rats. The neural recordings from 3 acute experiments are shown in Figure 6.7.

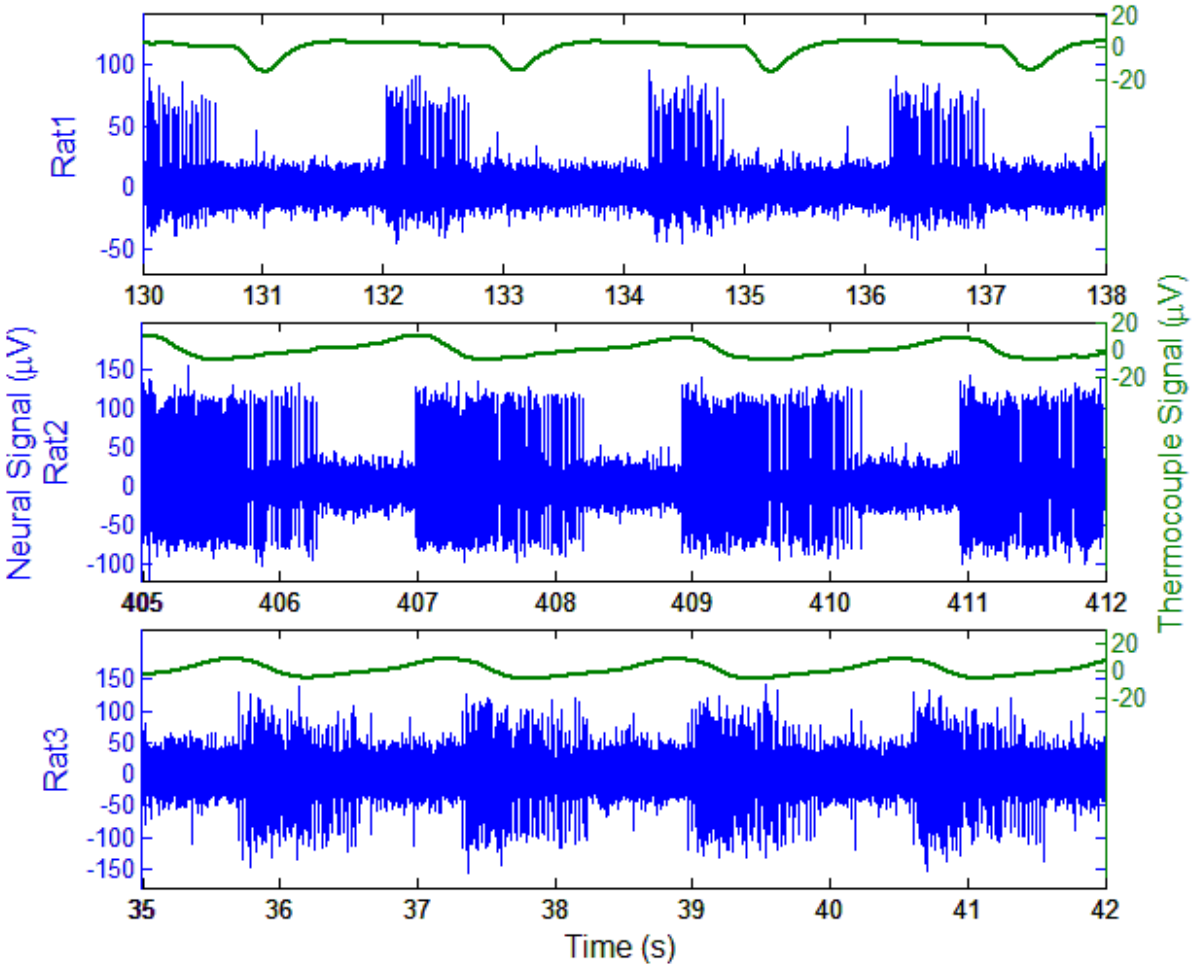

Figure 6.7 Respiratory neural activity recorded from 3 non-survival experiments. © [2019] IEEE Reprinted with permission from [57]

6.4 Electrode Track

To visualize the implanted microelectrode inside the brain, a CT image of the microelectrode was obtained after perfusion (Figure 6.8) [78]. The microelectrode shows no sign of buckling inside the brain. The reconstruction parameters were selected such that brain tissue does not appear after reconstruction.

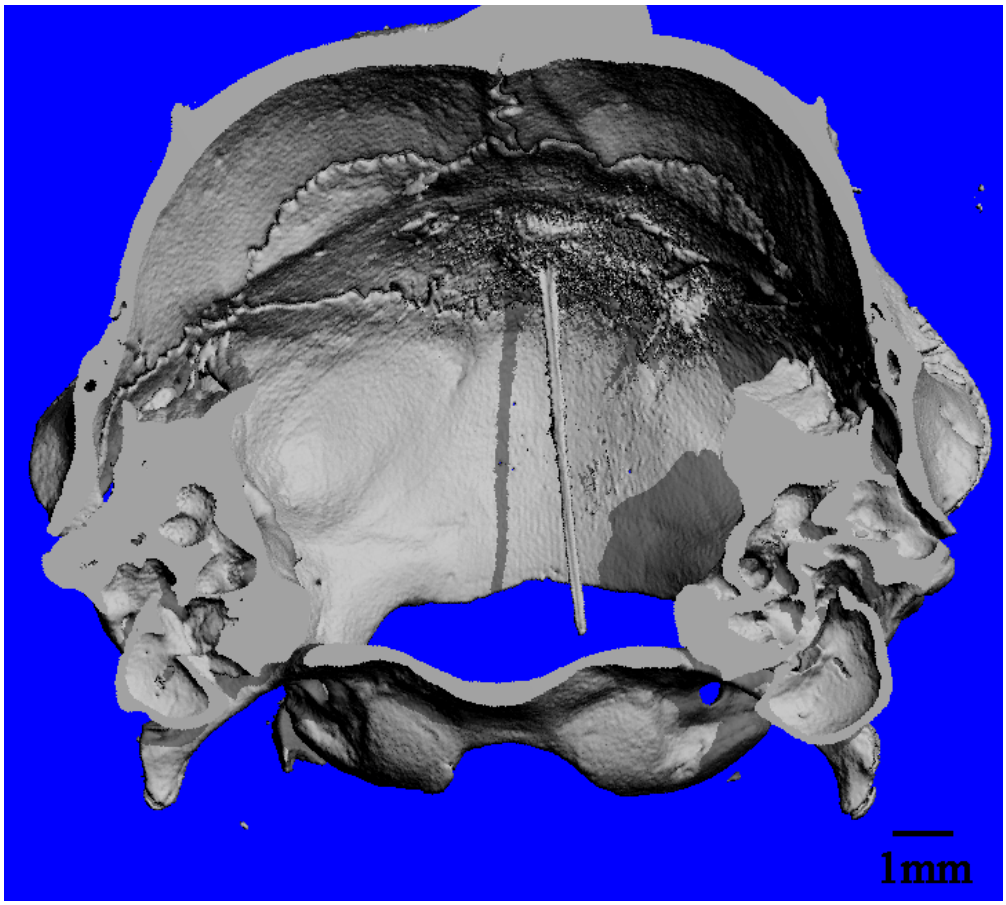

Figure 6.8 The X-ray 3D image of the microelectrode in rat brain. The 25 µm electrode appears thicker than its actual diameter because of artifacts. © [2019] IEEE Reprinted with permission from [57]

The 25 µm electrode appears thicker than its actual diameter because of artifacts. Coating the neural electrode with fluorescent dye (DiI1) was not able to provide a complete electrode track [79] in brain section because the dye was washed away from the tip due to spinning motion (Figure 6.9). Nissl staining was also done on brain slices after perfusion to obtain the electrode track in the tissue. Since the electrode is very thin, it is very difficult to find the mark without lesioning the tissue. Therefore, a small current (10µA) was injected in the brain through the microelectrode for 10s. After lesioning, the mark of the electrode tip was visible (Figure 6.10). Comparing Figure 6.1(b) and 6.10, it is seen that the electrode tip is at the right location of the brain. This also proves that the electrode reached the target.

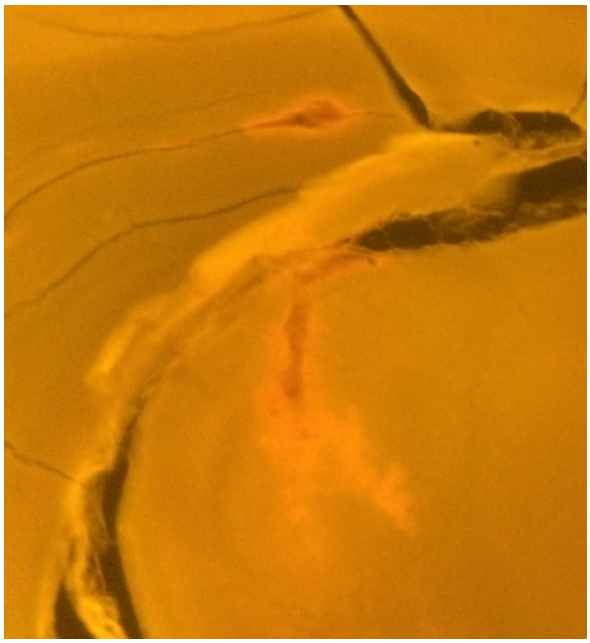

Figure 6.9 Fluorescent dye disappeared from the electrode tip because of the spin motion and spread at the top part of the brain.

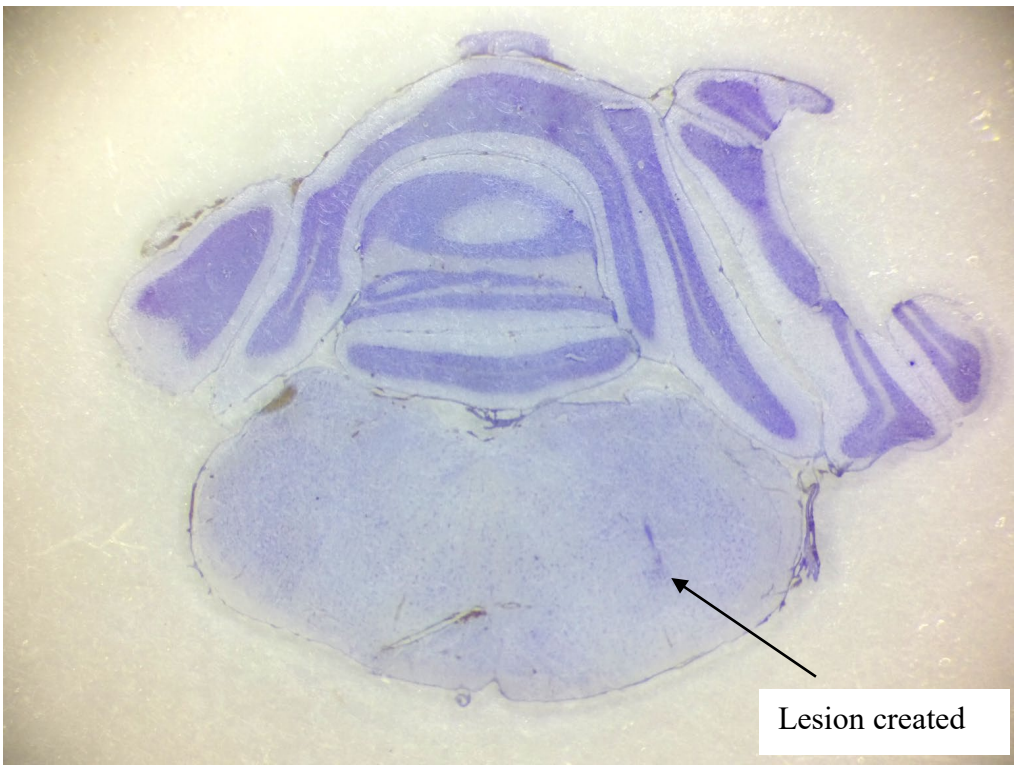

Figure 6.10 Brain section after Nissl staining. Lesion created by the electrode tip after passing current was observed.

6.5 Micromotion Compensation

Figure 6.11 shows the micromotion compensation of the microelectrode with helical spring. Microelectrodes were inserted in the CA1 region of rat brain and the micro-force was measured with the S256 sensor. Before dissolving sucrose (Figure 6.11(a)), two types of oscillations were observed in the force due to motions of the brain caused by two sources. The slower oscillation is due to the respiration of the rat and the faster oscillation is due to the heart beating. Due to these two micromotions of the brain, the electrode attached with the sensor experiences push and pull forces continuously which is harmful for long term recordings. After dissolving sucrose (Figure 6.11(b)), both the oscillations are significantly reduced. The microelectrode becomes more flexible after dissolving sucrose and therefore dampens the micromotions.

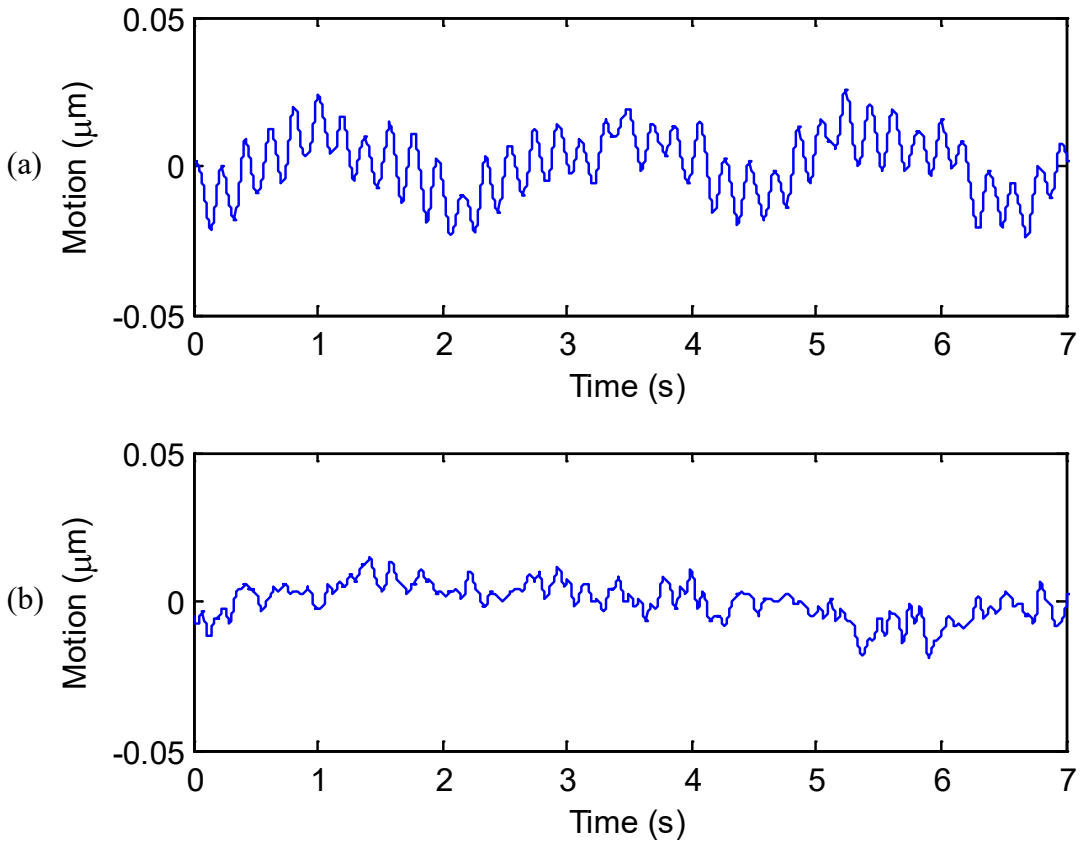

Figure 6.11 Micromotion compensation of the electrode with helical spring. (a) Before dissolving sucrose. (b) After dissolving sucrose.

6.6 Neural Recording Using Wireless Implantable Device- Bionode

A wireless implantable device, called Bionode, has been developed at the Center for Implantable Devices (CID) (Figure 6.12). It consists of an analog amplifier board, a mother board and a power board. The amplifier board contains the neural amplifier. The mother board contains NRF52832 microcontroller and necessary circuits for wireless data transmission. The power board contains power management circuits, a battery and two power receiving coils. After all the boards are assembled, the device is packaged in a sealed container and sterilized for implantation. The Bionode receives power wirelessly from an external source which can be a coil or a cavity resonator. The device has wireless power transfer (WPT) capability to charge a built in battery which supplies the power necessary for the device operation. The signal frequency used for power transmission is 345 MHz. The Bionode transmits the data through Wi-Fi to an external raspberry pi at 2.4 GHz. The external raspberry pi then sends the data to computer through Wi-Fi. The data sampling rate of the Bionode was set to 10KHz per channel.

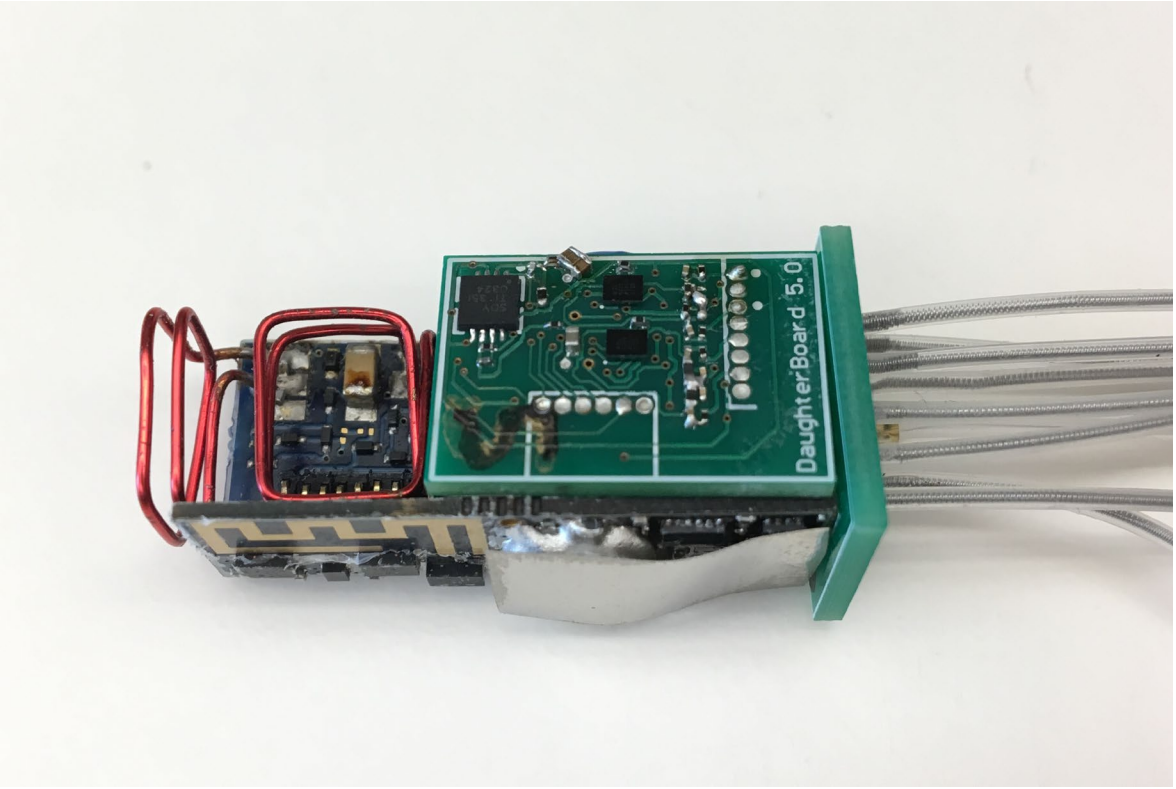

Figure 6.12 The Bionode – a wireless implantable device for bio-potential recording and stimulation. The picture shows the interior of the device.

The Bionode was implanted in rat to obtain neural recording from freely moving rat. The device was implanted in one side of the rat. The rat was under isoflurane anesthesia during the whole implantation procedure. Thermocouple couple was implanted in the nasal cavity to obtain respiratory signal. Microelectrode was implanted in the brainstem to obtain neural activity. To record ECG signal, ECG leads were also implanted. The device implantation was done by my colleague Ethan Biggs. All surgical and animal handling procedures were performed in accordance with the regulations of the Institutional Animal Care and Use Committee (IACUC) and approved by the Purdue University Animal Care and Use Committee (PACUC). After implantation, the rat was recovered from anesthesia and put in a cage. Figure 6.13 shows a segment of the respiratory neural signal recorded in Dataview (a GUI for data recording) while the rat was awake after device implantation. The thermocouple signal was not obvious. Possible reason could be the sensor in contact with tissue. The ECG electrodes also pick up the EMG signal of the diaphragm muscle. Therefore, diaphragm EMG signal was derived from the ECG signal which is shown in Figure 6.14. The respiratory neural activity was synchronized with diaphragm contraction and expansion. Sometimes the rat sniffed when it was awake. Figure 6.15 shows a segment of the respiratory neural activity while the rat was sniffing. During sniffing, the rat breathes at much higher frequency.

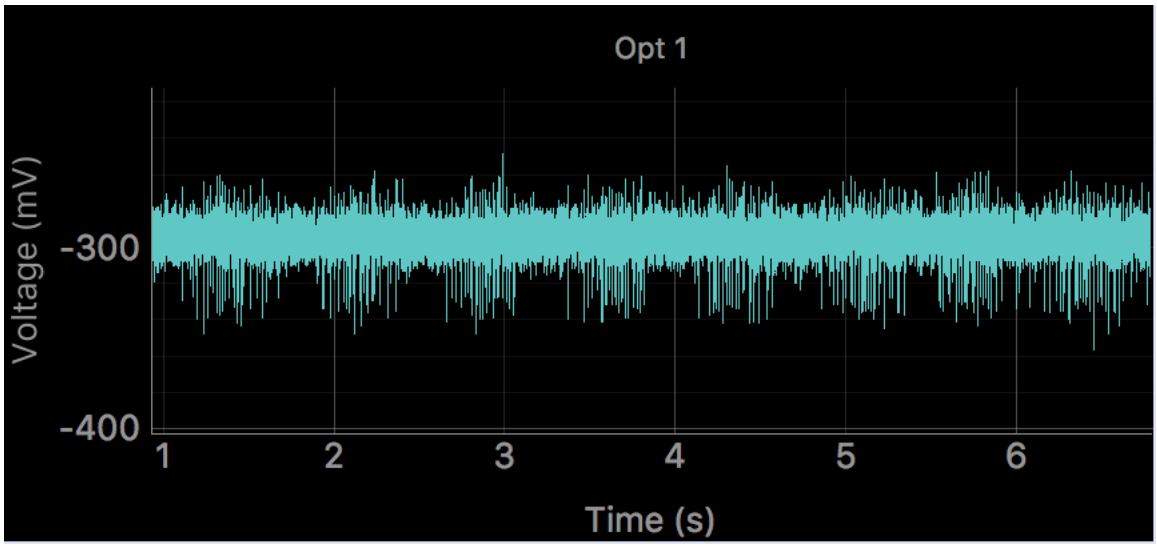

Figure 6.13 Respiratory neuron single unit activity recorded from a freely moving rat using the microelectrode and Bionode (Screen shot from Dataview).

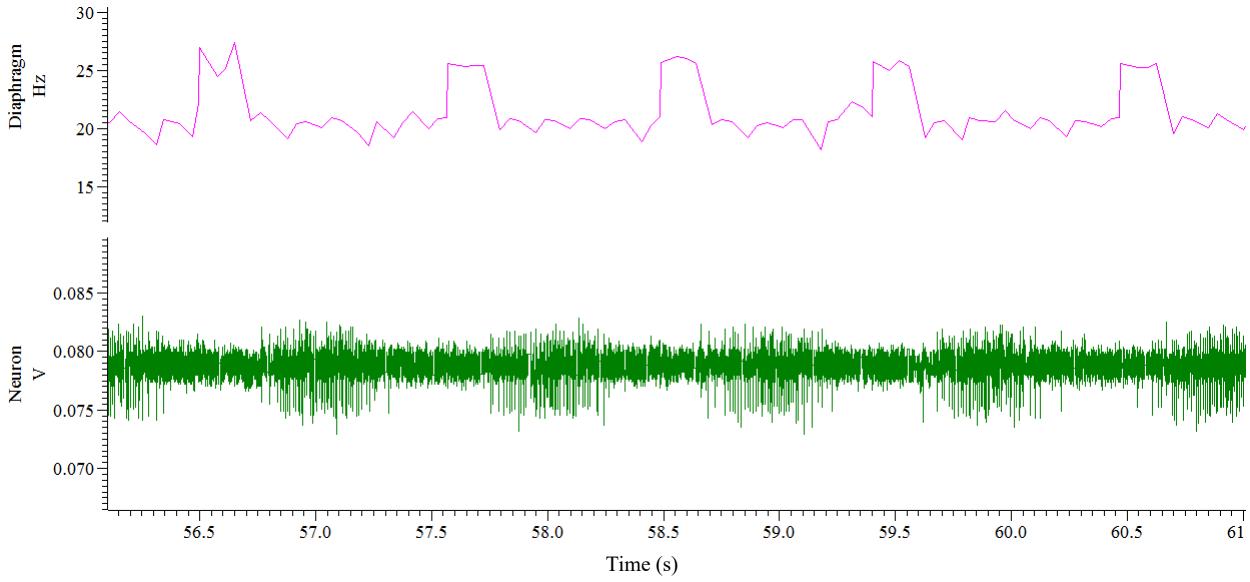

Figure 6.14 Single unit respiratory neural activity was synchronized with diaphragm EMG signal in a freely moving rat. The signal was recorded using Bionode.

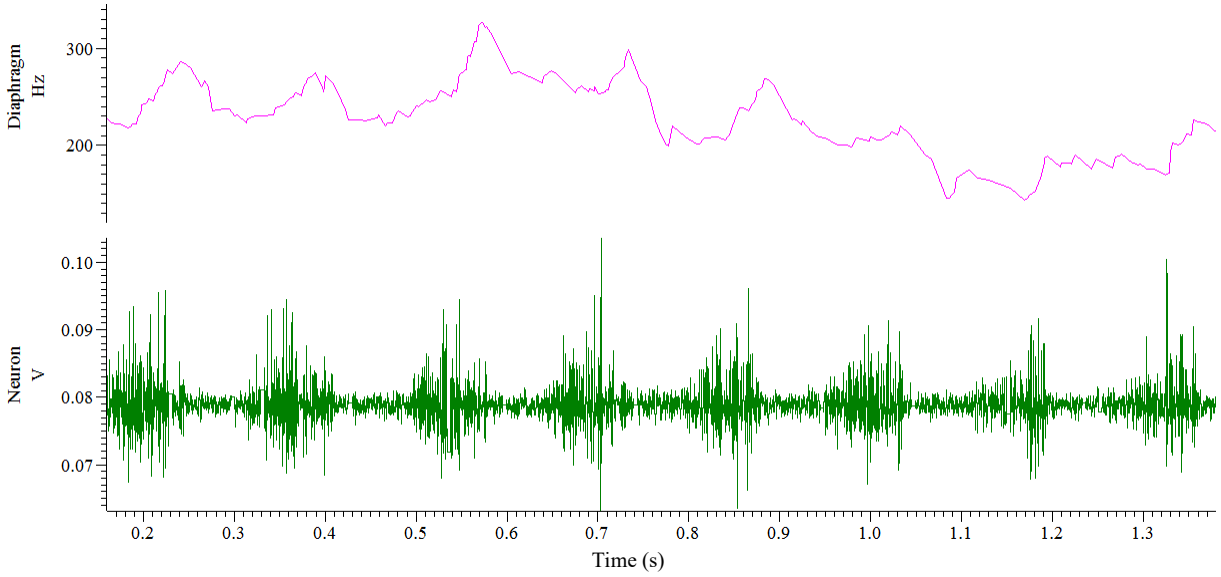

Figure 6.15 A segment of the respiratory neural activity while the rat was sniffing. During sniffing, the rat breathes at much higher frequency.

6.7 Respiratory Neural Activity during Seizures in Freely Moving Rat

To investigate the brainstem neuronal activity during seizures in freely moving rat, microelectrode along with the wireless data transmission device (Bionode) was implanted in a rat and epileptic seizure was induced by injecting Tetanus Neurotoxin (TeNT) in the hippocampus of the rat brain. Isoflurane anaesthetized rat was implanted with nasal thermocouple and micro-wire electrode in the Botzinger complex. Again the device implantation was done by my colleague, Ethan Biggs. All surgical and animal handling procedures were performed in accordance with the regulations of the Institutional Animal Care and Use Committee (IACUC) and approved by the Purdue University Animal Care and Use Committee (PACUC). After device implantation the rat was recovered from anesthesia and it was put in the recording cage on the 4th day post surgery. The rat developed epileptic seizure on the 5^{th} day. From then it was observed to seize very often with sudden intense erratic motion. Figure 6.16(a) shows a portion of the recorded data in a seizing period. The blue plot on top shows the thermocouple signal and the green bottom plot shows the neural activity in brainstem. Neural activity synchronized with respiration was observed at the beginning 0-10s (Figure 6.16(b)). After 10^{th} second the neural activity started to lose synchronization and no neural firing was observed after 15^{th} second although nasal airflow was present (Figure 6.16(c)). The rate of respiration was not constant in 0-35s period. At about 37^{th} second the rat started seizing with intense motion and it collided with the cage walls multiple times. Due to the intense motion, motion artifact was observed in the signal (Figure 6.16(d)). The motion sustained for about 2 seconds. After the erratic motion, no airflow was observed for about 5 seconds which indicates the rat was having transient apnea. In this 5 second period (39-44s), random neural spiking was observed. After 44^{th} second, breathing re-started and unit firing returned to the rate time-locked to the nasal signal (Figure 6.16(e)). Another epoch of epileptic seizure and transient apnea is shown in Figure 6.17.

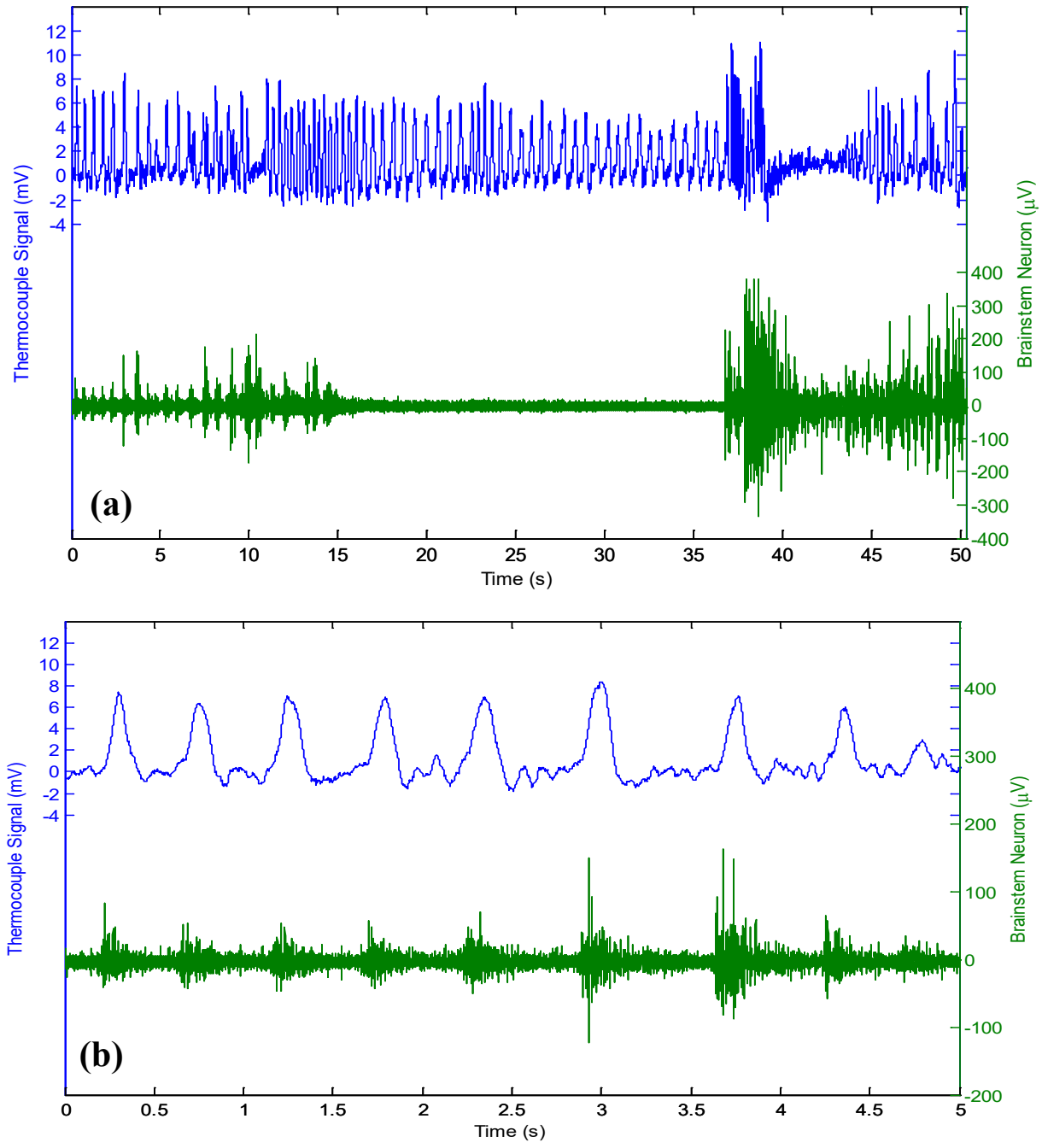

Figure 6.16 Respiratory neuronal activity during seizures in freely moving rat. The blue plot on top shows the thermocouple signal and the green bottom plot shows the neural activity in brainstem. Plot (a) shows the full recorded data in a seizing period and plot (b)-(e) shows segments of data at various moments of the seizing period. (b) Typical neural activity synchronized with respiration. (c) Neural activity lost synchronization and no neural firing was observed although nasal airflow was present. (d) Beginning of seizure with intense motion. Motion artifact was observed in 37-39s period in the signal. No airflow and random neural spiking were observed in 39-44s period. (e) After 44th second, breathing re-started and unit firing returned to the rate time-locked to the nasal signal.

Figure 6.16 (continued)

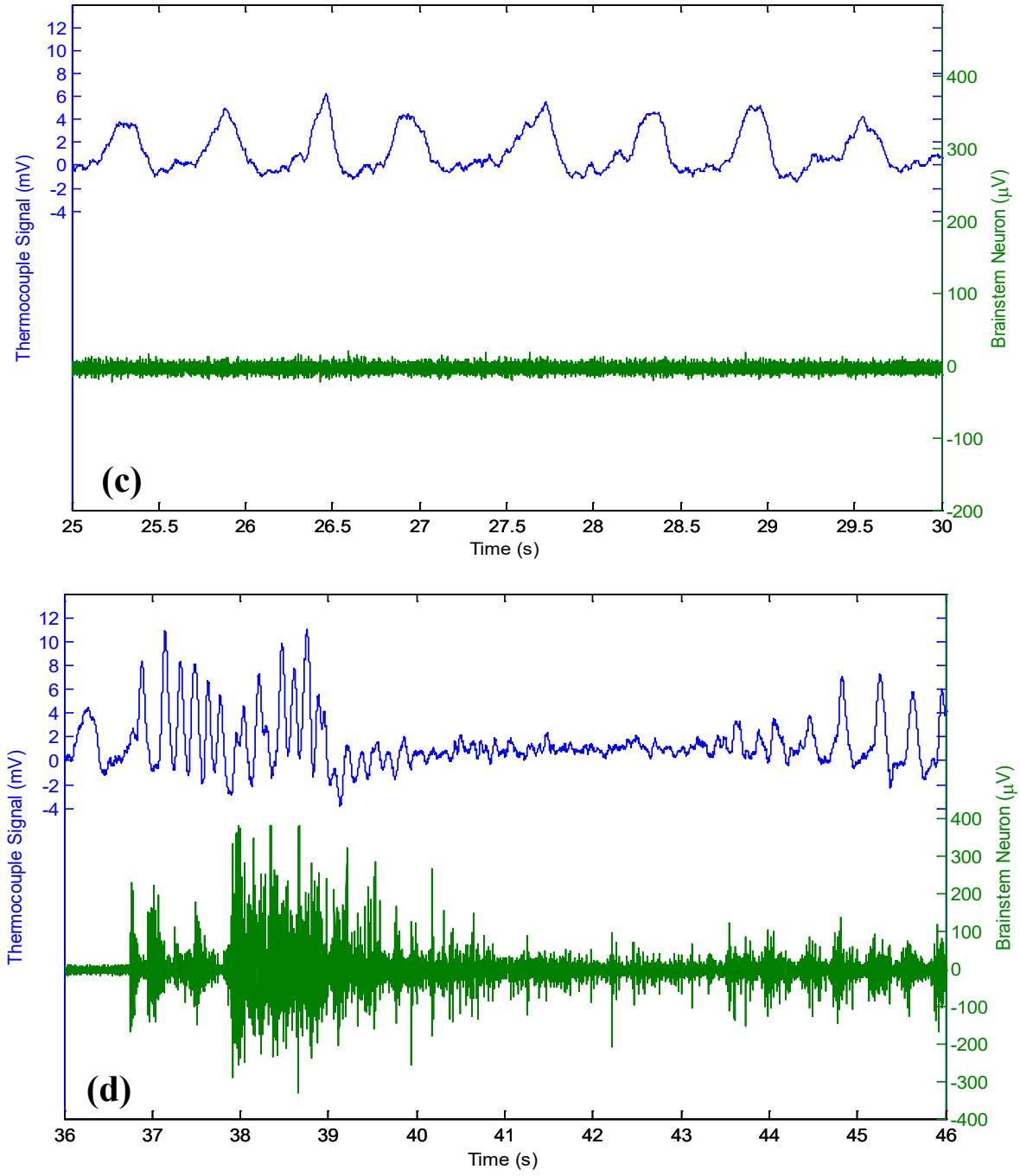

Figure 6.16 (Continued)

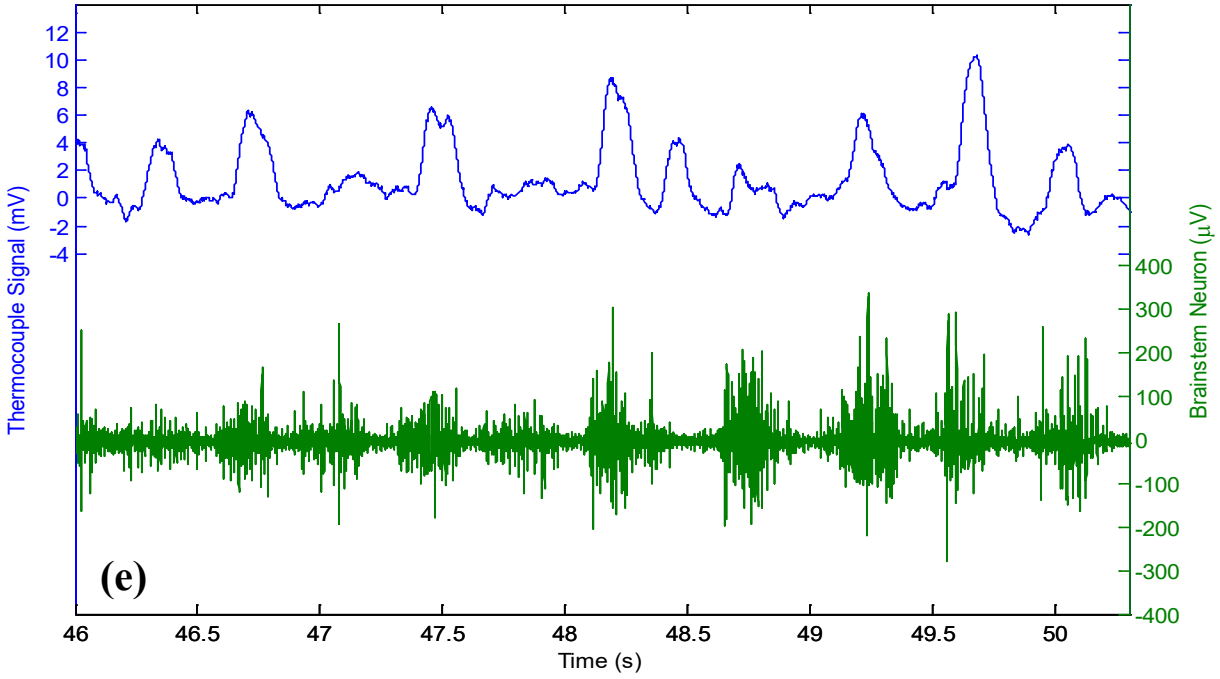

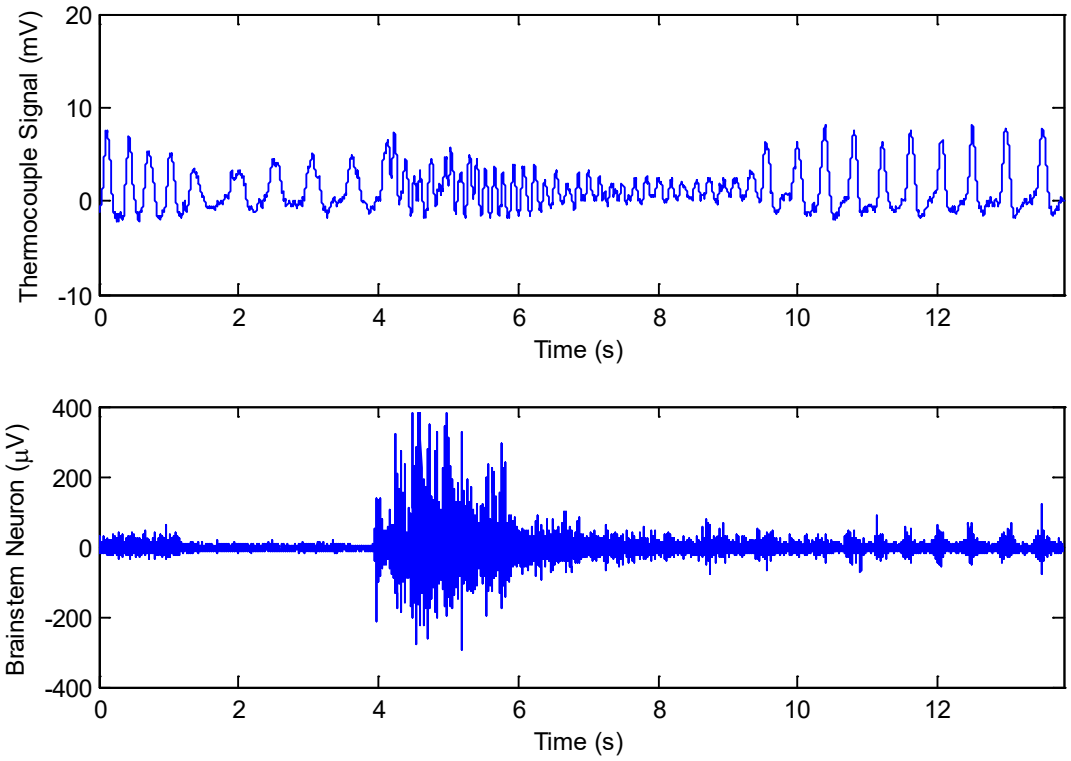

Figure 6.17 Another epoch of epileptic seizure and transient apnea.

6.8 Respiratory Neural Activity during Seizures in Anesthetized Rat

To investigate the brainstem neuronal activity during seizures in anesthetized rat induced by intrahippocampal kainic acid (KA), micro-wire electrodes were inserted in the Botzinger complex of rat [80]. These experiments were led by Professor John Jefferys from University of Oxford, Oxford, UK and Professor Thelma Lovick from Bristol University, Bristol, UK. Urethane-anaesthetized female Long-Evans rats were implanted with: nasal thermocouple, venous and arterial cannula, and electrodes for ECG, hippocampal, cortical, and brainstem recording micro-wire electrodes. The surgeries were done by Professor John Jefferys and Professor Thelma Lovick. I inserted my microelectrodes in the brainstem using my developed inserter and used my neural amplifier to obtain the neural signal. The phasic respiratory-related units from the Botzinger region was recorded during 61 apneas in 8 rats [80]. When nasal airflow ceases, the units continue to fire rhythmically but at a significantly lower frequency. Once breathing re-starts, unit firing returns abruptly to the rate time-locked to the nasal signal (Figure 6.18). Twenty-two rats die spontaneously after injecting KA. In 11/12 rats recording of Botzinger neuronal activity continues through the final apnea. After nasal airflow ceases, respiratory effort (from brainstem activity, EMG and/or visual observation) continues for ≤43s before blood pressure (BP) and heart rate (HR) begin a sharp terminal decline (Figure 6.19(a)). Active inspiratory efforts in the absence of nasal airflow suggest that the cause of death is obstructive apnea. The remaining 10 lethal apneas are not obstructive because the respiratory drive stops at the last breath which suggests a central mechanism (Figure 6.19 (b)) [80].

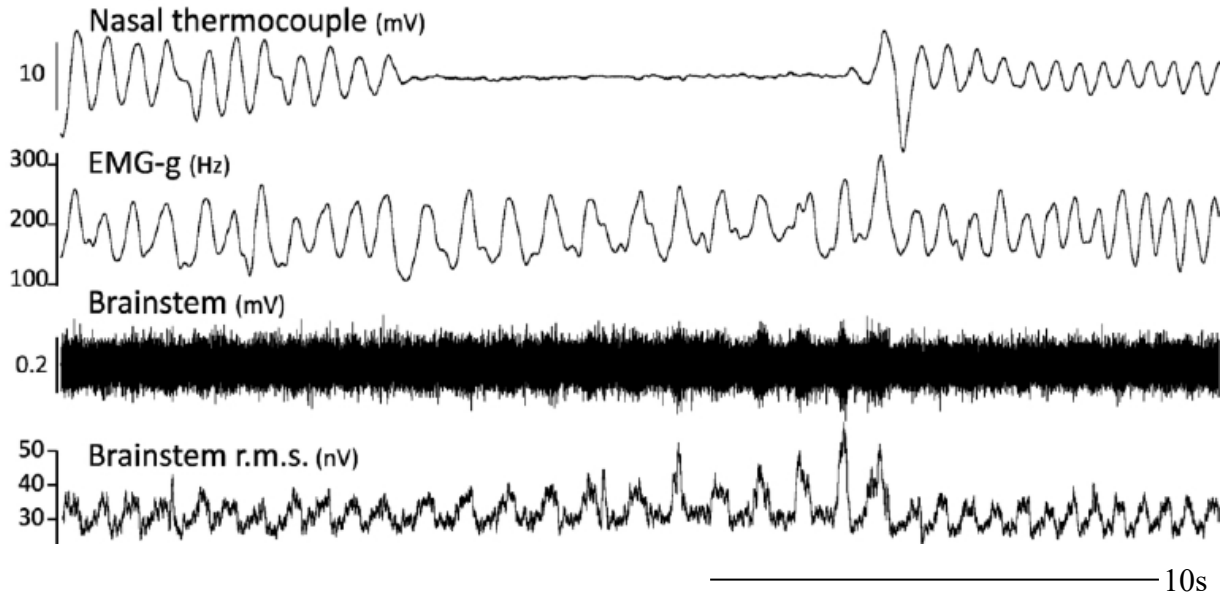

(a)

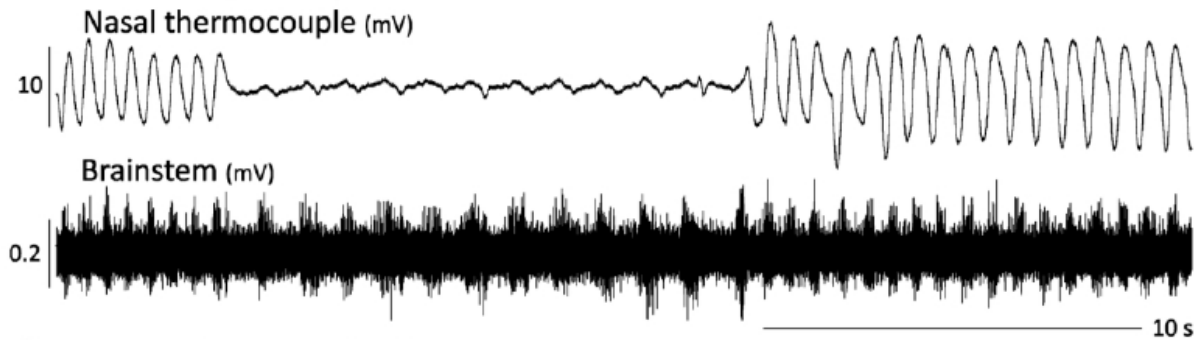

(b)

Figure 6.18 Transient apneas induced by intrahippocampal kainic acid injection. (a) Obstructive apneas. During apnea (loss of oscillation of nasal thermocouple signal), brainstem firing continues at a lower rate. (b) Partial apneas. Reduced amplitude nasal signals are observed, indicating reduced airflow. (Reprinted with permission from [80])

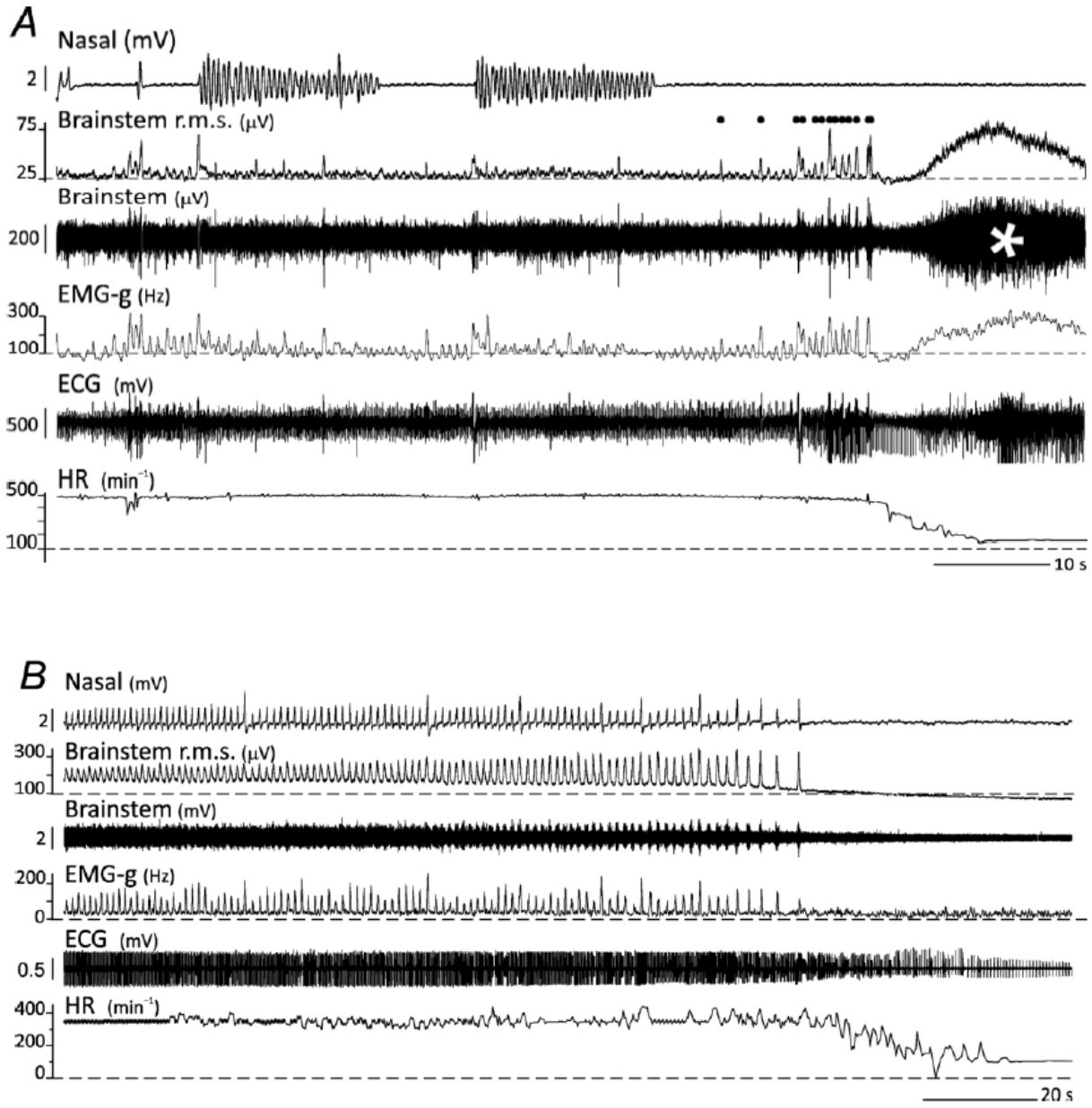

Figure 6.19 Lethal apneas following seizures induced by KA. A. Obstructive lethal apnea. Brainstem recording show increasing strength of activity with repeated attempts to breath. Brainstem recording also shows large discharge following the final attempt to breath (marked by white star). B. Central lethal apnea. Respiration slows during final seconds. (Reprinted with permission from [80])

7. SUMMARY AND CONCLUSION

A novel flexible micro-wire electrode insertion method has been proposed and demonstrated. For successful insertion, the electrode has to be straight. A crimped or damaged electrode has a high probability of failure because of reduced CBF. The dura is not required to be removed which is a big advantage of the proposed method. Using this method, the flexible microelectrode can be inserted in the brain without using any supporting rod or tube or using external coating to increase stiffness and hence the method is novel. Since the electrode is inserted without piercing the brain with a blade or sharp rod, the method is less invasive. Also since it is not coated with any other material to increase stiffness, it does not inject any additional foreign particle in the brain and hence causes less reaction in the brain.

An ultrathin micro-motion compensated micro-wire electrode has been presented. Novel techniques have been developed to fabricate the electrode tip. Also addition of helical spring at the top of the electrode for micro-motion compensation is a new dimension to electrode fabrication. The presented electrode is the longest and thinnest single shank electrode ever found in the literature. The proposed insertion method is applicable not only for platinum electrodes but also for electrodes made of gold, iridium, tungsten, carbon fiber and stainless steel. Higher increase in CBF can be achieved by reducing the separation between the guide arms. By decreasing the separation between the guide arms, insertion of micro-wire with diameter smaller 25 μm could be possible. Since the insertion process involves spinning the electrode, the technology is limited to cylindrical shaped electrode. However, if the dura is removed prior to insertion, flexible planer electrodes may be inserted successfully after modifying the geometry of the guide arms.

Based on the proposed method, an electrode insertion device has been presented. The device is equipped with all the neural recording circuitry so that it can record neural signal while insertion which is a unique feature of the inserter. The inserter is designed and operated in such precision that it is possible to capture individual neuron with required spatial resolution and hold onto it until the end of implantation. The device can be used to insert electrode at a large range of insertion angle.

A neural amplifier based on folded cascode differential OPAMP has been designed and presented. The amplifier has low noise, moderate CMRR and high input impedance which are important criteria for neural recording. Most of the neural signals presented in this thesis are obtained by using this amplifier.

In short, I have developed an advanced system for chronic neural electrode implantation which includes a novel chronic neural electrode and a novel insertion device with signal recording capability. By spinning the electrode during insertion and inserting it through the proposed guide, I have implanted 25 um wire Pt electrodes 10 mm deep in the brain of rats without any buckling and accurately targeted specific neuron. It is the thinnest and longest microelectrode ever inserted in animal brain. Microelectrodes were implanted in the Botzinger complex of rat brains and 10 week long neural activity was observed. The microelectrode and inserter not only work for rat brain but also work for rodents such as chinchilla. It is a technology platform that is capable of implanting flexible micro-wire electrode into deep brain structures for chronic brain signal studies.

APPENDIX

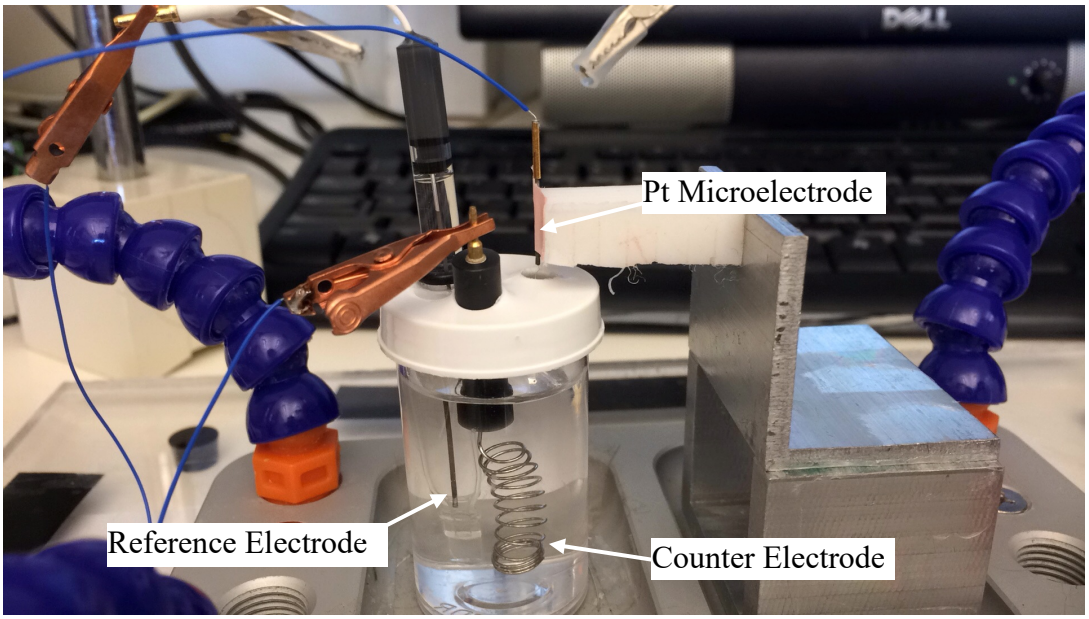

Figure A.1 Electrochemical impedance measurement using three-electrode cell configuration. WE - Pt microelectrode, CE - larger Pt spiral wire, RE - Ag/AgCl electrode.

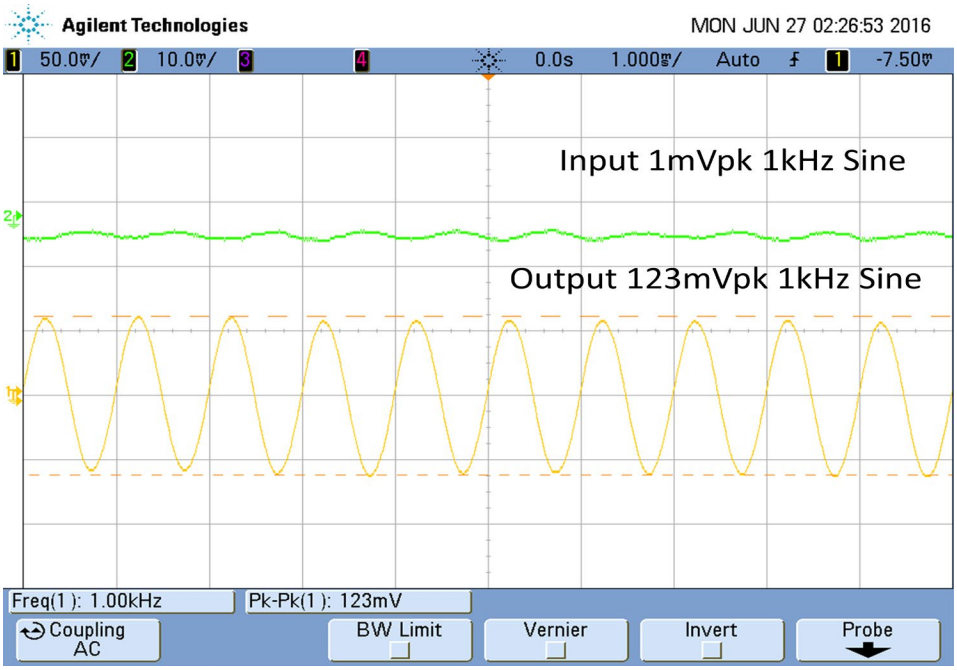

(a)

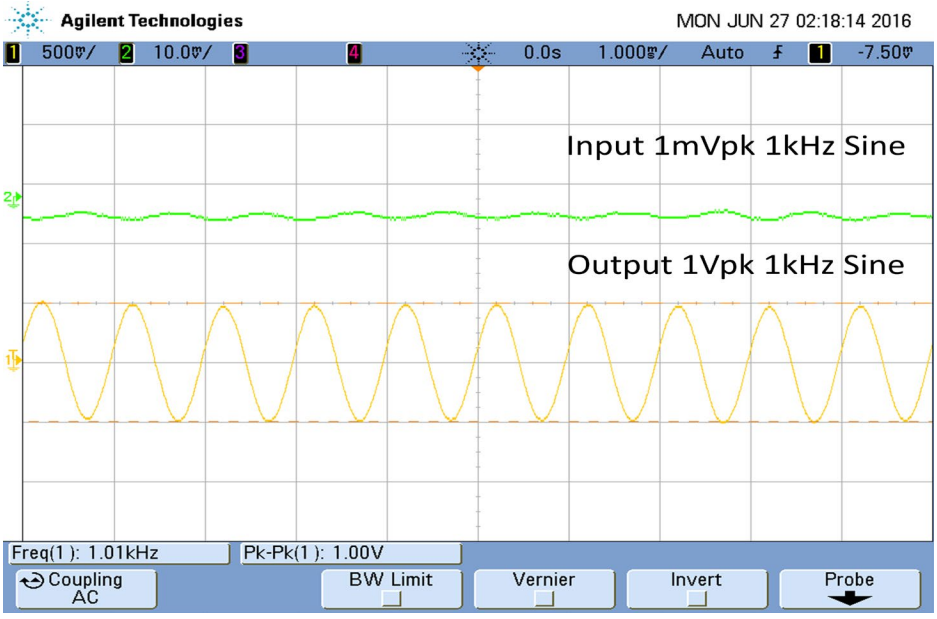

(b)

Figure A.2 Time domain input-output voltage waveform of the neural amplifier. (a) Output at gain 42 dB. (b) Output at gain 60 dB.

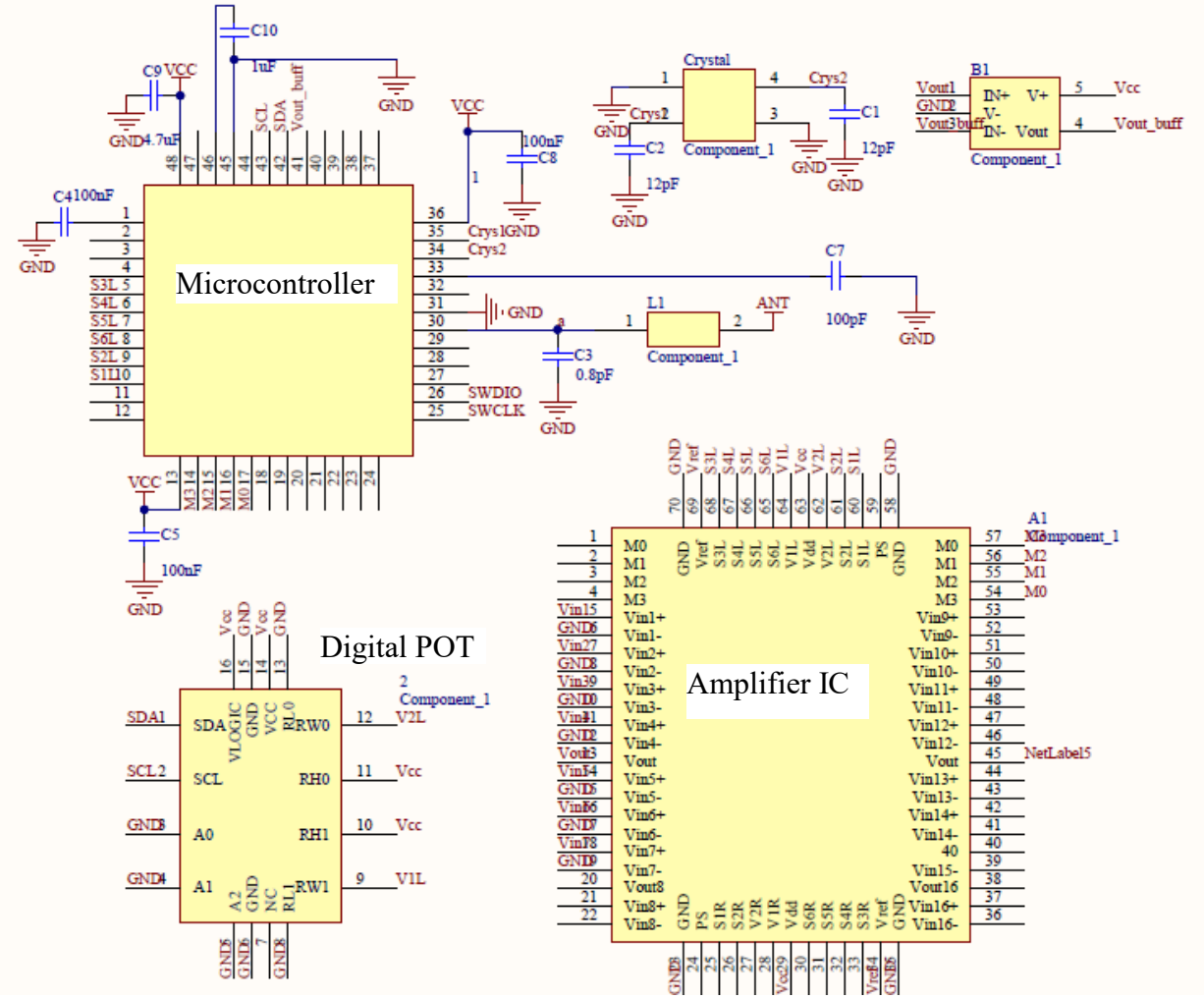

Figure A.3 Schematic diagram of the neural amplifier board.

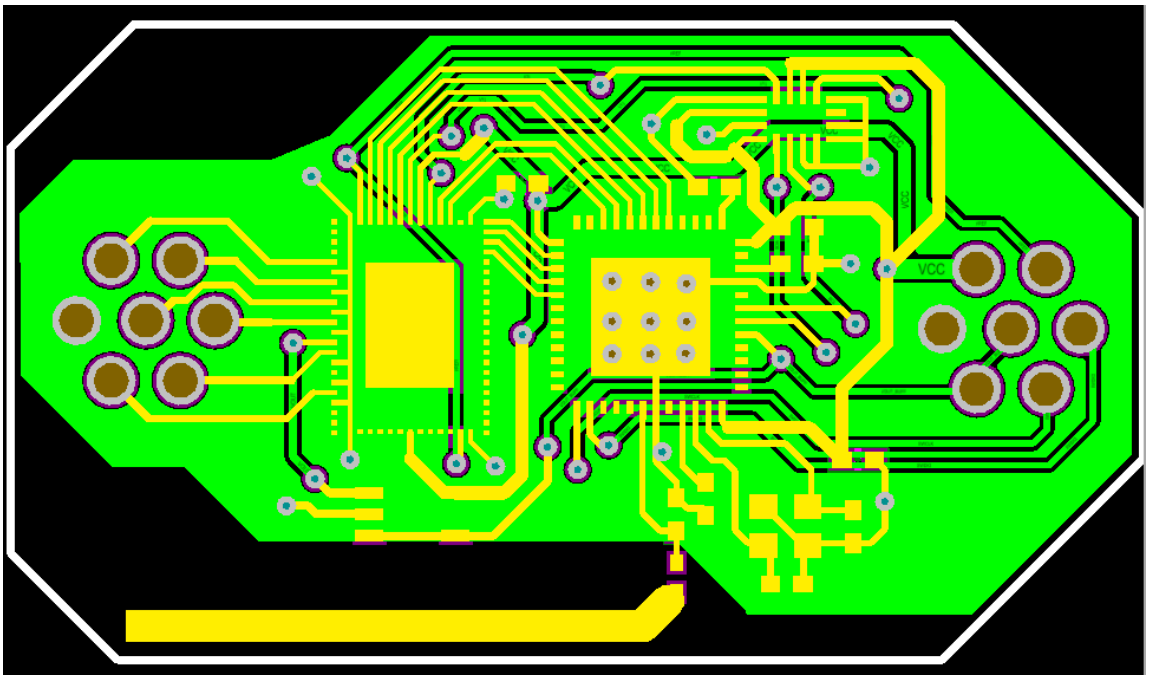

Figure A.4 Layout of the neural Amplifier board.

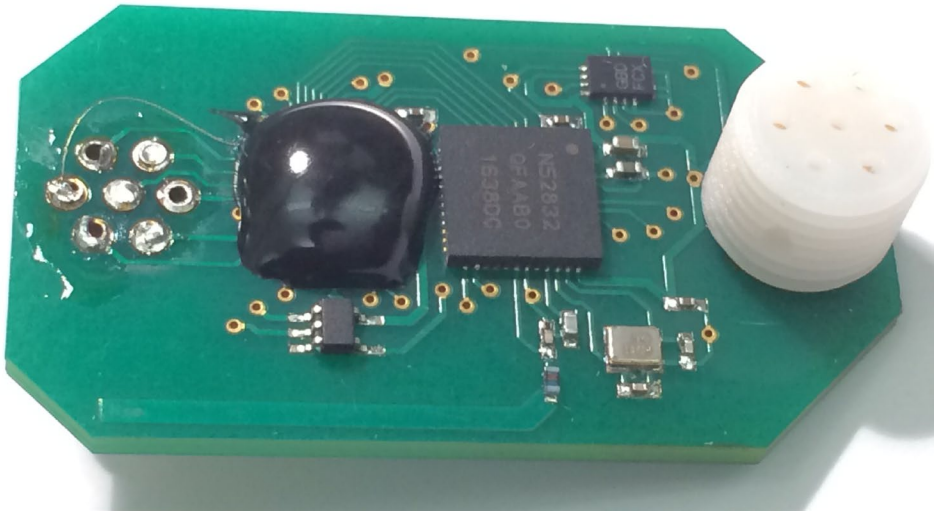

Figure A.5 Neural Amplifier Board with epoxy encapsulated IC.

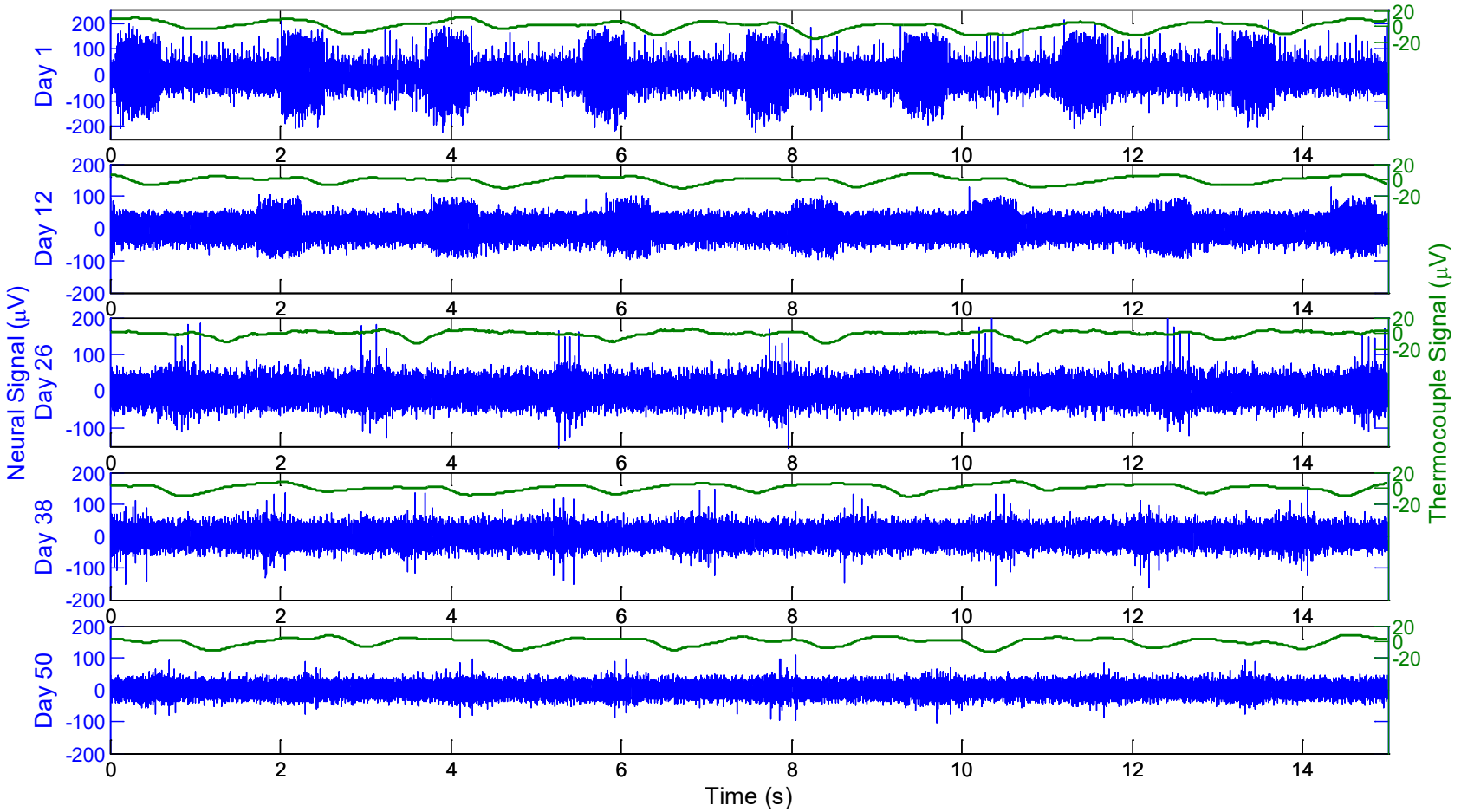

Figure A.6 Long-term neural recording from the Botzinger Complex of rat 3. (Left) Segments of respiratory neural signal recorded on day 1, 8, 21, 34 and 50. Blue trace is the neural signal and black trace is the respiration signal. (Right) The 3 largest populated spike groups after spike sorting. The percentage number of spikes in each group are given. (Middle) The PETH of the three dominant spikes in a breathing cycle.

Table A.1 Neural amplifier cut off frequencies for various control parameter settings.

Gain = 100, S1=1, S2=0

V1 (V)	V2 (V)	f_L (Hz)
1.50	1.10	0.1
1.50	0.80	1
1.50	0.75	5
1.50	0.70	18

Gain = 1000, S1=0, S2=1

V1 (V)	V2 (V)	f_L (Hz)
1.50	0.9	28
1.50	0.85	35
1.50	0.80	55
1.50	0.78	70
1.50	0.76	110
1.50	0.74	170
1.50	0.72	270
1.50	0.70	450

Gain = 1000

S6 S5 S4 S3	f_H (Hz)
0000	700
0001	730
0010	770
0011	800
0100	870
0101	910
0110	960
0111	1.00k
1000	1.80k
1001	2.00k
1010	2.22k
1011	2.52k
1100	3.45k
1101	4.10k
1110	5.00k
1111	6.23k

Gain = 100

S6 S5 S4 S3	f_H (Hz)
0000	600
0001	625
0010	650
0011	680
0100	725
0101	770
0110	800
0111	830
1000	1.33k
1001	1.46k
1010	1.56k
1011	1.70k
1100	2.12k
1101	2.12k
1110	2.77k
1111	3.30k

REFERENCES

[1] C. I. a. J.-M. Seo, "A review of electrodes for the electrical brain signal recording," *Biomed. Eng. Lett.,* vol. 6, no. 3, pp. 104-112, 2016.

[2] P. Fattahi, G. Yang, G. Kim, and M. R. Abidian, "A review of organic and inorganic biomaterials for neural interfaces," (in eng), *Adv Mater,* vol. 26, no. 12, pp. 1846-85, Mar 2014, doi: 10.1002/adma.201304496.

[3] M. Jorfi, J. L. Skousen, C. Weder, and J. R. Capadona, "Progress towards biocompatible intracortical microelectrodes for neural interfacing applications," (in eng), *J Neural Eng,* vol. 12, no. 1, p. 011001, Feb 2015, doi: 10.1088/1741-2560/12/1/011001.

[4] A. C. Patil and N. V. Thakor, "Implantable neurotechnologies: a review of micro- and nanoelectrodes for neural recording," (in eng), *Med Biol Eng Comput,* vol. 54, no. 1, pp. 23-44, Jan 2016, doi: 10.1007/s11517-015-1430-4.

[5] K. M. Szostak, L. Grand, and T. G. Constandinou, "Neural Interfaces for Intracortical Recording: Requirements, Fabrication Methods, and Characteristics," (in eng), *Front Neurosci,* vol. 11, p. 665, 2017, doi: 10.3389/fnins.2017.00665.

[6] J. A. Gallego, M. G. Perich, L. E. Miller, and S. A. Solla, "Neural Manifolds for the Control of Movement," (in eng), *Neuron,* vol. 94, no. 5, pp. 978-984, Jun 2017, doi: 10.1016/j.neuron.2017.05.025.

[7] M. A. L. Nicolelis, "Brain-machine interfaces to restore motor function and probe neural circuits," *Nat Rev Neurosci,* vol. 4, no. 5, pp. 417-422, 2003.

[8] P. Kennedy, "Changes in emotional state modulate neuronal firing rates of human speech motor cortex: a case study in long-term recording," (in eng), *Neurocase,* vol. 17, no. 5, pp. 381-93, Oct 2011, doi: 10.1080/13554794.2010.532137.

[9] A. M. Lozano, A. E. Lang, R. Levy, W. Hutchison, and J. Dostrovsky, "Neuronal recordings in Parkinson's disease patients with dyskinesias induced by apomorphine," (in eng), *Ann Neurol,* vol. 47, no. 4 Suppl 1, pp. S141-6, Apr 2000.

[10] J. Martinerie *et al.*, "Epileptic seizures can be anticipated by non-linear analysis," (in eng), *Nat Med,* vol. 4, no. 10, pp. 1173-6, Oct 1998, doi: 10.1038/2667.

[11] K. Smith, "Brain waves reveal intensity of pain," *Nature,* vol. 450, p. 329, 2007.

[12] R. B, F. A, and M. BR, "Activity of isocortex and hippocampus: electrical studies with micro-electrodes," *J Neurophysiol.,* vol. 3, no. 1, pp. 74-105, 1940.

[13] S. WOLDRING and M. N. DIRKEN, "Spontaneous unit-activity in the superficial cortical layers," (in eng), *Acta Physiol Pharmacol Neerl,* vol. 1, no. 3, pp. 369-79, Nov 1950.

[14] R. M. DOWBEN and J. E. ROSE, "A metal-filled microelectrode," (in eng), *Science,* vol. 118, no. 3053, pp. 22-4, Jul 1953, doi: 10.1126/science.118.3053.22.

[15] J. D. GREEN, "A simple microelectrode for recording from the central nervous system," (in eng), *Nature,* vol. 182, no. 4640, p. 962, Oct 1958, doi: 10.1038/182962a0.

[16] D. H. HUBEL and T. N. WIESEL, "Receptive fields of single neurones in the cat's striate cortex," (in eng), *J Physiol,* vol. 148, pp. 574-91, Oct 1959, doi: 10.1113/jphysiol.1959.sp006308.

[17] M. L. Wolbarsht, E. F. Macnichol, and H. G. Wagner, "Glass Insulated Platinum Microelectrode," (in eng), *Science,* vol. 132, no. 3436, pp. 1309-10, Nov 1960, doi: 10.1126/science.132.3436.1309.

[18] L. A. Geddes and R. Roeder, "Criteria for the selection of materials for implanted electrodes," (in eng), *Ann Biomed Eng,* vol. 31, no. 7, pp. 879-90, 2003 Jul-Aug 2003, doi: 10.1114/1.1581292.

[19] A. M. Dymond, L. E. Kaechele, J. M. Jurist, and P. H. Crandall, "Brain tissue reaction to some chronically implanted metals," (in eng), *J Neurosurg,* vol. 33, no. 5, pp. 574-80, Nov 1970, doi: 10.3171/jns.1970.33.5.0574.

[20] L. R. Hochberg *et al.*, "Neuronal ensemble control of prosthetic devices by a human with tetraplegia," (in eng), *Nature,* vol. 442, no. 7099, pp. 164-71, Jul 2006, doi: 10.1038/nature04970.

[21] J. L. Collinger *et al.*, "High-performance neuroprosthetic control by an individual with tetraplegia," (in eng), *Lancet,* vol. 381, no. 9866, pp. 557-64, Feb 2013, doi: 10.1016/S0140-6736(12)61816-9.

[22] E. N. Brown, R. Lydic, and N. D. Schiff, "General anesthesia, sleep, and coma," (in eng), *N Engl J Med,* vol. 363, no. 27, pp. 2638-50, Dec 2010, doi: 10.1056/NEJMra0808281.

[23] A. M. Chan *et al.*, "Speech-specific tuning of neurons in human superior temporal gyrus," (in eng), *Cereb Cortex,* vol. 24, no. 10, pp. 2679-93, Oct 2014, doi: 10.1093/cercor/bht127.

[24] R. Q. Quiroga, L. Reddy, G. Kreiman, C. Koch, and I. Fried, "Invariant visual representation by single neurons in the human brain," (in eng), *Nature,* vol. 435, no. 7045, pp. 1102-7, Jun 2005, doi: 10.1038/nature03687.

[25] W. Truccolo *et al.*, "Single-neuron dynamics in human focal epilepsy," (in eng), *Nat Neurosci,* vol. 14, no. 5, pp. 635-41, May 2011, doi: 10.1038/nn.2782.

[26] C. P. Warren, S. Hu, M. Stead, B. H. Brinkmann, M. R. Bower, and G. A. Worrell, "Synchrony in normal and focal epileptic brain: the seizure onset zone is functionally disconnected," (in eng), *J Neurophysiol,* vol. 104, no. 6, pp. 3530-9, Dec 2010, doi: 10.1152/jn.00368.2010.

[27] V. S. Polikov, M. L. Block, J. M. Fellous, J. S. Hong, and W. M. Reichert, "In vitro model of glial scarring around neuroelectrodes chronically implanted in the CNS," (in eng), *Biomaterials,* vol. 27, no. 31, pp. 5368-76, Nov 2006, doi: 10.1016/j.biomaterials.2006.06.018.

[28] V. S. Polikov, P. A. Tresco, and W. M. Reichert, "Response of brain tissue to chronically implanted neural electrodes," (in eng), *J Neurosci Methods,* vol. 148, no. 1, pp. 1-18, Oct 2005, doi: 10.1016/j.jneumeth.2005.08.015.

[29] G. C. McConnell, H. D. Rees, A. I. Levey, C. A. Gutekunst, R. E. Gross, and R. V. Bellamkonda, "Implanted neural electrodes cause chronic, local inflammation that is correlated with local neurodegeneration," (in eng), *J Neural Eng,* vol. 6, no. 5, p. 056003, Oct 2009, doi: 10.1088/1741-2560/6/5/056003.

[30] J. N. Turner *et al.*, "Cerebral astrocyte response to micromachined silicon implants," (in eng), *Exp Neurol,* vol. 156, no. 1, pp. 33-49, Mar 1999, doi: 10.1006/exnr.1998.6983.

[31] D. H. Szarowski *et al.*, "Brain responses to micro-machined silicon devices," (in eng), *Brain Res,* vol. 983, no. 1-2, pp. 23-35, Sep 2003.

[32] R. Biran, D. C. Martin, and P. A. Tresco, "The brain tissue response to implanted silicon microelectrode arrays is increased when the device is tethered to the skull," (in eng), *J Biomed Mater Res A,* vol. 82, no. 1, pp. 169-78, Jul 2007, doi: 10.1002/jbm.a.31138.

[33] R. Biran, D. C. Martin, and P. A. Tresco, "Neuronal cell loss accompanies the brain tissue response to chronically implanted silicon microelectrode arrays," (in eng), *Exp Neurol,* vol. 195, no. 1, pp. 115-26, Sep 2005, doi: 10.1016/j.expneurol.2005.04.020.

[34] T. D. Kozai *et al.*, "Ultrasmall implantable composite microelectrodes with bioactive surfaces for chronic neural interfaces," (in eng), *Nat Mater,* vol. 11, no. 12, pp. 1065-73, Dec 2012, doi: 10.1038/nmat3468.

[35] J. P. Seymour and D. R. Kipke, "Neural probe design for reduced tissue encapsulation in CNS," (in eng), *Biomaterials,* vol. 28, no. 25, pp. 3594-607, Sep 2007, doi: 10.1016/j.biomaterials.2007.03.024.

[36] J. L. Skousen, S. M. Merriam, O. Srivannavit, G. Perlin, K. D. Wise, and P. A. Tresco, "Reducing surface area while maintaining implant penetrating profile lowers the brain foreign body response to chronically implanted planar silicon microelectrode arrays," (in eng), *Prog Brain Res,* vol. 194, pp. 167-80, 2011, doi: 10.1016/B978-0-444-53815-4.00009-1.

[37] S. M. Wellman *et al.*, "A Materials Roadmap to Functional Neural Interface Design," (in eng), *Adv Funct Mater,* vol. 28, no. 12, Mar 2018, doi: 10.1002/adfm.201701269.

[38] P. J. Rousche, D. S. Pellinen, D. P. Pivin, J. C. Williams, R. J. Vetter, and D. R. Kipke, "Flexible polyimide-based intracortical electrode arrays with bioactive capability," (in eng), *IEEE Trans Biomed Eng,* vol. 48, no. 3, pp. 361-71, Mar 2001, doi: 10.1109/10.914800.

[39] T. Shoji, S. Takafumi, M. Kunihiko, and F. Hiroyuki, "3D flexible multichannel neural probe array," *Journal of Micromechanics and Microengineering,* vol. 14, no. 1, pp. 104-107, 2004.

[40] J. Myounggun, "Partially flexible MEMS neural probe composed of polyimide and sucrose gel for reducing brain damage during and after implantation," *Journal of Micromechanics and Microengineering,* vol. 24, no. 2, p. 025010, 2014.

[41] R. Goyal, M. Guvendiren, O. Freeman, Y. Mao, and J. Kohn, "Optimization of Polymer-ECM Composite Scaffolds for Tissue Engineering: Effect of Cells and Culture Conditions on Polymeric Nanofiber Mats," (in eng), *J Funct Biomater,* vol. 8, no. 1, Jan 2017, doi: 10.3390/jfb8010001.

[42] A. Weltman, J. Yoo, and E. Meng, "Flexible, Penetrating Brain Probes Enabled by Advances in Polymer Microfabrication," (in eng), *Micromachines (Basel),* vol. 7, no. 10, Oct 2016, doi: 10.3390/mi7100180.

[43] C. Hassler, J. Guy, M. Nietzschmann, D. T. Plachta, J. F. Staiger, and T. Stieglitz, "Intracortical polyimide electrodes with a bioresorbable coating," (in eng), *Biomed Microdevices,* vol. 18, no. 5, p. 81, 10 2016, doi: 10.1007/s10544-016-0106-7.

[44] D. P. O. Brien, T. R. Nichols, and M. G. Allen, "Flexible microelectrode arrays with integrated insertion devices," *Technical Digest. MEMS 2001. 14th IEEE International Conference on Micro Electro Mechanical Systems (Cat. No.01CH37090),* pp. 216-219, 2001, doi: 10.1109/MEMSYS.2001.906517.

[45] J. T. Kuo *et al.*, "Novel flexible Parylene neural probe with 3D sheath structure for enhancing tissue integration," (in eng), *Lab Chip,* vol. 13, no. 4, pp. 554-61, Feb 2013, doi: 10.1039/c2lc40935f.

[46] X. Jiao, Y. Wang, and Q. Qing, "Scalable Fabrication Framework of Implantable Ultrathin and Flexible Probes with Biodegradable Sacrificial Layers," (in eng), *Nano Lett,* vol. 17, no. 12, pp. 7315-7322, 12 2017, doi: 10.1021/acs.nanolett.7b02851.

[47] T. D. Kozai *et al.*, "Chronic tissue response to carboxymethyl cellulose based dissolvable insertion needle for ultra-small neural probes," (in eng), *Biomaterials,* vol. 35, no. 34, pp. 9255-68, Nov 2014, doi: 10.1016/j.biomaterials.2014.07.039.

[48] F. Vitale, S. R. Summerson, B. Aazhang, C. Kemere, and M. Pasquali, "Neural stimulation and recording with bidirectional, soft carbon nanotube fiber microelectrodes," (in eng), *ACS Nano,* vol. 9, no. 4, pp. 4465-74, 2015, doi: 10.1021/acsnano.5b01060.

[49] T. I. Kim *et al.*, "Injectable, cellular-scale optoelectronics with applications for wireless optogenetics," (in eng), *Science,* vol. 340, no. 6129, pp. 211-6, Apr 2013, doi: 10.1126/science.1232437.

[50] K. A. Potter, A. C. Buck, W. K. Self, and J. R. Capadona, "Stab injury and device implantation within the brain results in inversely multiphasic neuroinflammatory and neurodegenerative responses," (in eng), *J Neural Eng,* vol. 9, no. 4, p. 046020, Aug 2012, doi: 10.1088/1741-2560/9/4/046020.

[51] D. B. Jaroch, M. P. Ward, E. Y. Chow, J. L. Rickus, and P. P. Irazoqui, "Magnetic insertion system for flexible electrode implantation," (in eng), *J Neurosci Methods,* vol. 183, no. 2, pp. 213-22, Oct 2009, doi: 10.1016/j.jneumeth.2009.07.001.

[52] F. Vitale *et al.*, "Fluidic Microactuation of Flexible Electrodes for Neural Recording," (in eng), *Nano Lett,* vol. 18, no. 1, pp. 326-335, 01 2018, doi: 10.1021/acs.nanolett.7b04184.

[53] S. P. Marshall, W. C. Lin, P. R. Patel, A. J. Shih, and C. A. Chestek, "Effects of geometry and material on the insertion oi very small neural electrode," *2016 38th Annual International Conference of the IEEE Engineering in Medicine and Biology Society (EMBC),* pp. 2784-2788, 2016, doi: 10.1109/EMBC.2016.7591308.

[54] F. Pervin and W. W. Chen, "Mechanically Similar Gel Simulants for Brain Tissues," in *Dynamic Behavior of Materials, Volume 1*, New York, NY, T. Proulx, Ed., 2011// 2011: Springer New York, pp. 9-13.

[55] J. P. Harris *et al.*, "In vivo deployment of mechanically adaptive nanocomposites for intracortical microelectrodes," (in eng), *J Neural Eng,* vol. 8, no. 4, p. 046010, Aug 2011, doi: 10.1088/1741-2560/8/4/046010.

[56] S. Timoshenko, *Theory of elastic stability*. New York: Mc Graw-Hill, 1936.

[57] M. A. Arafat, L. N. Rubin, J. G. R. Jefferys, and P. P. Irazoqui, "A Method of Flexible Micro-Wire Electrode Insertion in Rodent for Chronic Neural Recording and a Device for Electrode Insertion," (in eng), *IEEE Trans Neural Syst Rehabil Eng,* vol. 27, no. 9, pp. 1724-1731, Sep 2019, doi: 10.1109/TNSRE.2019.2932032.

[58] Z. Fekete, A. Németh, G. Márton, I. Ulbert, and A. Pongrácz, "Experimental study on the mechanical interaction between silicon neural microprobes and rat dura mater during insertion," (in eng), *J Mater Sci Mater Med,* vol. 26, no. 2, p. 70, Feb 2015, doi: 10.1007/s10856-015-5401-y.

[59] K. Najafi and J. F. Hetke, "Strength characterization of silicon microprobes in neurophysiological tissues," (in eng), *IEEE Trans Biomed Eng,* vol. 37, no. 5, pp. 474-81, May 1990, doi: 10.1109/10.55638.

[60] P. J. Rousche and R. A. Normann, "A method for pneumatically inserting an array of penetrating electrodes into cortical tissue," (in eng), *Ann Biomed Eng,* vol. 20, no. 4, pp. 413-22, 1992.

[61] A. Obaid, Y.-W. Wu, M. Hanna, W. Nix, J. Ding, and N. Melosh, "Ultra-sensitive measurement of brain penetration with microscale probes for brain machine interface considerations," *bioRxiv,* p. 454520, 2018, doi: 10.1101/454520.

[62] J. Hsu, L. Rieth, R. A. Normann, P. Tathireddy, and F. Solzbacher, "Encapsulation of an Integrated Neural Interface Device With Parylene C," *IEEE Transactions on Biomedical Engineering,* vol. 56, no. 1, pp. 23-29, 2009, doi: 10.1109/TBME.2008.2002155.

[63] E. Meng, P.-Y. Li, and Y.-C. Tai, "Plasma removal of Parylene C," *Journal of Micromechanics and Microengineering,* vol. 18, no. 4, p. 045004, 2008/02/22 2008, doi: 10.1088/0960-1317/18/4/045004.

[64] R. R. Harrison and C. Charles, "A low-power low-noise CMOS amplifier for neural recording applications," *IEEE Journal of Solid-State Circuits,* vol. 38, no. 6, pp. 958-965, 2003, doi: 10.1109/JSSC.2003.811979.

[65] R. R. Harrison *et al.*, "A Low-Power Integrated Circuit for a Wireless 100-Electrode Neural Recording System," *IEEE Journal of Solid-State Circuits,* vol. 42, no. 1, pp. 123-133, 2007, doi: 10.1109/JSSC.2006.886567.

[66] W. Wattanapanitch, M. Fee, and R. Sarpeshkar, "An Energy-Efficient Micropower Neural Recording Amplifier," *IEEE Transactions on Biomedical Circuits and Systems,* vol. 1, no. 2, pp. 136-147, 2007, doi: 10.1109/TBCAS.2007.907868.

[67] B. Razavi, *Design of Analog CMOS Integrated Circuits*. New York, NY , USA: McGraw-Hill, Inc. , 2001.

[68] W. Wattanapanitch and R. Sarpeshkar, "A low-power 32-channel digitally programmable neural recording integrated circuit," (in eng), *IEEE Trans Biomed Circuits Syst,* vol. 5, no. 6, pp. 592-602, Dec 2011, doi: 10.1109/TBCAS.2011.2163404.

[69] D. Han, Y. Zheng, R. Rajkumar, G. S. Dawe, and M. Je, "A 0.45 V 100-channel neural-recording IC with sub- μW/channel consumption in 0.18 μm CMOS," (in eng), *IEEE Trans Biomed Circuits Syst,* vol. 7, no. 6, pp. 735-46, Dec 2013, doi: 10.1109/TBCAS.2014.2298860.

[70] Z. Xiaodan *et al.*, "A 100-Channel 1-mW Implantable Neural Recording IC," *IEEE Transactions on Circuits and Systems I: Regular Papers,* vol. 60, no. 10, pp. 2584-2596, 2013, doi: 10.1109/TCSI.2013.2249175.

[71] C. M. Lopez *et al.*, "An Implantable 455-Active-Electrode 52-Channel CMOS Neural Probe," *IEEE Journal of Solid-State Circuits,* vol. 49, no. 1, pp. 248-261, 2014, doi: 10.1109/JSSC.2013.2284347.

[72] K. J. Paralikar, J. K. Lawrence, and R. S. Clement, "Collagenase-aided Insertion of Intracortical Microelectrode Arrays: Evaluation of Insertion Force and Chronic Recording Performance," *2006 International Conference of the IEEE Engineering in Medicine and Biology Society,* pp. 2958-2961, 2006, doi: 10.1109/IEMBS.2006.260302.

[73] E. G. Merrill, "Where are the real respiratory neurons?," (in eng), *Fed Proc,* vol. 40, no. 9, pp. 2389-94, Jul 1981.

[74] G. Paxinos and C. Watson, *The rat brain in stereotaxic coordinates*, 6th ed. ed. Amsterdam ; Boston ; Oxford: Academic, 2006.

[75] D. W. Richter, "Generation and maintenance of the respiratory rhythm," (in eng), *J Exp Biol,* vol. 100, pp. 93-107, Oct 1982.

[76] D. W. Richter and J. C. Smith, "Respiratory rhythm generation in vivo," (in eng), *Physiology (Bethesda),* vol. 29, no. 1, pp. 58-71, Jan 2014, doi: 10.1152/physiol.00035.2013.

[77] T. H. Bryant, S. Yoshida, D. de Castro, and J. Lipski, "Expiratory neurons of the Bötzinger Complex in the rat: a morphological study following intracellular labeling with biocytin," (in eng), *J Comp Neurol,* vol. 335, no. 2, pp. 267-82, Sep 1993, doi: 10.1002/cne.903350210.

[78] P. Sokal, M. Harat, M. Rusinek, M. Rudaś, and A. Litwinowicz, "Intraoperative CT verification of electrode localization in DBS surgery in Parkinson's disease," *Interdisciplinary Neurosurgery,* vol. 2, no. 1, pp. 6-9, 2015, doi: http://dx.doi.org/10.1016/j.inat.2014.10.002.

[79] J. J. DiCarlo, J. W. Lane, S. S. Hsiao, and K. O. Johnson, "Marking microelectrode penetrations with fluorescent dyes," (in eng), *J Neurosci Methods,* vol. 64, no. 1, pp. 75-81, Jan 1996, doi: 10.1016/0165-0270(95)00113-1.

[80] J. G. R. Jefferys, M. A. Arafat, P. P. Irazoqui, and T. A. Lovick, "Brainstem activity, apnea, and death during seizures induced by intrahippocampal kainic acid in anaesthetized rats," (in eng), *Epilepsia,* Nov 2019, doi: 10.1111/epi.16374.

VITA

Muhammad Abdullah Arafat has been working toward his PhD in the Electrical and Computer Engineering Department at Purdue University since August 2013. His focus at Purdue has been insertion mechanism of chronic recording neural electrodes. Arafat was born and raised in Dhaka, capital of Bangladesh and attended Bangladesh University of Engineering and Technology (BUET) in Dhaka. He obtained his B.Sc. degree in Electrical and Electronic Engineering in 2009 and joined the Department of Electrical and Electronic Engineering, BUET as a lecturer after graduation. Besides his teaching profession, he was also studying M.Sc. in Electrical and Electronic Engineering in BUET and obtained his M.Sc. degree in 2011. He was promoted to Assistant Professor in 2012. After four years in teaching profession, Arafat decided to pursue PhD in a US university. Arafat applied for and was accepted into the PhD program in the Department of Electrical and Computer Engineering at Purdue University with the intent of working in the field of implantable devices. He took leave from BUET and came to USA in 2013. Arafat was awarded graduate research assistantship and was funded in his whole PhD research period.

Upon graduating from Purdue University, Arafat plans to return to home country and continue working as a professor in BUET. He will continue his research on microelectrode and develop his own laboratory. In future, he will also apply for post-doctoral research fellowship in US universities.